POLITECNICO DI TORINO

Master Degree in Mathematical Engineering

Master Degree Thesis

Reaction-Diffusion Models of Protein Propagation in Neurodegenerative Diseases: The Case of Alzheimer's

Supervisors
Prof. Luigi Preziosi
Dr. Sara Garbarino

Candidate
Erika Rongoni

Academic Year 2024-2025

Contents

List of Figures

List of Tables

1. Abstract

Understanding the development of neurodegenerative diseases represents an open challenge for modern medicine today and is a fundamental step toward the possible identification of therapies. The aim of this thesis is to study the progression of these conditions inside the brain - in particular Alzheimer's disease - using reaction-diffusion models. The present research links the continuous diffusion model with the brain connectome, which is described by a discrete network model.

Using COMSOL Multiphysics software, a three-dimensional geometry of the right brain hemisphere and its connectome structure is constructed. The study initially implements the Fisher-Kolmogorov model to investigate the role of tau protein in initiating the disease. Subsequently, the focus shifts to the interaction between tau and β-amyloid proteins, as recent studies suggest that the spread of β-amyloid is the key driver of early cognitive decline and highly interacts with tau proteins. A tailored model is then developed to apply the findings to a cohort of patients at different stages of the disease.

All numerical simulations are followed by a parametric study investigating the rates of conversion of healthy proteins into misfolded forms, the interaction parameter between pathological species, and the time required for complete invasion of the cerebral cortex.

In the analysis of the patient cohort, simulation results are compared to clinical data to assess the correspondence between modelled predictions and observed disease progression.

The results demonstrate that the implemented models effectively reproduce the spatial and temporal patterns of misfolded protein propagation, offering a realistic representation of disease dynamics.

2. Introduction

2.1 The brain

The brain is the principal organ of the nervous system in all vertebrates and most invertebrates. It is usually located in the head, near the sensory organs, responsible for processing signals from the rest of the body [17]. As the control center of the organism, it plays a fundamental role in regulating both voluntary and involuntary functions.

In humans, the brain, together with the spinal cord — connected through the brainstem — constitutes the central nervous system. It controls most bodily activities by receiving, analyzing, and coordinating information from the sense organs. Through the processing of incoming stimuli, it determines which instructions to send to the rest of the body.

Anatomically, the brain is enclosed within the cranial cavity, which serves a crucial protective role, and is immersed in cerebrospinal fluid. It is separated from the rest of the body's blood flow by the blood-brain barrier, which regulates the exchange of substances to maintain a stable environment. Nonetheless, the brain is vulnerable to injury, disease, and infection. Injury may result from physical trauma or reduced blood flow — a condition known as *ictus*. The most common diseases affecting the brain are neurodegenerative disorders such as Parkinson's disease, various forms of dementia (including Alzheimer's disease), and multiple sclerosis. Tumors may also develop, often as metastases from other body regions.

The structure that most distinguishes the mammalian brain from that of invertebrates is the cerebral cortex, a continuous laminar layer of gray matter forming the outer surface and covering the white matter of the cerebral hemispheres. It is composed of neurons and nerve fibers and has a thickness of approximately 2–4 mm.

Functionally, the brain comprises the telencephalon and the diencephalon. The telencephalon includes the cerebral hemispheres and forms the largest part of the brain. Each hemisphere is conventionally divided into four lobes: frontal, parietal, occipital, and temporal. Each lobe contains cortical areas responsible for specific functions. The diencephalon is a group of neural structures located between the left and right hemispheres. Although the hemispheres are largely similar in form and function, some tasks are more specialized — for example, language is typically associated with the left hemisphere, while visuospatial abilities are more dominant in the right. The hemispheres are interconnected by neural pathways, the largest of which is the corpus callosum.

The average adult human brain weighs about 1.2 - 1.4 kg and represents roughly 2% of total body weight. It has a volume of approximately 1260 cm^3 in men and about 1130 cm^3 in women, although significant individual variation exists.

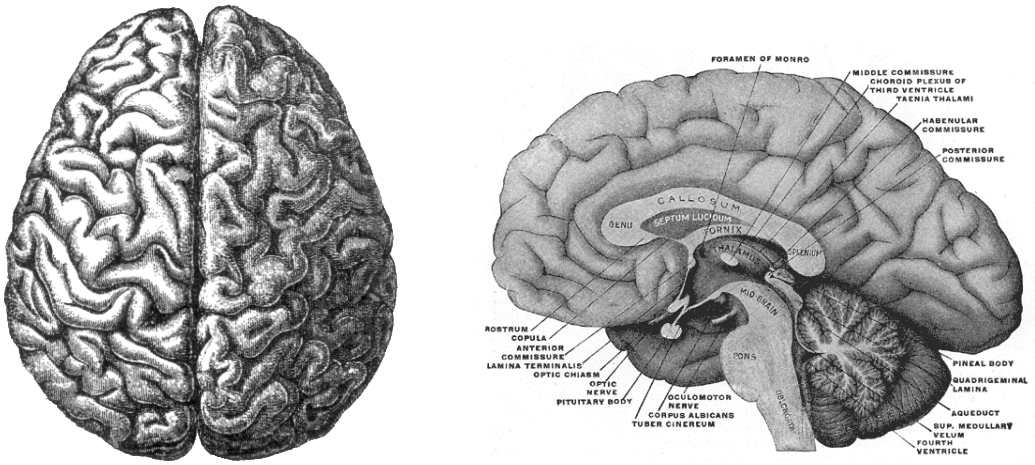

Figure 2.1: Left: top view drawing of an encephalon, depicting the two cerebral hemispheres and their overall shape [13]. Right: diagram of the vertical (sagittal) section of a human brain, showing key internal structures such as the corpus callosum, thalamus, hypothalamus, brainstem, and cerebellum [6]. Together, these views offer a complementary representation of both external and internal brain anatomy.

2.2 Biology of neurodegenerative diseases

Proteins are biological macromolecules composed of chains of amino acids that form the foundation of all living organisms. They perform a wide range of functions in the human body, including catalyzing metabolic reactions, facilitating synthesis, responding to stimuli, and transporting molecules across different sites.

Proteins have a natural tendency to fold into compact, three-dimensional structures. Only properly folded proteins are stable in biological environments over time. Failures in folding are associated with pathological conditions, leading to the disruption of vital cellular, tissue, and organ functions. Misfolded proteins can aggregate into insoluble fibrils or plaques, which are toxic to cells and interfere with normal physiological processes.

The diversity of neurodegenerative diseases arises from the specific proteins involved in misfolding. Notable examples include prion disease, Alzheimer's disease (AD), Parkinson's disease (PD), Creutzfeldt-Jakob disease, and Amyotrophic Lateral Sclerosis (ALS) [5].

Figure 2.2 illustrates the correlation between the accumulation of misfolded proteins and their respective neurodegenerative diseases.

a−**e**: In Alzheimer's disease, the formation of β-amyloid protein plaques begins in the neocortical region and subsequently spreads throughout the brain.

b−**f**: Also in Alzheimer's disease, tau protein accumulation begins in the *locus coeruleus*, then spreads to the transentorhinal and hippocampal areas.

c−**g**: In Parkinson's disease, α-synuclein protein propagation begins in the brainstem. The first lesions appear in the olfactory bulb and medulla oblongata, later affecting other areas.

d−**h**: In ALS, TDP-43 protein is initially found in the granular motor cortex and α-motor neurons of the spinal cord. The disease then progresses toward the prefrontal and post-central cortex, eventually reaching the temporal and hippocampal regions.

Despite their significant impact on tissue biology and cognitive function, the mechanisms behind the emergence and aggregation of misfolded proteins remain poorly understood. Their prevalence and toxicity have been widely studied over recent decades and continue to be the subject of scientific debate.

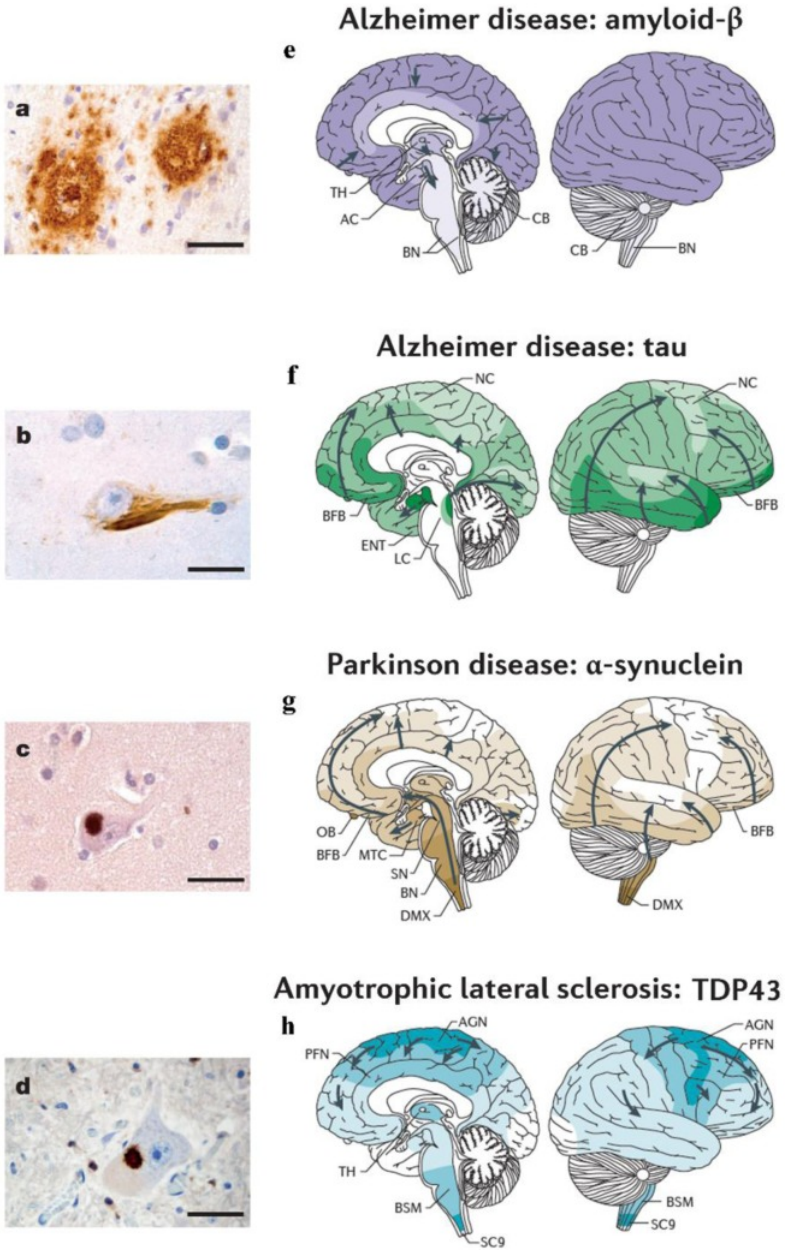

Figure 2.2: Misfolded proteins (**a**–**d**) and corresponding patterns of disease progression (**e**–**h**) in major neurodegenerative disorders [5].

2.3 Pathogenic protein aggregates: the prion paradigm

The prion paradigm emerged after decades of research into unusual animal and human diseases characterized by atypical infectivity, prolonged incubation periods, and the absence of inflammation or any detectable viral agent. In the 1980s, Prusiner and his colleagues first demonstrated that the infectious agent responsible for these diseases was an abnormally folded protein, which led to the coining of the term "prion".

Pathologically, prion diseases are characterized by the accumulation of prion proteins (PrPs), which eventually lead to neuronal loss and structural changes in the brain. Under normal conditions, PrPs adopt a non-pathogenic three-dimensional conformation. Disease occurs when these proteins misfold and aggregate into structures known as "oligomers" and "fibrils".

The fundamental mechanism underlying the disease is the aggregation of normally produced prion protein (PrP). This process can be triggered by different factors, depending on the form of the disease:

- Hereditary form, caused by gene mutations that increase the tendency of PrP to misfold;
- Infectious form, resulting from the introduction of already misfolded prion proteins (seeds) from external sources;
- Idiopathic form, arising from spontaneous misfolding of PrP, followed by the self-propagation of endogenous misfolded seeds.

The term 'infectivity' in the context of prions refers to disease initiation caused by an external misfolded protein that enters the body and induces misfolding in native PrPs. Since these aggregates are formed from endogenous proteins, the immune system fails to recognize them as foreign and does not mount a defensive response. In humans, prion diseases of infectious origin are extremely rare: only approximately 3400 cases have been identified globally, and such occurrences are now virtually non-existent.

Typically, once the disease is established in the body, it enters a clinically silent incubation period during which it spreads within the brain. Eventually, characteristic signs and symptoms appear, culminating in death [23].

Within the brain, prions spread with high specificity along defined anatomical pathways, suggesting that neuronal transport mechanisms play a central role in their propagation.

2.4 The Alzheimer's disease

The intriguing clinical and pathological similarities between prion diseases and neurodegenerative disorders have been extensively studied. Among these, Alzheimer's disease (AD) stands out as a major neurodegenerative condition, characterized clinically by a progressive decline in cognitive function and histologically by the presence of intra-cerebral plaques and neurofibrillary tangles.

Plaques are heterogeneous lesions consisting of extracellular masses of amyloid fibrillar peptide (Aβ), while tangles consist of intracellular bundles of fibrillar tau protein. As the

disease advances, additional lesion types, such as cerebral Aβ-amyloid angiopathy, as well as age-related comorbidities, are often observed in the brain.

Tau protein is found in large quantities inside neurons and plays a key role in stabilizing microtubules. In several neurodegenerative disorders, including AD, tau undergoes abnormal hyperphosphorylation and polymerization, a pathological process referred to as tauopathy, which initiates the cascade of events that trigger disease progression. The spread typically begins in the *locus coeruleus*, proceeds to the transentorhinal region, and subsequently reaches the entorhinal cortex, eventually propagating to the neocortex and axonally connected areas.

Recent studies have demonstrated that β-amyloid oligomers (sAβ), very small assemblies of soluble misfolded proteins, are the primary mediators of misfolding transmission, promoting the aggregation of additional pathological proteins. Due to their extracellular localization, Aβ oligomers diffuse through the brain's interstitial fluid and propagate anisotropically along neuronal fibre tracts, thereby reaching and inducing misfolding in previously unaffected cells.

2.5 The connectome

A major challenge in understanding neurodegenerative diseases lies in deciphering the clinico-pathological relationships that influence both diagnosis and treatment. The same primary pathology can give rise to multiple clinical syndromes, while a single syndrome may stem from diverse neurodegenerative aetiologies. Therefore, an ideal approach to disease identification involves investigating the functional networks responsible for information processing and transfer in the brain. This may help correlate neuropathological patterns with clinical syndromes — for instance, dementia in the case of Alzheimer's disease (AD).

Cognitive abilities rely on large-scale functional networks distributed throughout the brain. Post-mortem studies have shown that neurodegenerative pathology often spreads within strongly connected anatomical regions, where neurofibrillary tangles are more extensive. The study of this process is central to the 'prion-like' hypothesis, which describes the propagation of misfolded proteins from their site of origin along neuronal pathways. Despite mounting evidence that neuronal networks contribute to disease progression, many aspects of their role remain poorly understood [22].

The prion-like diffusion hypothesis implies a view of the network as a tangle of passive connections between distant brain areas, through which pathogens are transported. However, recent theories suggest a more active role, proposing that certain network hubs may facilitate or even generate pathological proteins, acting as catalysts for disease progression. A central concept in this framework is the connectome: a comprehensive map of neural connections in the brain, encompassing both adjacent and long-range pathways mediated by axonal projections. Both post-mortem analyses and neuroimaging studies support the notion that such networks serve as channels for the transmission of misfolded proteins across functionally connected but anatomically distinct regions.

In AD, neuroimaging using positron emission tomography (PET) has revealed significant overlap between the spatial distribution of β-amyloid and fronto-parietal networks, as well as a correlation between tau accumulation and specific functional circuits.

Recent approaches employ 'correlative network models', based on graph theory, where

nodes represent brain regions and edges represent biological or functional connectivity. The central hypothesis is that disease propagation begins in one or more epicentral regions and spreads along synaptic connections. Imaging studies have shown that areas most strongly connected to these epicentres often exhibit the fastest rates of pathological protein accumulation or grey matter atrophy, as observed in AD.

This framework is illustrated in figure 2.3:

a. On the left, the neuroimaging technique allows for the regional quantification of protein accumulation. Red areas indicate regions with high tau protein deposition, whereas yellow areas show lower levels. On the right, the structure of the connectome is displayed, highlighting the white matter tracts that interconnect different brain regions.

b. The left panel illustrates a potential approach to analyzing the network architecture: brain regions are modelled as nodes, and the interconnections between them are represented as edges in a graph. The shading intensity of each node reflects the local burden of pathological proteins, with the darkest red node representing the epicentre of disease propagation. Based on both the intrinsic properties of nodes and their network connectivity, the model estimates how the pathology may spread to distant areas of the brain. On the right, a linear correlation is shown between pathological burden and network connectivity: the higher the connectivity, the greater the accumulation of tau in the corresponding region. Additionally, nodal properties allow predictions of spatial propagation patterns.

c. Individual-specific models are generated by integrating PET-based regional measurements of tau deposition. For each subject, a graph-based model is constructed to reflect the individual's unique brain network architecture. Variations in these architectures may account for differences in the pattern and extent of pathological spread. Below, a covariance matrix illustrates the relationship between tau-PET signal across brain regions and the corresponding network connectivity, offering insights into the association between brain structure and the spatial diffusion of pathology.

d. After defining the spatial propagation model, this is integrated with the temporal dynamics of disease progression. These models simulate the early accumulation of misfolded aggregates in initial regions, followed by their diffusion through the network over time. This process is governed by a set of parameters that take into account node characteristics such as aggregation, production and diffusion, as well as the connectivity of the network itself.

The idea that networks thus serve as conduits for the spread of disease suggests that disease progression can be simulated from the information from imaging representing the network itself.

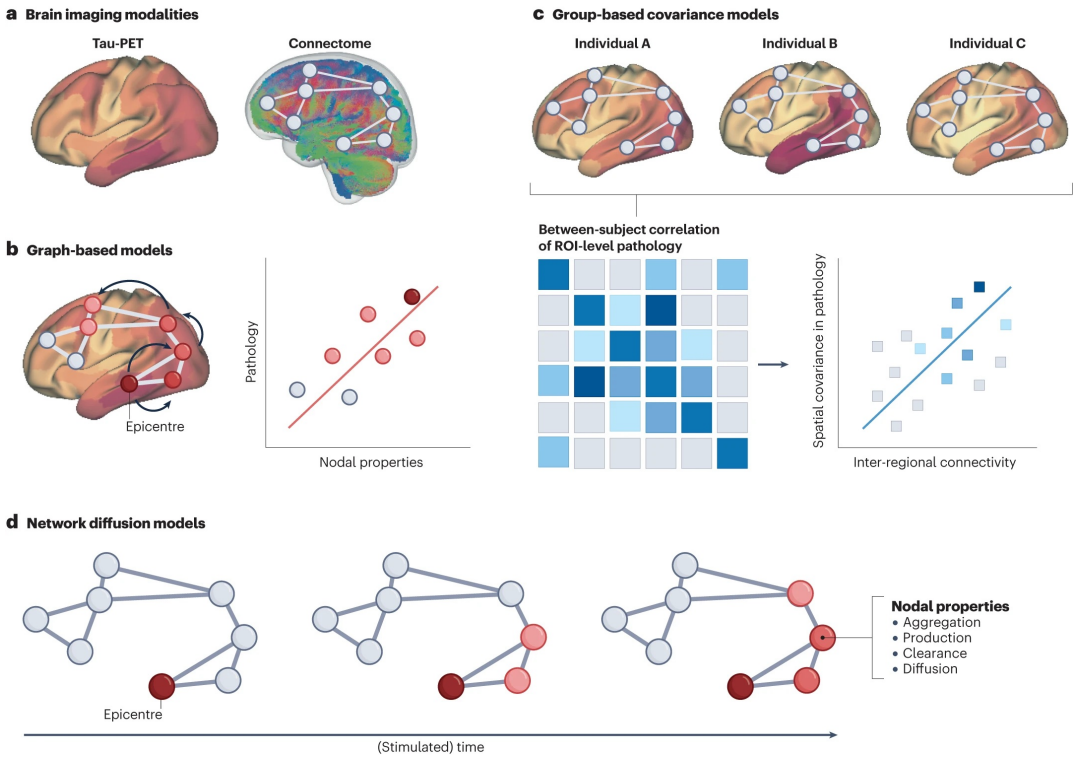

Figure 2.3: Methods for assessing the influence of network architecture on disease progression [22].

2.6 Diagnosis of neurodegenerative diseases

The diagnosis of neurodegenerative diseases is a complex process that requires a multidisciplinary approach: there is no single definitive test, but rather, analyses from different clinical symptoms are combined with a series of instrumental and biological examinations.

In the case of AD, the first step towards diagnosis is taken through a targeted and detailed clinical assessment of the patient's cognitive condition. The diagnostic criteria used are those proposed by the National Institute on Aging and Alzheimer's.

The clinical evaluation is supported by instrumental examinations, such as Magnetic Resonance Imaging (MRI) useful for identifying possible cerebral atrophies, in particular in the hippocampus, or Computerized Tomography (CT), less sensitive than the former but useful for ruling out other pathologies, and Positron Emission Tomography (PET). The latter is fundamental for making the diagnosis: FDG (fluorodeoxyglucose) PET assesses cerebral metabolism, while amyloid PET detects the accumulation of β-amyloid plaques.

It is also possible to carry out analysis of the cephalorachid fluid (CSF), which may show a decrease in β-amyloid, thus an accumulation of plaques, or an increase in tau protein, associated with the formation of neurofibrillary tangles. These biomarkers are useful for confirming the diagnosis and differentiating AD from other dementias.

After confirmation of the presence of the disease, patients can be categorized according to the severity of their symptoms.

3. Reaction-Diffusion Models

3.1 Diffusion models for neurodegenerative diseases

Prion diseases are characterised by a series of chain reactions in which misfolded infectious proteins induce healthy counterparts to adopt the same pathogenic conformation, distinct from their physiological structure. These diseases display unique kinetic characteristics:

1. Disease progression becomes inevitable once prion production processes are initiated;

2. The length of the incubation period depends on both the initial concentration of pathological proteins and the rate at which they replicate;

3. The disease course is marked by a prolonged and silent incubation phase, during which prions accumulate and spread, followed by a brief but fatal symptomatic period [14].

Since the initial identification of these diseases, researchers have been trying to develop mathematical models capable of capturing the above-mentioned features. The main difficulty encountered was that early models focused on producing repeatable and predictive results, but were not based on the physical mechanisms that regulate protein diffusion. Initial studies primarily investigated individual seeding events involving monomeric or polymeric proteins that could induce misfolding in native proteins. Over time, however, the focus shifted towards understanding the diffusion of prion-like proteins within the cerebral cortex and the resulting cognitive and behavioural consequences. This shift proved essential for differentiating between symptoms and improving diagnostic specificity.

To date, most hypotheses and extensive research suggest that pathological proteins in neurodegenerative diseases propagate through mechanisms similar to those of prions, spreading progressively throughout the brain along anatomically connected neural networks [10]. Moreover, reaction-diffusion models, rooted in physical principles governing molecular diffusion, have successfully described the growth and propagation of misfolded proteins in diseases such as Alzheimer's (AD), Parkinson's (PD), and Amyotrophic Lateral Sclerosis (ALS). This is possible because, despite differences in clinical and pathological features, these disorders share fundamental molecular properties with prion diseases: nucleation, growth, and spreading.

One of the major challenges in studying disease progression lies in the fact that the first clinical symptoms of cognitive decline typically appear one or two decades after the initial cellular abnormalities have begun to emerge in the brain. As a result, obtaining data from the earliest stages of the disease remains particularly difficult.

Figure 3.1 illustrates the propagation of pathological proteins associated with different neurodegenerative diseases — tau and β-amyloid in Alzheimer's disease (AD), α-synuclein in Parkinson's disease (PD), and TDP-43 in Amyotrophic Lateral Sclerosis (ALS) — across three distinct stages of disease progression, highlighting the spatial patterns of protein aggregation in each case.

Post-mortem studies conducted on several hundred human brains have consistently confirmed the progression patterns depicted in the figure, which have therefore become the basis for repeatable and predictive models. In AD, for example, plaque accumulation caused by β-amyloid proteins has been repeatedly observed to begin in the neocortex and then spread to subcortical regions, as shown in the first row in orange [20]. In the same disease, tau protein aggregation, represented in blue in the second row, originates in the *locus coeruleus* and subsequently extends to the entire cerebral cortex [2]. In PD, the presence of α-synuclein proteins, highlighted in red in the third row, is first detected in the motor nucleus and the olfactory bulb, from which it later spreads to additional brain areas [3]. The fourth row, shown in green, depicts the accumulation of TDP-43 proteins in ALS, which begins in the motor cortex and later involves the neocortex and brainstem [4].

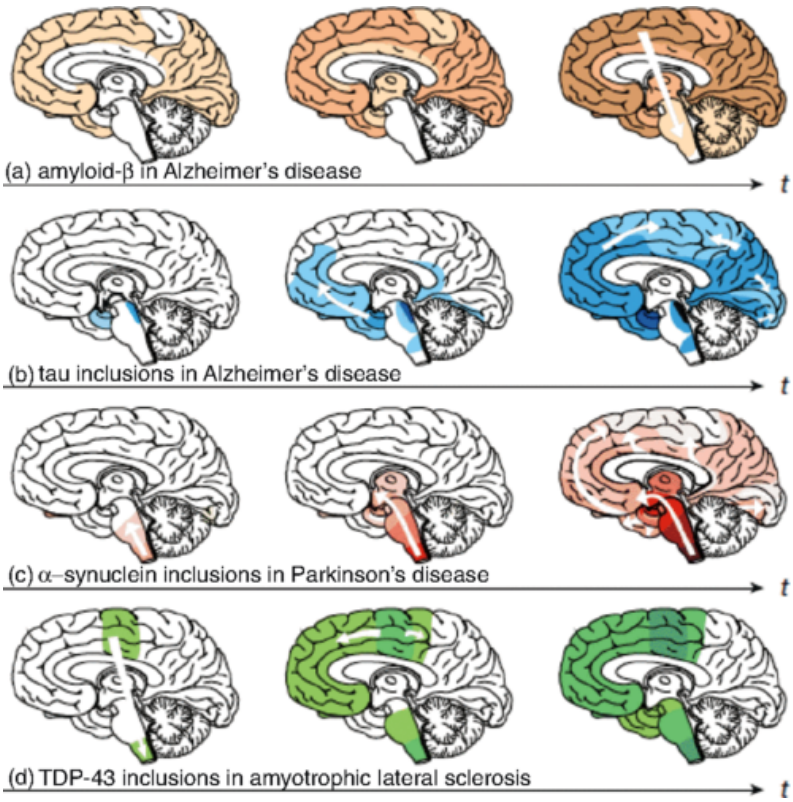

Figure 3.1: Characteristic progression of the accumulation of pathologic specific proteins in neurodegenerative diseases deduced from post-mortem brain analyses. Respectively, from top to bottom, β-amyloid protein deposits in Alzheimer's disease, tau inclusions in Alzheimer's disease, α-synuclein inclusions in Parkinson's disease, and TDP-43 inclusions in amyotrophic lateral sclerosis. Three stages of progressive neurodegeneration are shown, from left to right, with white arrows indicating the possible spread of lesions [26, 12].

Despite these advances, modelling neurodegeneration remains an open challenge. A common goal is to develop a model capable of explaining why disease progression becomes inevitable after the initial protein accumulation e why it proceeds so slowly in the early stages and then accelerates dramatically in later phases.

3.2 Diffusion models for Alzheimer's disease

The prevailing theory in neurodegeneration research suggests that, in Alzheimer's disease (AD), tau proteins within healthy axons behave similarly to prions, undergoing misfolding and progressively forming larger aggregates of pathological proteins that propagate throughout the brain. To understand how the disease advances, it is first essential to examine both the mechanisms of molecular misfolding and the biophysical principles that regulate their diffusion within the cortical structure. To address these challenges, researchers have proposed three main mathematical approaches, each capturing different aspects of the underlying biological complexity:

1. Kinetic growth and fragmentation models, which simulate local molecular interactions between misfolded and normally folded protein aggregates of varying sizes. These models typically rely on systems of ordinary differential equations (ODEs) and are useful for studying the nucleation and elongation dynamics at the microscopic scale.

2. Network diffusion models, founded on graph theory, which describe the macroscopic propagation of misfolded proteins through anatomically defined brain networks. These models treat the brain as a system of interconnected nodes (regions) and edges (axonal pathways), allowing researchers to simulate the spread of disease from seed sites along connectivity pathways.

3. Continuum models, based on reaction-diffusion equations, which provide a spatially continuous representation of protein spread over time. These models use partial differential equations (PDEs) to describe the evolution of pathogenic proteins as a function of both molecular kinetics and anisotropic diffusion along fiber tracts.

Figure 3.2 illustrates the typical spatio-temporal progression of misfolded tau protein spread in AD. The three rows depict: (a) clinical observations from imaging data, (b) results from continuum modelling, and (c) outcomes from network diffusion modelling [10]. The simulation in the second row is based on a non-linear anisotropic reaction-diffusion model, which captures both the directional transport of tau along white matter tracts and the local amplification of misfolded aggregates. Although this approach is highly accurate and closely aligns with clinical observations, it is also computationally onerous, as it requires finely resolved spatial data and complex numerical solvers. The third row model, on the other hand, employs the principles of graph theory to simulate protein diffusion along a discrete network of brain regions. This method simplifies anatomical geometry, allows scalable calculations and facilitates the integration of patient-specific connectivity data.

Moreover, hybrid strategies are now being explored, combining the spatial accuracy of continuum models with the efficiency of network-based approaches. These integrative

methods aim to achieve a balance between biological precision and computational feasibility, potentially enabling real-time simulation of disease spread in individual patients based on neuroimaging data.

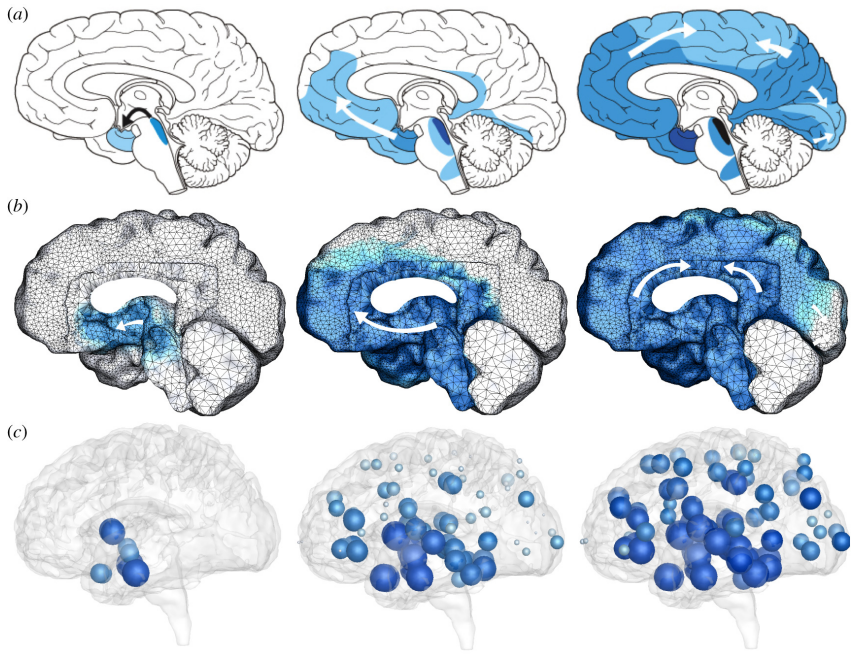

Figure 3.2: Study of the typical diffusion of misfolded tau protein in Alzheimer's disease. Respectively, starting from the top, the clinical observation (a), the continuum model (b) and the diffusion model implemented through graph theory (c) are illustrated. In all three paradigms it can be seen that the accumulation of misfolded tau occurs first in the *locus coeruleus*, and then spreads to the transentorhinal region and entorhinal cortex. It progressively spreads to all interconnected neocortical brain regions [10].

3.3 Fisher-Kolmogorov model

The Fisher-Kolmogorov model, frequently used in the literature for the study of protein misfolding, is the most widely adopted model [10]. It is commonly used to describe population dynamics and travelling wave solutions in a variety of fields. It is based on a non-linear reaction-diffusion equation for an unknown component u, which in this case represents the concentration of misfolded proteins:

$$\frac{du}{dt} = \nabla \cdot (\mathbf{D}\nabla u) + \alpha u(1-u) \tag{3.1}$$

where $\mathbf{D}$ is the diffusion tensor that characterizes global protein spreading and α characterizes the local conversion rate from the healthy to the misfolded state.

Equation (3.1) has two steady-state solutions: an unstable one for $u = 0$, and a stable one for $u = 1$. This implies that once the misfolded protein is present everywhere in the brain, $u > 0$, the concentration will tend to veer toward the misfolded state, $u = 1$.

Of particular interest is the parameter α, which is purely phenomenological and does not provide information about the mechanisms inherent in the current infection. It also cannot capture intermediate equilibrium states such as, for example, the result of drug treatment [10]. One can model the presence of misfolded proteins in a specific area of the brain from which diffusion will begin with non-homogeneous initial conditions, $u_0 > 0$. Within the $\mathbf{D}$ tensor, the part of diffusion that occurs extracellularly will be denoted by the coefficient d^{ext}, and that which occurs by axonal transport, thus along the $\boldsymbol{n}$ direction, will be enclosed in d^{axn}:

$$\mathbf{D} = d^{ext}\mathbf{I} + d^{axn}\boldsymbol{n} \otimes \boldsymbol{n}$$

Prion cells are known to be transported with high specificity along established anatomical pathways, and it is generally assumed that axonal transport is faster than extracellular diffusion. [25]

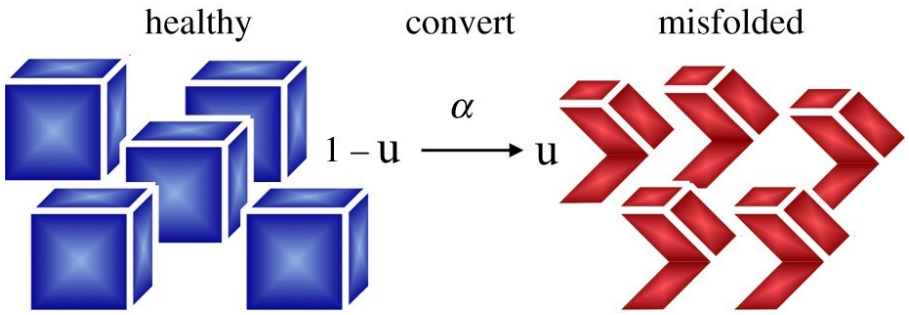

Figure 3.3: Fisher-Kolmogorov model kinetics. The model has only one unknown, namely the concentration of misfolded proteins u, and converts healthy proteins to misfolded proteins with rate α. In the presence of a small perturbation from the healthy state, $u > 0$, all proteins will convert to the misfolded state, $u = 1$ [10].

3.4 Interaction model between proteins

Recent studies have shown that Alzheimer's disease (AD) is characterized by the progressive and widespread accumulation in the brain of two distinct pathological proteins: β-amyloid (Aβ) and tau. The progression of AD involves the deposition of Aβ plaques in the cortex and the formation of neurofibrillary tangles composed of misfolded tau protein.

Aβ typically first appears in the frontal regions of the cerebral cortex and subsequently spreads to other cortical and subcortical areas. According to the prevailing 'amyloid cascade hypothesis', the abnormal accumulation of Aβ acts as the upstream trigger of the pathological process, initiating a cascade of downstream events, including the misfolding, aggregation, and atypical propagation of tau. However, this hypothesis alone has proven insufficient to fully explain the complexity of AD pathogenesis. As a result, alternative mechanisms have been proposed, many of which emphasize the critical and possibly independent role of tau in disease progression. In particular, growing experimental and mechanistic evidence indicates that Aβ facilitates the aggregation of tau and accelerates

its diffusion across the brain, thereby influencing the extent of neurodegeneration and cognitive decline.

Among the most compelling of these alternative frameworks is the concept of network-based propagation. Unlike conventional models that assume purely spatial diffusion, recent neuroimaging studies suggest that both Aβ and tau propagate preferentially along axonal projections, following the architecture of the brain's structural connectome. Through this trans-neuronal mechanism, the two proteins can interact locally, while the effects of their interaction propagate through neural circuits to distant brain regions. This may explain the distinct and often non-overlapping spatial distributions of Aβ and tau observed at different stages of the disease. Consistent with these observations, numerous mathematical models have been developed to investigate the dynamics of their interaction. Among these, spatio-temporal reaction-diffusion models of tau — augmented by secondary diffusion terms reflecting Aβ-driven facilitation of tau aggregation — have emerged as some of the most robust and widely accepted approaches for capturing the coupled progression of the two proteinopathies in Alzheimer's disease [18].

The brain's anatomical connectivity network is represented by the graph $G = \{V, E\}$, where the nodes $v_i \in V$, $i \in [1, \mathrm{N}]$ represent distinct grey matter regions of the brain, and the edges $e_{i,j} \in E$ correspond to the axonal fibre connections between them. Two time-dependent vectors, $\mathbf{u}_{A\beta}$ and $\mathbf{u}_{tau}$, are defined to describe the concentration levels of Aβ and tau, respectively, at each node.

A model is proposed below that integrates the production of the two proteins, their diffusion, and their interaction:

$$\frac{d\mathbf{u}_{tau}}{dt} = -\delta H \mathbf{u}_{tau} + \alpha f_{tau} e_{EC} \tag{3.2}$$

$$\frac{d\mathbf{u}_{A\beta}}{dt} = -\delta H \mathbf{u}_{A\beta} + \alpha f_{A\beta}(\mathbf{m} \cdot \mathbf{u}_{APP}) \tag{3.3}$$

where the equation (3.2) represents the evolution of the diffusion of the tau protein and the equation (3.3) that of the β-amyloid protein.

Diffusion of both tau and β-amyloid proteins is modelled through the Laplacian matrix of the connectome H and a diffusivity rate δ, which depends on the concentration gradients of the protein under consideration and the degree of connectivity between regions. This approach aims to capture trans-neuronal propagation as an active axonal transport process, in which fibre length is considered negligible and does not significantly influence diffusion.

In the equation describing tau protein dynamics, a focal seeding term, $\alpha f_{tau} e_{EC}$, is included, originating in the entorhinal cortex (EC), identified as the sole region responsible for producing the misfolded protein. All other regions are assumed incapable of tau synthesis and contribute only to its transport and aggregation.

In contrast, the equation modelling β-amyloid dynamics employs the same diffusion framework used for tau, incorporating the term $\alpha f_{A\beta}(\mathbf{m} \cdot \mathbf{u}_{APP})$. This includes a production term proportional to both the region's baseline metabolic activity $\mathbf{m}$, as measured by FDG-PET in healthy individuals, and the local availability of Amyloid Precursor Protein, $\mathbf{u}_{APP}$, from which Aβ is generated.

Since the onset of production is gradual, followed by a possible decline and plateau, the production terms are modulated by long-duration Gamma-shaped driving functions f_{tau} and $f_{A\beta}$, which describe the temporal evolution of protein synthesis [18].

Several studies have investigated the coexistence of β-amyloid protein and tau proteins within brain regions. The model with the strongest empirical support is presented below. It describes a unidirectional interaction, in which β-amyloid is hypothesised to promote tau aggregation. Equation (3.2) is modified as follows:

$$\frac{d\mathbf{u}_{tau}}{dt} = -\delta H \mathbf{u}_{tau} + \alpha f_{tau} e_{EC} + \gamma \mathbf{u}_{A\beta} \mathbf{u}_{tau}(k - \mathbf{u}_{tau}) \tag{3.4}$$

The last term, $\mathbf{u}_{tau}(k-\mathbf{u}_{tau})$, represents a logistic growth component, where tau accumulation is promoted by local concentrations of Aβ, but saturates as tau approaches a maximal capacity k. This formulation ensures biological plausibility by preventing indefinite growth.

3.5 Integration of the connectome structure

Recent theories regarding the structure of the connectome have laid the groundwork for the development of diffusion models that incorporate brain network architecture [22].

In neurodegenerative diseases, such as Alzheimer's, Parkinson's, and Huntington's, the connectome is thought to facilitate the spread of pathological proteins, enabling their propagation even between non-adjacent regions. The application of these models marked a significant turning point: a strong spatial correlation was observed with patterns of grey matter atrophy. In Alzheimer's disease in particular, longitudinal diffusion data revealed that the architecture of the human brain network is sufficiently predictive of the regional accumulation of tau protein. These findings were further supported by studies in murine models of neurodegenerative disease: when applied to the mouse brain connectome, diffusion models yielded accurate predictions of axonal tracing following inoculation, allowing for the investigation of disease progression over time.

A current limitation of these models is their lack of a term representing the system's resistance — that is, factors capable of modulating the rate of protein accumulation. These factors could either accelerate or slow down the local spread of misfolded proteins, depending on the biological environment. Only in recent adaptations of epidemic spreading models has this limitation begun to be addressed. In particular, some studies have introduced both production and clearance terms to model the dynamics of pathogen load at the level of individual brain regions.

Nonetheless, many avenues remain open for improving the biological realism of such models. This is especially true given that axonal transport mechanisms are the subject of ongoing research. Moreover, emerging theories increasingly regard the connectome not merely as a passive conduit but as an active substrate that participates in protein production and propagation within physiological processes.

3.6 Brain network model

In order to model the diffusion of proteins through the connectome structure, the latter can be represented as a weighted graph G, consisting of N nodes and E edges [10].

The graph G was derived from diffusion tensor MRI scans of 418 subjects included in the Human Connectome Project [15], using data from the Budapest Reference Connectome v3.0 [19]. The original high-resolution graph G comprised $N = 1015$ nodes and $E = 37477$

edges. For modelling purposes, this was coarse-grained to a graph with $N = 83$ nodes and $E = 1130$ edges. Each edge in the graph is weighted by the average number of fibres n_{IJ} present in each region of the brain, which have a length between 11.3 mm and 136.8 mm and denoted by l_{IJ}.

The connectivity structure of the graph G can be summarised using two matrices: the diagonal degree matrix $\mathbf{D} = diag\{D_{II}\}$ involving the degree of each node I, and the weighted adjacency matrix $\mathbf{A}$, where each entry is proportional to the ratio of mean fiber number and length between nodes I and J. The difference between the matrices $\mathbf{D}$ and $\mathbf{A}$ is defined as a weighted graph Laplacian $\mathbf{L}$.

$$\mathbf{L} = \mathbf{D} - \mathbf{A} \quad \text{with} \quad A_{IJ} = \frac{n_{IJ}}{l_{IJ}} \quad \text{and} \quad D_{II} = \sum_{J=1}^{N} A_{IJ} \tag{3.5}$$

Assuming that the parameter L_{IJ} characterizes the diffusion of healthy and misfolded proteins through the brain network, the Fisher-Kolmogorov model can be discretized on the weighted graph G. Equation (3.1) becomes

$$\frac{du_I}{dt} = -\sum_{J=1}^{N} L_{IJ} u_J + \alpha u_I (1 - u_I) \tag{3.6}$$

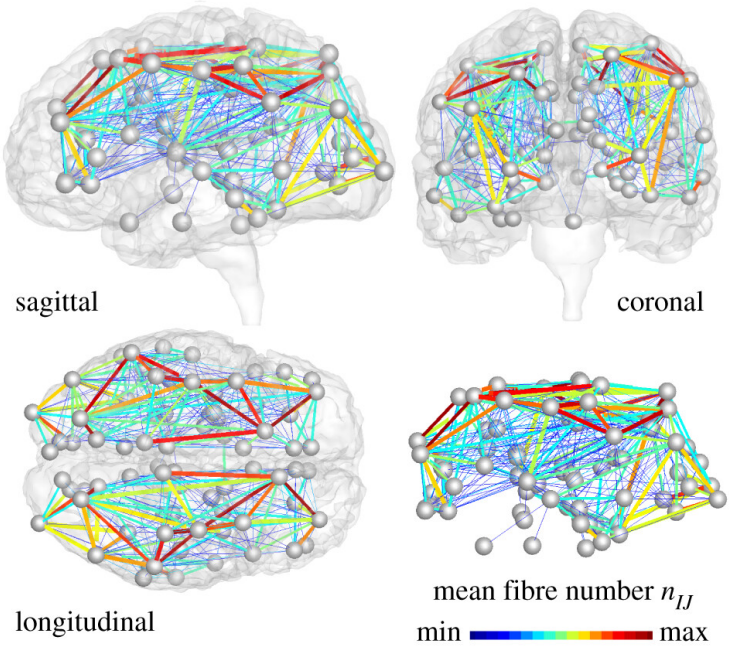

Figure 3.4: Brain network model. The propagation of misfolded tau proteins is modelled over the brain connectome, represented as a weighted graph G with $N = 83$ nodes and $E = 1130$ edges. Each edge weight is defined as the ratio between the average number of fibres n_{IJ} and their average length l_{IJ} computed from diffusion MRI data of 418 healthy subjects in the Human Connectome Project [24].

4. The Numerical Brain

4.1 Overview of work performed

The simulations were performed using COMSOL Multiphysics, a finite element analysis software, on a three-dimensional geometry generated from an imported mesh designed to represent the so-called 'ideal brain' and its associated connectome structure.

The brain model was obtained by converting the imported mesh into a solid three-dimensional domain suitable for numerical analysis. This domain was then subdivided on its surface into fourteen distinct zones, corresponding to the main anatomical macro-areas. This subdivision is considered 'ideal' because it does not alter the original geometry, mesh resolution or simulation results, but rather serves as a visual and analytical reference to provide a clearer understanding of the spatial location of these regions within the brain.

In this anatomical framework, the connectome was explicitly modelled as a network of ten three-dimensional channels embedded within the brain geometry. These channels represent the principal fibre tracts that form the macrostructural connectivity network, facilitating long-range communication between disparate brain regions.

Protein diffusion processes were implemented through coupled reaction-diffusion equations defined at the brain surface and within the connectome channels. The reaction terms account for local protein aggregation and production, while diffusion is governed by spatial gradients and the adjacency matrix derived from the connectome. Diffusion within the connectome channels was modelled as effectively instantaneous with respect to diffusion through surrounding brain tissue, reflecting their role as primary conduits for trans-neuronal propagation of pathological proteins.

Time-dependent simulations were carried out over a 40-year period, with output data recorded at 6-month intervals. This temporal discretization was selected to accurately capture the slow progression of neurodegenerative pathology, enabling detailed mapping of protein accumulation and spread over clinically relevant timescales. However, when the model is applied to a selected cohort of patients, simulations are conducted over a 30-year period to better reflect individual disease progression within that time-frame.

The results of these simulations will provide a comprehensive picture of disease progression, highlighting the temporal evolution of misfolded protein concentrations within each brain region as model parameters governing the reaction-diffusion processes are varied. In the case of the studied patients, simulated data will be compared against their individual PET imaging results to assess the model's predictive accuracy. Furthermore, the dynamics of the model's key parameters will be traced to evaluate their impact on the progression and characteristics of the disease.

4.2 Meshing construction

The initial mesh was obtained using a series of processing pipelines available within the FreeSurfer software suite, applied to the MNI template — commonly referred to as the 'ideal' subject and widely adopted as a standard anatomical reference in neuroimaging studies.

In particular, the 'recon_all' pipeline was used to reconstruct cortical surfaces from raw MRI data. Subsequently, the 'mris_convert' tool was employed to export the surface data into STL format, thereby enabling compatibility with the COMSOL Multiphysics environment.

The original mesh derived from the STL file includes 261722 surface elements, 18323 edges, and 12745 vertices. This extremely dense structure, while anatomically detailed, initially posed a significant computational burden for the numerical solution of the model. To overcome this problem, a mesh simplification process was applied, aimed at reducing the number of elements while preserving the essential morphological features of the three-dimensional brain surface. This preprocessing step allowed for a more computationally efficient model implementation without compromising anatomical fidelity.

The complexity of the imported mesh can be seen in the left-hand side of the figure 4.1; the right-hand side shows the simplified mesh. The figure also shows three views of the cerebral cortex thus obtained. The latter represents the right hemisphere and forms the geometric basis for the simulations described above. Specifically, the first view shows the entire hemisphere, providing an overall perspective of the structure; the second illustrates the outer cortical surface, corresponding to a lateral view; and the third presents the internal cortical surface, offering a medial view of the anatomy.

These visualisations effectively convey the level of detail of the original mesh prior to simplification and highlight its anatomical consistency, which was maintained throughout the modelling process.

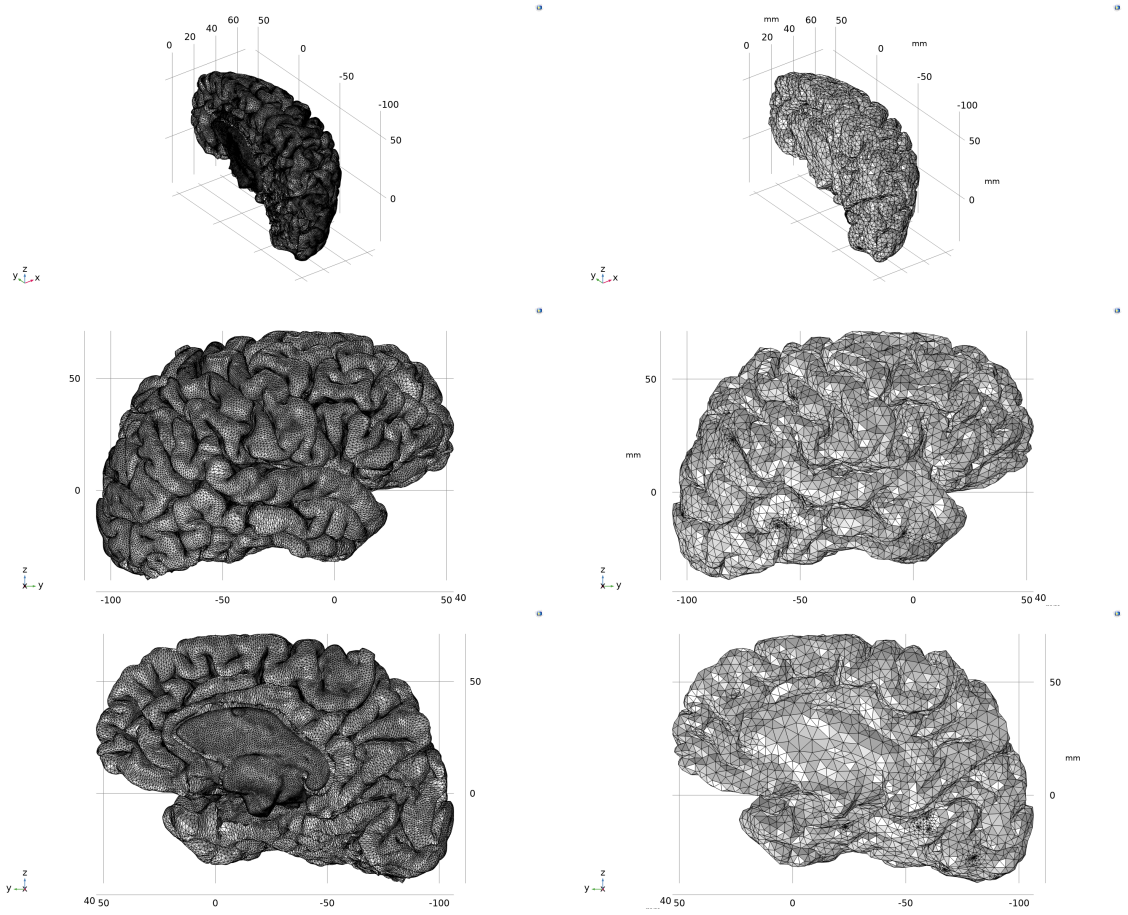

Figure 4.1: Left: original cortical mesh obtained from the STL file. Right: refined and simplified version of the mesh, used for the simulations presented in this study. The first row displays the entire right hemisphere, the second shows the external (lateral) surface of the cortex, and the third illustrates the internal (medial) surface.

4.3 Ideal brain

From the detailed construction of the mesh described above, the focus is now on the so-called 'ideal brain', a geometric framework crucial for simulations. This structure comprises the grey matter and cortical regions and is derived from the T1-weighted magnetic resonance imaging (T1w-MRI) template known as the 'MNI152_template'. This template is generated through the averaging and co-registration of thousands of individual MRI scans, and it is widely acknowledged as a standard anatomical reference in neuroimaging studies [7, 9, 8].

The extensive dataset forming the foundation of the 'MNI152_template' originates from the Human Connectome Project, with data processing and analysis coordinated by the WU-Minn consortium, the McDonnell Center for Neuroscience Systems at Washington University, alongside other NIH-supported neuroscience research centers. This rigorous data processing ensures that the 'ideal brain' template accurately captures normative brain anatomy, providing a robust and reproducible basis for computational modeling.

In the COMSOL Multiphysics environment, the cortical surface mesh previously imported in STL format was converted into a solid three-dimensional geometry. This conversion preserves the anatomical detail inherent in the original mesh, while enabling the implementation of reaction-diffusion simulations directly on the brain surface.

Figure 4.2 presents multiple perspectives of this three-dimensional structure, illustrating the anatomical fidelity of the model and its suitability for simulating protein diffusion dynamics within the brain. Fourteen distinct anatomical regions of interest were delineated on the surface of the brain model. The colours used to identify each zone in the list below correspond exactly to those depicted in figure 4.2, enabling a direct visual correlation between the anatomical structures and their spatial localization on the cortical surface. This subdivision facilitates the analysis of protein diffusion dynamics and pathological progression in relation to specific brain regions.

The following describes each region's functional relevance and potential implications of pathological alterations as modelled in the study.

1. Inner zone: composed primarily of white matter, this region is assumed to be unaffected by the propagation of pathological proteins.

2. Temporal zone: involved in auditory perception, visual memory, and affectivity. Lesions in the right temporal lobe impair interpretation of non-verbal auditory stimuli, whereas damage to the left side affects visual recognition, memory, and language functions.

3. Occipital zone: includes the primary visual cortex and visual association areas. Pathology here can result in visual perception deficits and difficulties in spatial understanding.

4. Parietal zone: encompasses the somatosensory cortex, responsible for sensory and tactile processing, and the parietal cortex, involved in language, calculation, spatial orientation, and memory. Lesions may cause impaired processing of simultaneous stimuli and reduced spatial awareness.

5. Frontal zone: responsible for voluntary motor control, language production (both spoken and written), and emotional regulation. Damage often leads to cognitive and behavioural disorders as well as diminished empathy.

6. Mid-frontal zone: along with the frontal zone, this area underpins long-term memory, attention control, and personality traits. Protein aggregation here is associated with planning and decision-making difficulties.

7. Upper-frontal zone: located at the uppermost surface of the frontal lobe, it supports self-awareness and integration with sensory processing areas.

8. Cingulate zone: interfaces with subcortical structures and plays a key role in affective processing, acting as a bridge between emotions and cognition.

9. Zone of the wedge: a subsection of the occipital lobe that receives direct visual input from the retina.

10. Language zone: specializes in language comprehension, semantics, and speech production planning. Lesions can cause impairments in both spoken and written communication.

11. Hippocampal zone: crucial for memory formation, including short- and long-term memory, and spatial orientation. It integrates signals from multiple brain areas and is one of the earliest regions affected by Alzheimer's disease.

12. Entorhinal zone: heavily involved in memory formation and commonly referred to as the 'house of memories'. It is typically the first cortical region to exhibit protein accumulation in Alzheimer's pathology.

13. Sensorial zone: processes sensory inputs from the five senses. Lesions can result in disturbances across vision, hearing, touch, taste, and smell.

14. Central zone: governs voluntary motor control, behavioural planning, attention regulation, and impulse control. Damage may lead to disinhibition of action,, expressive aphasia, abulia, apathy, and impaired executive functioning.

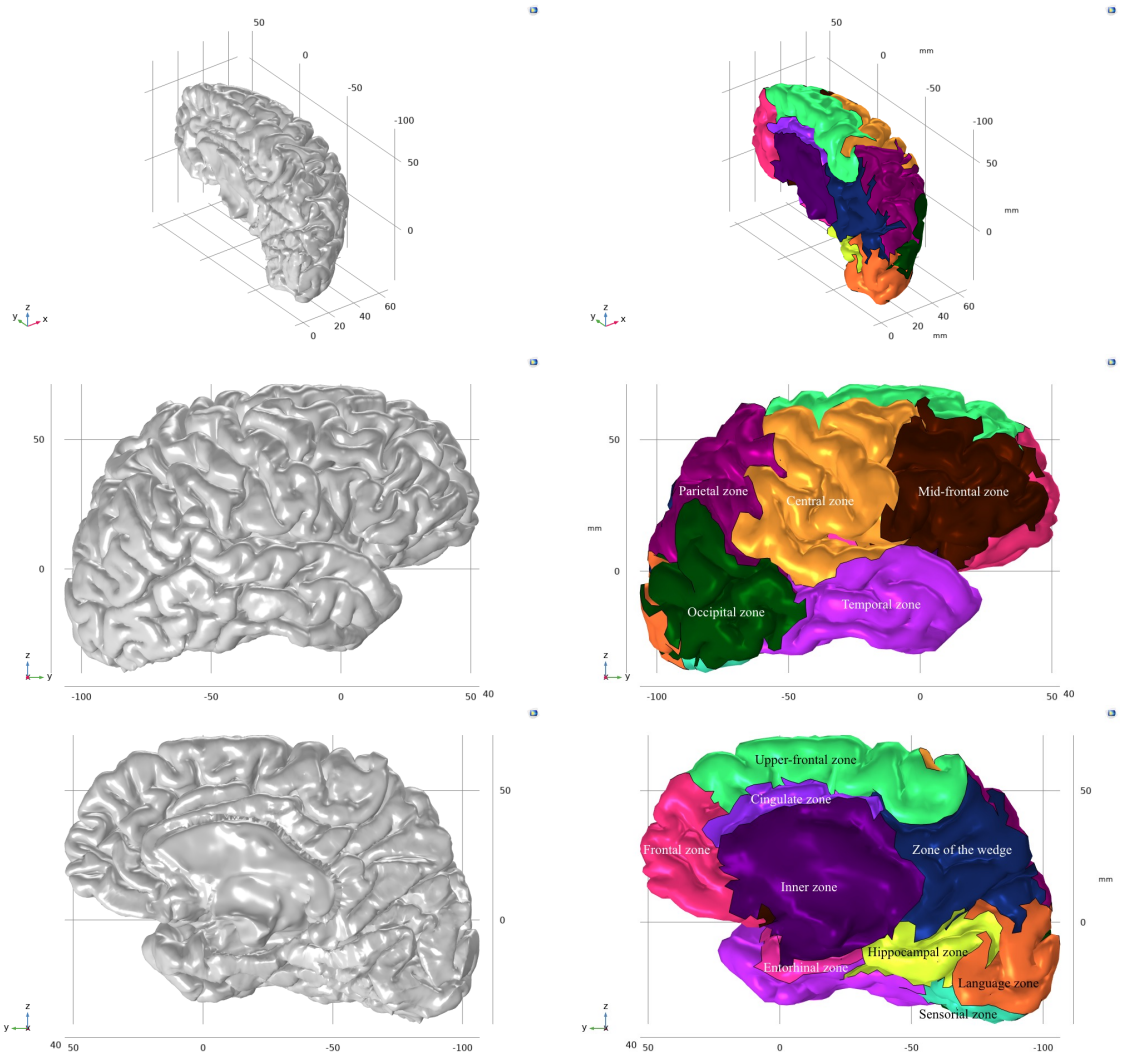

Figure 4.2: Left: three-dimensional structure of the analysed portion of the brain created from the starting mesh. Right: three-dimensional structure divided into the fourteen areas of interest described above, with colors corresponding to those used in the list for each region. In the external view of the cerebral cortex, the parietal, occipital, central, temporal, superior frontal, middle frontal and frontal areas can be distinguished. In the internal view of the brain, the entorhinal, inner, hippocampal, language, sensory, wedge, cingulate and the remaining portions of the superior frontal, frontal and temporal areas are observed.

4.4 Construction of the connectome structure

The connectome structure within the brain was represented by the construction of ten cylindrical channels, each with a radius of 0.1 *mm* and varying lengths and curvatures. These channels serve as conduits connecting distant brain regions, facilitating rapid transport of protein diffusion between areas. In the simulations, a pure diffusion equation — devoid of any reaction or production terms — was applied exclusively to these connecting channels to accurately model protein transport along the connectome pathways.

The resulting geometric configuration of the connectome is illustrated in figure 4.3.

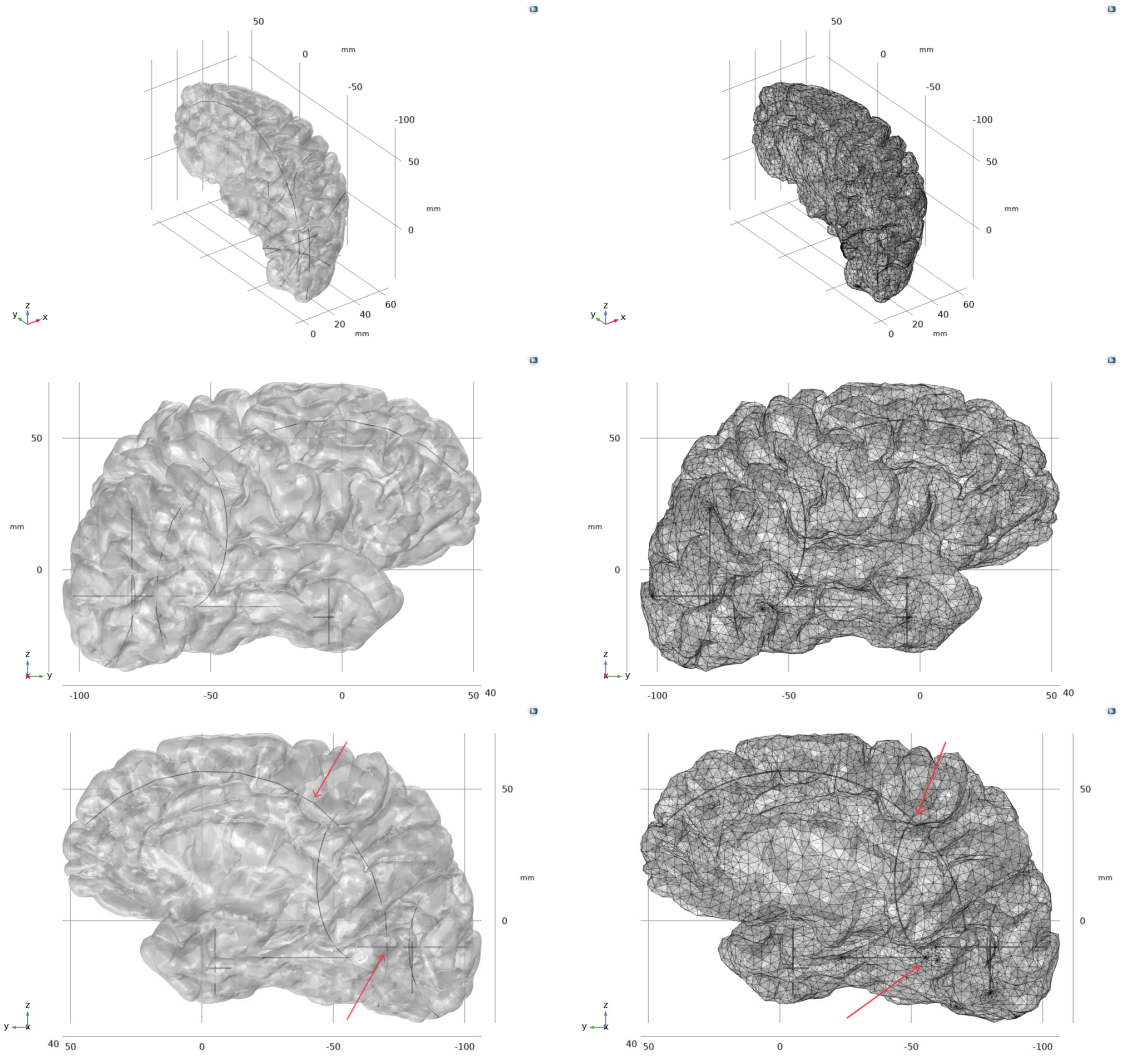

Figure 4.3: Left: integration of the connectome structure, respectively for the whole, frontal and inner vision of the portion of cerebral cortex considered. Right: integration of the connectome structure within the total meshwork of the cerebral cortex, in the three realised views. The red arrows indicate some of the channels that are part of the connectome structure.

To model the connectivity between specific brain regions mediated exclusively by the connectome domain — subsequently referred to in the mathematical model as Ω_c — a binary adjacency matrix $\mathbf{A}_c$ was constructed.

This matrix was derived directly from the three-dimensional geometry of the connectome designed in COMSOL Multiphysics and shown in figure 4.3, consisting of cylindrical channels physically connecting distant cortical areas. Each element $\mathbf{A}_{c,IJ}$ of the matrix takes the value 1 if there exists a direct connection between regions I and J, and 0 otherwise.

Although inspired by the network-based formulation presented earlier in (3.5), this matrix is not directly involved in the numerical simulations; instead, it serves as a schematic representation of the anatomical connectivity realized in the COMSOL model and offers a concise overview of how the constructed connectome channels link the defined cortical regions. The same structural logic underlies the discretised diffusion network described by the Fisher-Kolmogorov-type equation (3.6).

	1.	2.	3.	4.	5.	6.	7.	8.	9.	10.	11.	12.	13.	14.
1.	0	0	0	0	0	0	0	0	0	0	0	0	0	0
2.	0	0	0	0	0	0	0	0	0	0	0	1	0	1
3.	0	0	0	0	0	0	0	0	0	0	1	0	0	1
4.	0	0	0	0	0	0	0	0	0	1	0	0	0	0
5.	0	0	0	0	0	0	0	0	0	0	0	0	1	0
6.	0	0	0	0	0	0	0	0	0	0	0	0	0	0
7.	0	0	0	0	0	0	0	0	0	0	0	0	0	0
8.	0	0	0	0	0	0	0	0	0	0	0	0	0	0
9.	0	0	0	0	0	0	0	0	0	0	0	0	1	0
10.	0	0	0	1	0	0	0	0	0	0	0	0	0	0
11.	0	0	1	0	0	0	0	0	0	0	0	1	0	0
12.	0	1	0	0	0	0	0	0	0	0	1	0	0	0
13.	0	0	0	0	1	0	0	0	1	0	0	0	0	0
14.	0	1	1	0	0	0	0	0	0	0	0	0	0	0

Table 4.1: Binary adjacency matrix representing the presence (value 1, highlighted in yellow) or absence (value 0) of structural connections between cortical regions. The matrix is constructed from the three-dimensional geometry of the connectome designed in COMSOL Multiphysics. It schematically encodes the connectivity pattern imposed by the cylindrical channels linking distant brain areas, as shown in figure 4.3.

The adjacency matrix introduced above encodes the presence or absence of structural connections between brain regions, based on the three-dimensional geometry of the connectome. To model diffusion exclusively through these connecting channels, it is necessary to consider an effective diffusion coefficient that accounts for the combined transport properties of multiple microchannels. It is assumed that the connectome can be approximated as a set of microchannels, which collectively behave like a single flow conduit. Let each channel have a flow rate denoted by $\vec{q_i}$ with the simplifying assumption that all $\vec{q_i}$ are approximately equal.

Thus, the total flow rate $\vec{q_H}$ through the equivalent conduit is given by:

$$\sum_i \vec{q_i} = \vec{q_H}$$

Applying Fick's law to each microchannel,

$$\vec{q_i} = -D_i \nabla u_i$$

where the u_i represents the concentration in channel i. Summing over all channels yields an effective diffusion process described by:

$$\sum_i (-D_i \nabla u_i) = -D_{eff} \nabla U_H$$

where D_{eff} and U_H are the effective diffusion coefficient and overall concentration in the combined structure, respectively.

This reasoning relies on the following assumptions:

1. The concentrations u_i within the channels are sufficiently similar to each other to approximate their sum by U_H leading to the relation:

$$\sum_i -d_i \left(\frac{\partial u_i}{\partial s} \right) = - \left(\sum_i d_i \right) \frac{\partial u}{\partial s}$$

2. The diffusion coefficients d_i are the same between the channels, therefore:

$$- \left(\sum_i d_i \right) \frac{\partial u}{\partial s} = -D_{eff} \frac{\partial u}{\partial s}$$

   Since concentration gradients are non-zero, it follows that

$$\sum_i d_i = D_{eff}$$

   In order to implement this concept within COMSOL Multiphysics for visualization, the parameter N was introduced such that

$$N d_i = D_{eff}$$

In the simulations, $N = 10^6$ is used to scale the diffusion coefficient within the connectome channels, effectively capturing the combined transport capacity of a large number of microchannels. This adjustment reflects the modelling assumption that the connectome acts as a densely packed bundle of homogeneous channels, each contributing equally to the overall diffusion process.

5. Mathematical Models

5.1 Model 1: Diffusion pattern of tau protein

Tau protein, which is responsible for the onset of Alzheimer's disease, was modelled in terms of its diffusion within the brain using a reaction-diffusion system derived from the Fisher–Kolmogorov framework, as presented in equation (3.1). As shown in figure 3.2, tau pathology initially emerges in the *locus coeruleus*; therefore, in the simulations, the entorhinal cortex was chosen as the starting region for tau propagation, as it is spatially aligned and biologically connected to this site.

The model, implemented in COMSOL Multiphysics, is formulated as a system of partial differential equations defined on the surface Ω of the cerebral cortex. This system describes the spatio-temporal evolution of tau protein concentration across the entire cortical structure, with the exception of the inner region, denoted by Ω_{int}, which is not involved in the pathological progression. In this inner zone, a diffusion-free formulation is adopted, and Dirichlet boundary conditions are imposed along the interface between Ω and Ω_{int} to ensure that no flux of tau protein occurs either into or out of Ω_{int}.

In addition to the reaction–diffusion system defined on $\Omega \backslash \Omega_{int}$, a pure diffusion equation was also implemented to represent the dynamics of tau protein along the white matter connections, corresponding to the structure of connectome. This domain is denoted by Ω_c, and it captures the network-like geometry of axonal fibre bundles that connect distant regions of the cerebral cortex. The inclusion of Ω_c enables the modelling of long-range protein transport, complementing the surface-based propagation described on $\Omega \setminus \Omega_{int}$.

$$\begin{cases} \dfrac{\partial u_{tau}}{\partial t} = D\nabla^2 u_{tau} + \alpha_{tau} u_{tau}(1 - u_{tau}) & \text{in } \Omega \setminus \Omega_{int} \\ \dfrac{\partial u_{tau}}{\partial t} = ND\nabla^2 u_{tau} & \text{in } \Omega_c \end{cases} \tag{5.1}$$

In system (5.1), the first expression models the reaction-diffusion behavior of the tau protein on the cortical surface $\Omega \setminus \Omega_{int}$. The diffusion coefficient D quantifies the rate at which the protein spreads across the brain surface and is set to $10 \left[\frac{mm^2}{year}\right]$, a reference value commonly associated with diffusion in grey matter, as adopted in previous studies [26]. The term α_{tau} denotes the reaction rate and represents the speed at which native tau proteins undergo misfolding and aggregation due to pathological processes. The second equation in the system describes a purely diffusive process on the connectome network, denoted by Ω_c. Here, the scalar multiplier N is introduced to account for the structural and functional anisotropy of white matter pathways that compose the connectome structure.

This parameter is set to 10^6, thus amplifying the diffusive flux in this region to reflect the high conductivity and long-range connectivity of neural fibre bundles.

5.2 Model 2: Dynamics of protein interactions

Alzheimer's disease is marked by the accumulation of two key proteins, β-amyloid and tau. β-amyloid appears first in frontal brain regions and initiates a cascade of pathological events, including tau misfolding and abnormal spread. Studies show that this protein promotes tau aggregation and accelerates its propagation, worsening brain atrophy and cognitive decline. Their interaction, together with network-based transmission, explains the distinct spatial patterns of these proteins during disease progression [18].

To simulate this interaction and to assess how the disease propagates across different brain regions, the model presented in equation (3.4) was implemented in COMSOL Multiphysics. The parameter k was set to 1, thereby maintaining the upper bound of misfolded protein concentration at a normalized value of 1, consistent with the assumption used in the system (5.1) for the tau protein alone.

The following mathematical model is formulated as a system of partial differential equations (PDEs) defined on the brain surface, denoted by Ω. In this framework, the internal domain Ω_{int} is excluded from the diffusion process, while in the connectome subdomain Ω_c, the dynamics are governed by the same diffusion-only equation previously adopted in the system (5.1).

$$\begin{cases} \dfrac{\partial u_{tau}}{\partial t} = D\nabla^2 u_{tau} + \alpha_{tau} u_{tau}(1-u_{tau}) + \gamma_{int} u_\beta u_{tau}(1-u_{tau}) & \text{in } \Omega \setminus \Omega_{int} \\ \dfrac{\partial u_\beta}{\partial t} = D\nabla^2 u_\beta + \alpha_\beta u_\beta(1-u_\beta) & \text{in } \Omega \setminus \Omega_{int} \\ \dfrac{\partial u_{tau}}{\partial t} = ND\nabla^2 u_{tau} & \text{in } \Omega_c \end{cases} \tag{5.2}$$

In the system (5.2), the first equation describes both the diffusion of the tau protein and its interaction with the β-amyloid protein, represented by the non-linear term $\gamma_{int} u_\beta u_{tau}(1-u_{tau})$, which models the acceleration of the amyloid-induced misfolding process of tau. The second equation accounts for the diffusion of the β-amyloid protein alone, with the parameter α_β denoting the conversion rate from healthy to misfolded protein, analogously to α_{tau} in the tau equation. The third equation models protein diffusion along the white matter fibre tracts, i.e. connectome channels. In all equations, the diffusion coefficient D is set to 10 $\left[\frac{mm^2}{year}\right]$ for both species, and the parameter N remains fixed at 10^6.

5.3 Model 3: Adapted model for patients

In order to adapt the interaction model defined in system (5.2) for application to patient-specific data, a modification was introduced to the parameter k, which governs the upper bound of misfolded protein concentration. Specifically, the value of k was modified from 1 to 3 to reflect clinical observations related to the accumulation of tau and β-amyloid proteins. This adjustment is based on experimental studies indicating that the standardized uptake

value (SUV) of tau, as measured via PET imaging, does not exceed a threshold of 3 in affected brain regions.

The SUV is a dimensionless parameter obtained by normalizing the tracer activity concentration in a specific tissue (in MBq/mL) to the injected dose normalized by body weight (in MBq/g). Assuming an average tissue density of 1 g/mL, the units cancel out, resulting in a unitless measure [16]. This normalization allows SUV to serve as a semi-quantitative indicator of pathological burden in vivo.

$$SUV = \frac{\text{Tracer concentration}(MBq/mL)}{\frac{\text{Injected dose}(MBq)}{\text{Body weight}(g)} 1(g/mL)}$$

To ensure reliability in model calibration, only patient data minimally affected by physiological variability or technical artifacts in SUV quantification were considered, thereby enhancing the model's ability to realistically simulate disease progression in clinical contexts. Within this framework, assigning $k = 3$ ensures that the modified model remains aligned with physiological constraints observed in vivo, thereby enhancing its capacity to realistically capture the dynamics of disease progression across individual patients.

The following system of equations represents the patient-specific adaptation of the interaction model previously introduced in (5.2), as implemented in COMSOL Multiphysics for the study of individual cases.

$$\begin{cases} \dfrac{\partial u_{tau}}{\partial t} = D\nabla^2 u_{tau} + \alpha_{tau} u_{tau}(3 - u_{tau}) + \gamma_{int} u_\beta u_{tau}(3 - u_{tau}) & \text{in } \Omega \setminus \Omega_{int} \\ \dfrac{\partial u_\beta}{\partial t} = D\nabla^2 u_\beta + \alpha_\beta u_\beta(3 - u_\beta) & \text{in } \Omega \setminus \Omega_{int} \\ \dfrac{\partial u_{tau}}{\partial t} = ND\nabla^2 u_{tau} & \text{in } \Omega_c \end{cases} \tag{5.3}$$

where parameter D is equal to $10\left[\frac{mm^2}{year}\right]$ and N is equal to 10^6.

Also in this case, the first equation represents both the diffusion of the tau protein and its interaction with the β-amyloid protein; the second is the reaction-diffusion equation of the β-amyloid protein exclusively; the third equation models diffusion through the channels of the connectome structure.

6. Simulation Results

Published data indicate that the accumulation process of misfolded proteins in Alzheimer's disease and the clinical progression of the medical condition develops over a period of about 40 years [26]. In the reality of the situation, the appearance of observable symptoms and the diagnosis do not coincide with $t = 0$, since significant protein aggregation has already occurred. Consequently, simulations were conducted along this ideal disease trajectory, from the initial seeding of tau in the entorhinal cortex through its progressive dissemination to all other brain regions. Simulation results were generated at six-month intervals: at each time point, the results were visualised in COMSOL Multiphysics, and the average tau protein concentrations for each area of the brain were saved in an Excel file in order to realize, using MATLAB calculation software, the diagrams shown in the following sections.

6.1 Model 1: tau protein diffusion

The simulation analysis is introduced by examining the results of the first model, developed specifically to study the diffusion dynamics of the tau protein exclusively. This model aims to represent an idealized scenario in which tau propagates throughout the brain independently, without any interaction with other misfolded proteins. This overview is in line with previous theories in the Alzheimer's disease literature, which posited that the pathogenesis was driven exclusively by the anomalous propagation of a single misfolded protein species. The concentration of the tau protein is regulated by the reaction-diffusion equation of the system (5.1), where the key parameters are the conversion rate α_{tau} and the diffusion coefficient D. As an initial condition, a concentration of zero was assigned across the entire brain domain, except for the entorhinal cortex — denoted by Ω_e and identified in the literature as the initial epicentre of Alzheimer's disease — where a non-zero initial concentration, denoted as $u_{0,tau}$, was introduced. This setup defines the two critical states of the system: the initial seeding at time zero, and the saturation point at concentration value 1, corresponding to the complete invasion of tau throughout the brain.

$$\begin{cases} \dfrac{\partial u_{tau}}{\partial t} = D\nabla^2 u_{tau} + \alpha_{tau} u_{tau}(1 - u_{tau}) & \text{in } \Omega \setminus \Omega_{int} \\ \dfrac{\partial u_{tau}}{\partial t} = ND\nabla^2 u_{tau} & \text{in } \Omega_c \\ u_{tau}(t = 0) = u_{0,tau} & \text{in } \Omega_e \\ u_{tau}(t = 0) = 0 & \text{in } \Omega \setminus \Omega_e \end{cases} \tag{6.1}$$

The system of equations presented in (6.1) corresponds to the reaction–diffusion model implemented in COMSOL Multiphysics for the simulation of tau protein propagation. The first two equations describe the evolution of the concentration in the cortical domain $\Omega \backslash \Omega_{int}$, and the connectome Ω_c, through reaction–diffusion and pure diffusion, respectively. The third equation specifies that the inner brain domain Ω_{int} is excluded from the diffusion process and remains unaffected by tau accumulation.

Initial conditions are imposed in the final two equations: a non-zero value $u_{0,tau}$ in the entorhinal cortex Ω_e and zero concentration elsewhere. While this simplified configuration may not fully capture clinical reality — where tau accumulation is already present in multiple regions at the time of diagnosis — it facilitates a clearer observation of the spatio-temporal dynamics of the disease.

To explore the model's behaviour, simulations were conducted by varying the initial concentration $u_{0,tau}$ and the conversion rate α_{tau}. The diffusion coefficient was held constant at $D = 10 \left[\frac{mm^2}{year}\right]$, following prior work [26]. In total, five simulations were performed, providing insight into how tau might spread through brain tissue in the absence of amyloid interaction. Despite its simplicity, the model serves as a foundational framework for understanding the fundamental mechanisms underlying tau-driven neurodegeneration.

6.2 The effect of α_{tau}

In this section, a parametric analysis is carried out on the α_{tau} coefficient to evaluate its influence on the propagation dynamics of misfolded tau protein. The initial condition assigns a concentration of 0.1 in the entorhinal zone, while all other cortical and connectome regions are initialized at zero.

The parameter α_{tau} is varied across the values 3, 3.5, 4, 4.5 e 5 $\left[\frac{1}{year}\right]$, and for each configuration, simulations are performed using COMSOL Multiphysics. To monitor the temporal evolution of disease progression, three-dimensional brain renderings are exported at five key time points: 96, 192, 288, 384 and 480 months, corresponding to 8, 16, 24, 32 and 40 years, respectively.

The external view in the figures below highlights the cortical surface, where the central, parietal, mid-frontal, upper-frontal, and temporal zones are allocated. Protein diffusion in this portion proceeds upwards from the temporal region, located inferiorly. Notably, small clusters of activity emerge in non-adjacent regions, particularly visible at 8 and 16 years. These patches, not spatially contiguous with the entorhinal zone, become active through long-range connections established through the connectome structure, demonstrating the model's ability to capture non-local propagation phenomena.

The inner view illustrates a sagittal section of the right hemisphere, where the inner region Ω_{int}, excluded from diffusion, appears centrally as an area unaffected by diffusion. Directly below, the entorhinal region Ω_e — the presumed origin of the pathological seeding — shows initial accumulation of misfolded protein and subsequent diffusion towards adjacent hippocampal structures and inferiorly into the temporal area. In a mirror-like manner, an identical propagation pattern is assumed for the left hemisphere of the brain.

A global perspective of the right hemisphere is also provided to demonstrate how diffusion progressively reaches peripheral cortical areas, including sensory and language-associated regions. This viewpoint allows visualisation of advanced diffusion to the upper

frontal regions and cingulate, which marks complete cortical involvement and clinical degeneration.

For each simulation, average tau concentrations per brain region are exported and post-processed using MATLAB to generate time-dependent concentration plots. The resulting profiles exhibit characteristic sigmoidal growth curves, all initiated from zero except in the entorhinal zone (set to 0.1), and asymptotically approaching the model's saturation threshold of 1, consistent with the critical concentration level.

The results of the simulations for each α_{tau} value — namely 3, 3.5, 4, 4.5 and 5 $\left[\frac{1}{year}\right]$ — are presented and analyzed in the following sections.

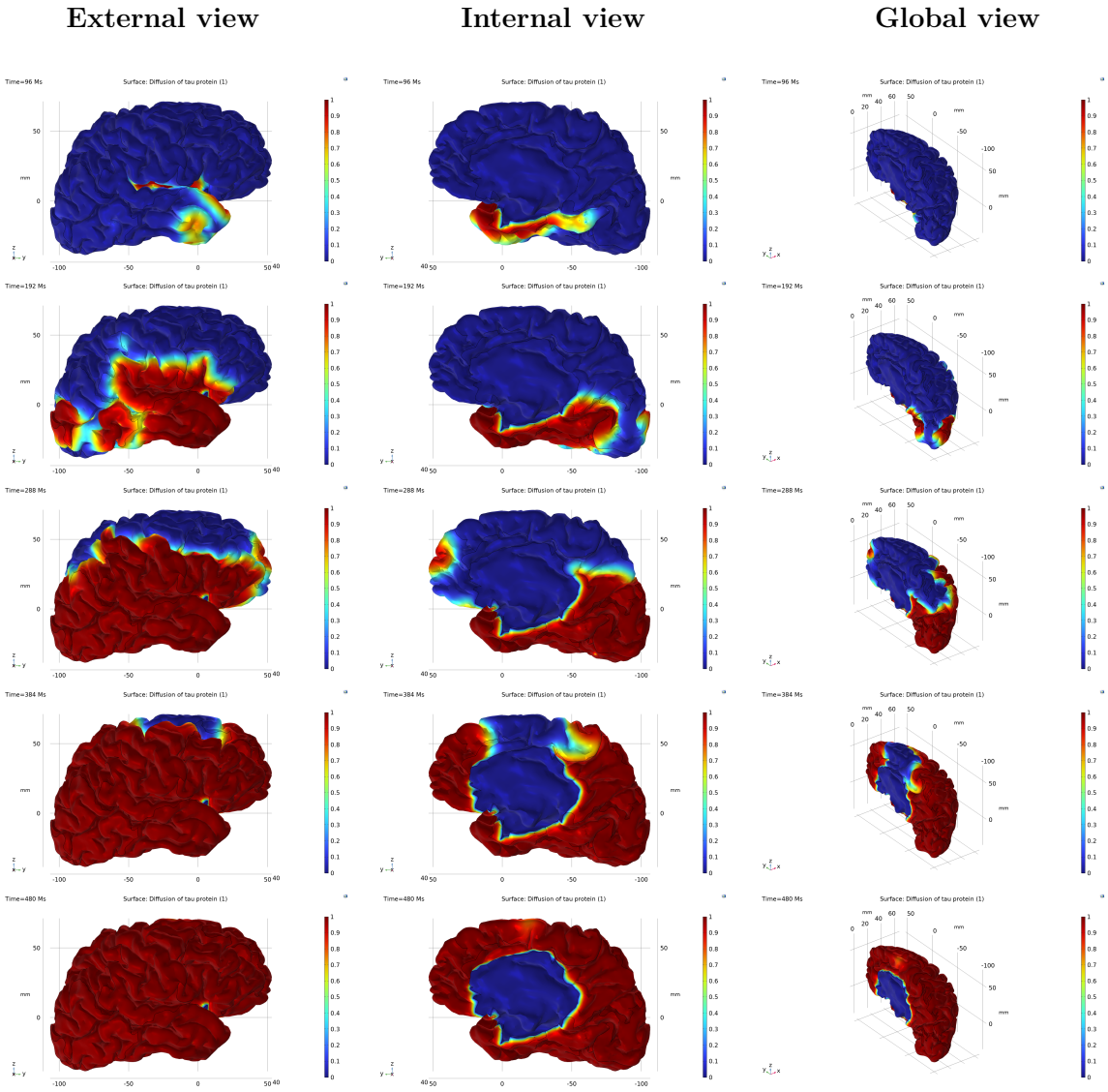

Figure 6.1: Evolution with $\alpha_{tau} = 3\left[\frac{1}{year}\right]$. From top to bottom row, year 8,16,24,32 and 40.

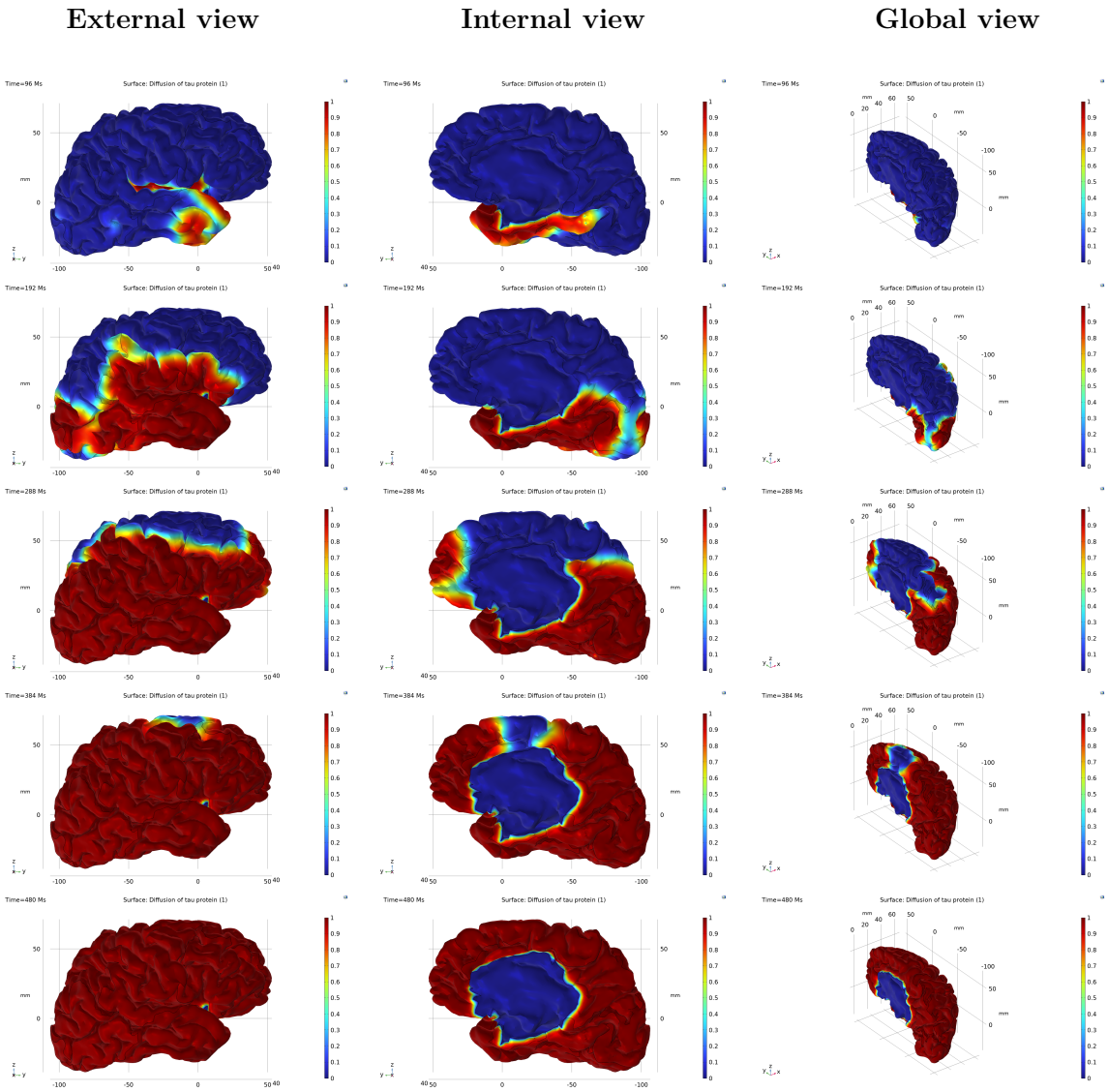

Figure 6.2: Evolution with $\alpha_{tau} = 3.5 \left[\frac{1}{year}\right]$. From top to bottom row, year 8,16,24,32 and 40.

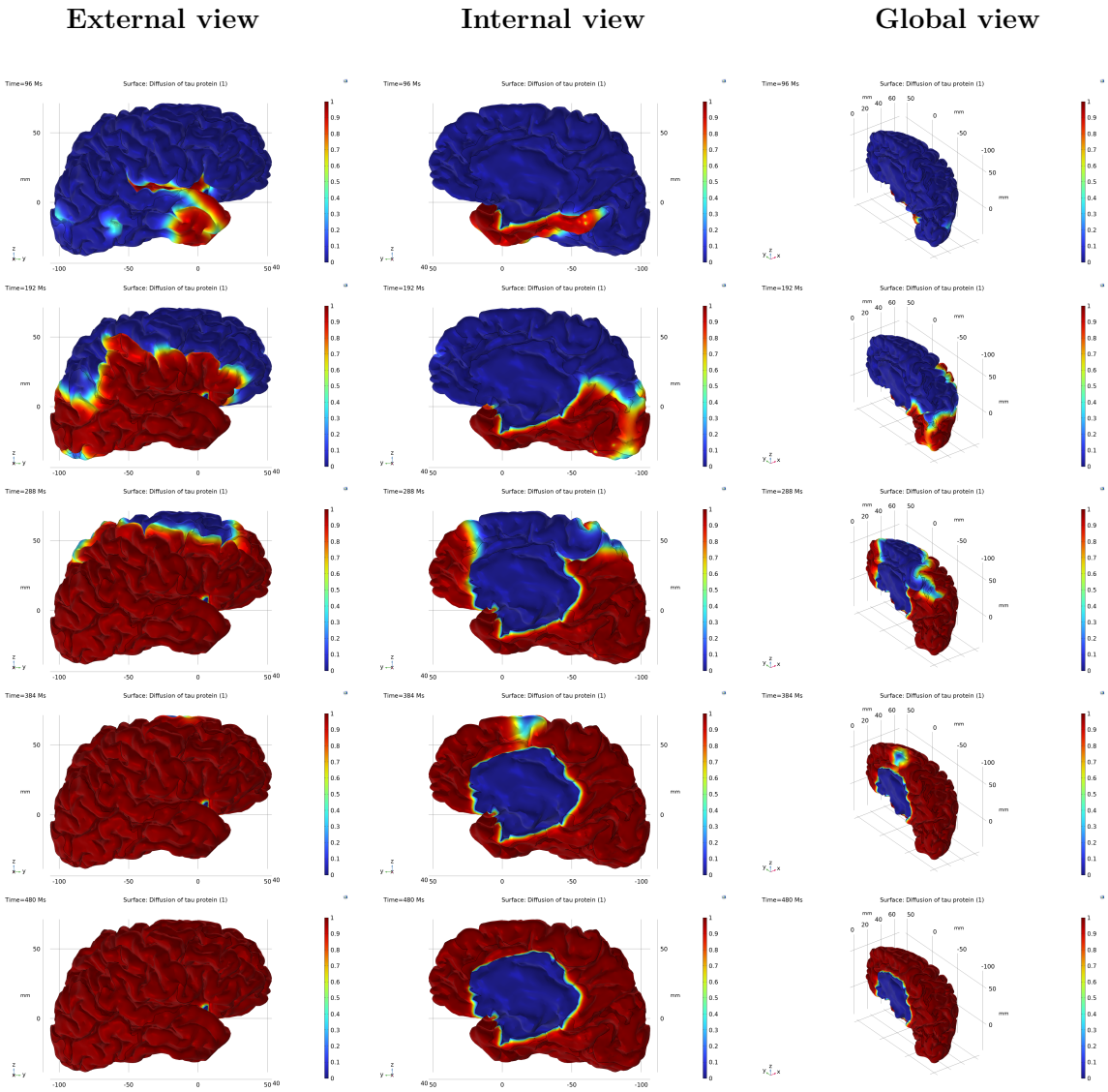

Figure 6.3: Evolution with $\alpha_{tau} = 4\left[\frac{1}{year}\right]$. From top to bottom row, year 8,16,24,32 and 40.

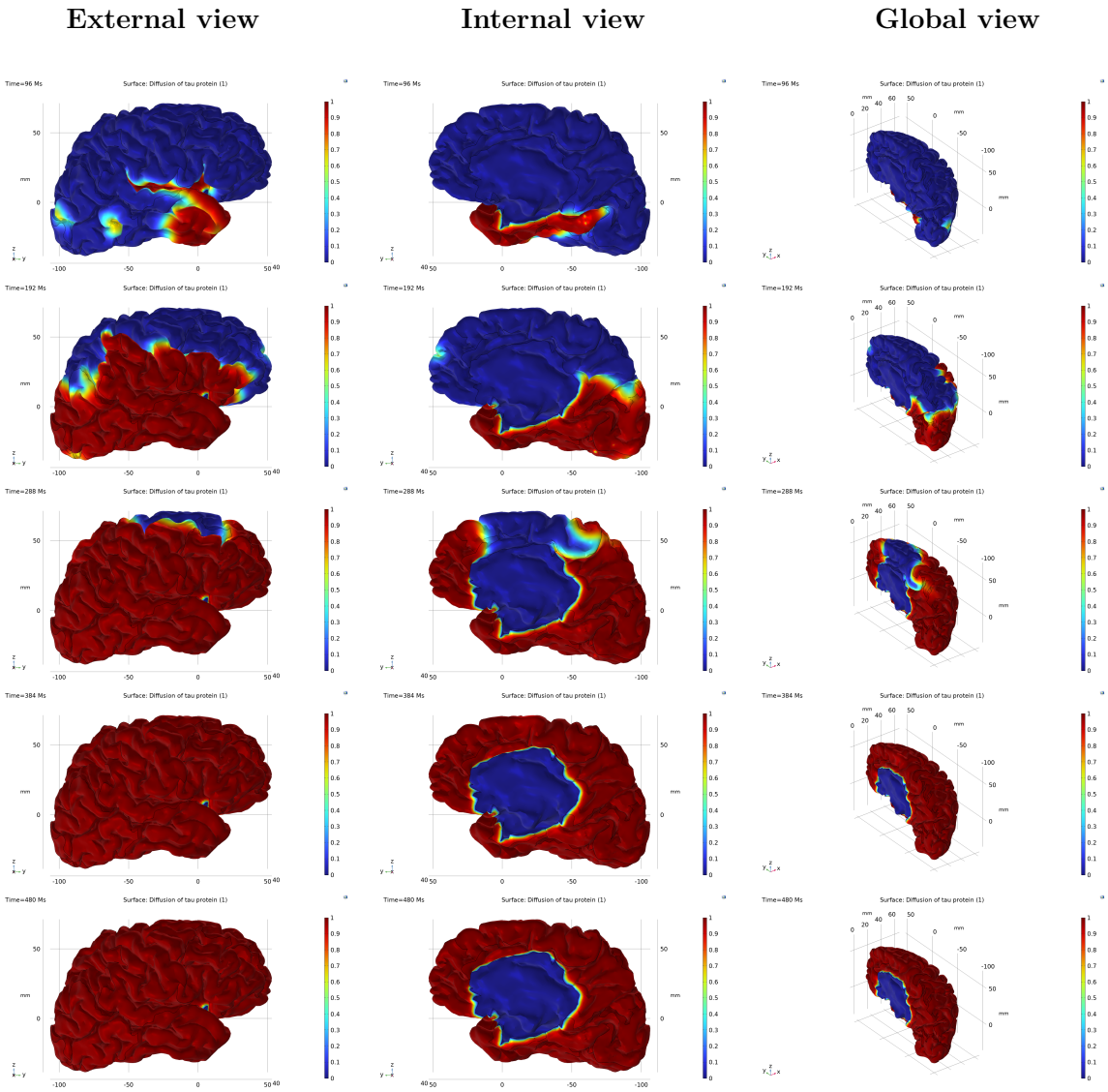

Figure 6.4: Evolution with $\alpha_{tau} = 4.5 \left[\frac{1}{year}\right]$. From top to bottom row, year 8,16,24,32 and 40.

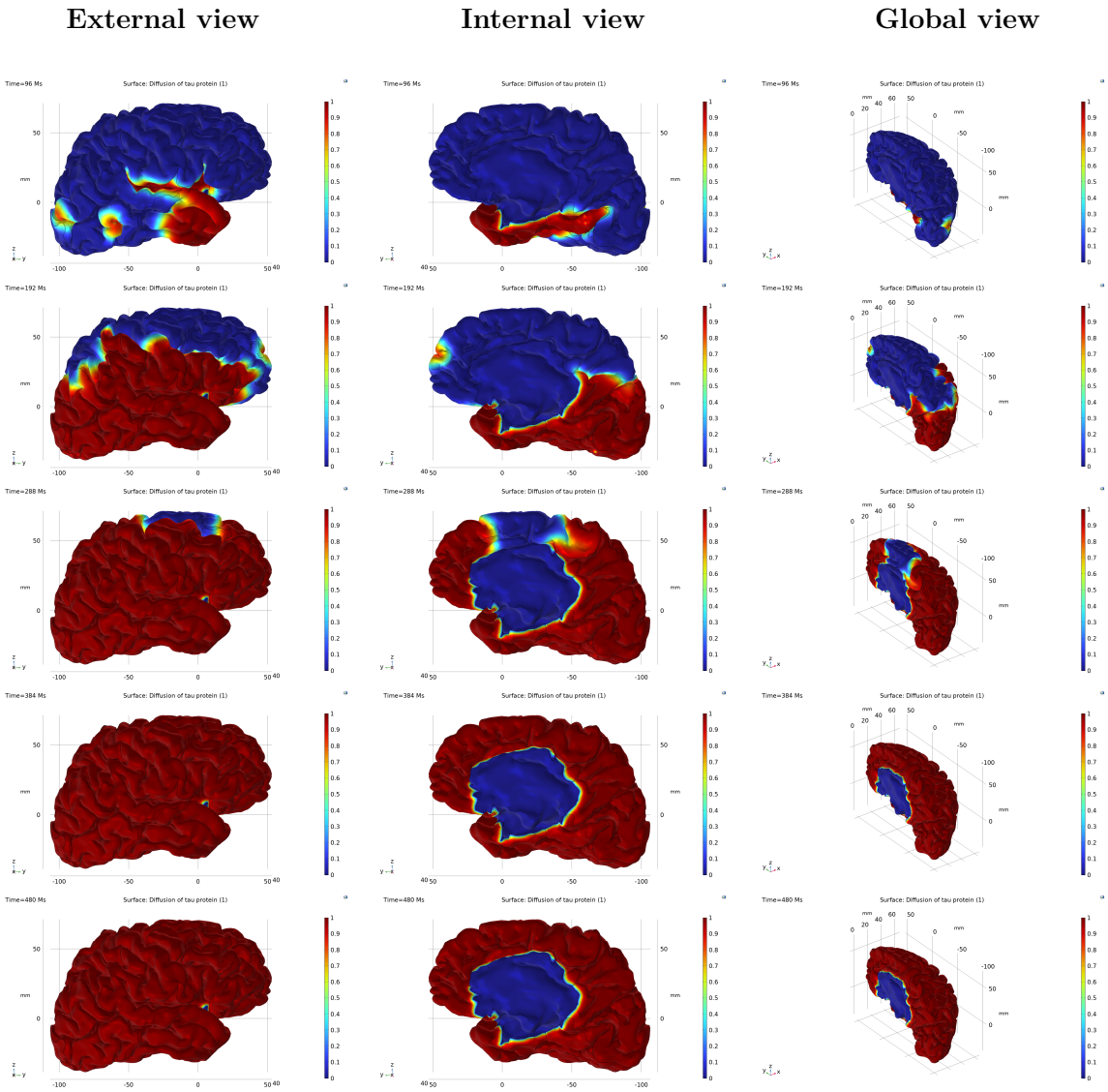

Figure 6.5: Evolution with $\alpha_{tau} = 5\left[\frac{1}{year}\right]$. From top to bottom row, year 8,16,24,32 and 40.

6.3 Parametric study results

Based on the results of the simulations, several observations can be made regarding the temporal dynamics of disease progression.

As illustrated in figure 6.1, when the conversion rate parameter is set to $\alpha_{tau} = 3 \left[\frac{1}{year}\right]$, the model predicts that the full cortical invasion by pathological tau culminates in the superior frontal region after approximately 40 years. This scenario represents an idealized, baseline progression of tau pathology, reflecting the disease spreading autonomously without interaction with other misfolded proteins or external pathological factors. Such a timescale is consistent with the slow and insidious nature of Alzheimer's disease progression observed clinically, emphasizing the long preclinical phase during which tau pathology gradually accumulates before overt symptoms manifest.

With incremental increases in the parameter α_{tau}, which governs the rate of tau misfolding and conversion, a marked acceleration in disease spread is observed. The simulations depicted in figures 6.2, 6.3, 6.4, and 6.5 demonstrate a systematic decrease in the total invasion time, varying from 40 years at $\alpha_{tau} = 3 \left[\frac{1}{year}\right]$ to approximately 30 years when α_{tau} achieves $5 \left[\frac{1}{year}\right]$. This trend highlights the critical influence of the conversion rate on the rhythm of neurodegeneration, suggesting that even relatively small increases in α_{tau} can significantly shorten the disease timeline, thereby potentially impacting clinical prognosis and intervention strategies.

The corresponding sigmoidal concentration profiles derived from the five simulations provide further qualitative insights into these dynamics. As α_{tau} increases, the curves become progressively steeper, indicating a more abrupt increase in tau concentration in the affected brain regions. This increase reflects a non-linear acceleration of protein accumulation and aggregation, which could correspond to a turning point beyond which pathological spread becomes rapid and widespread. On the abscissa axis, time is expressed in years to facilitate intuitive understanding of the time scale, while the y-axis shows the mean tau concentration progressively increasing between 0 and 1 and represents the transition from a healthy cortical state to a fully invaded one.

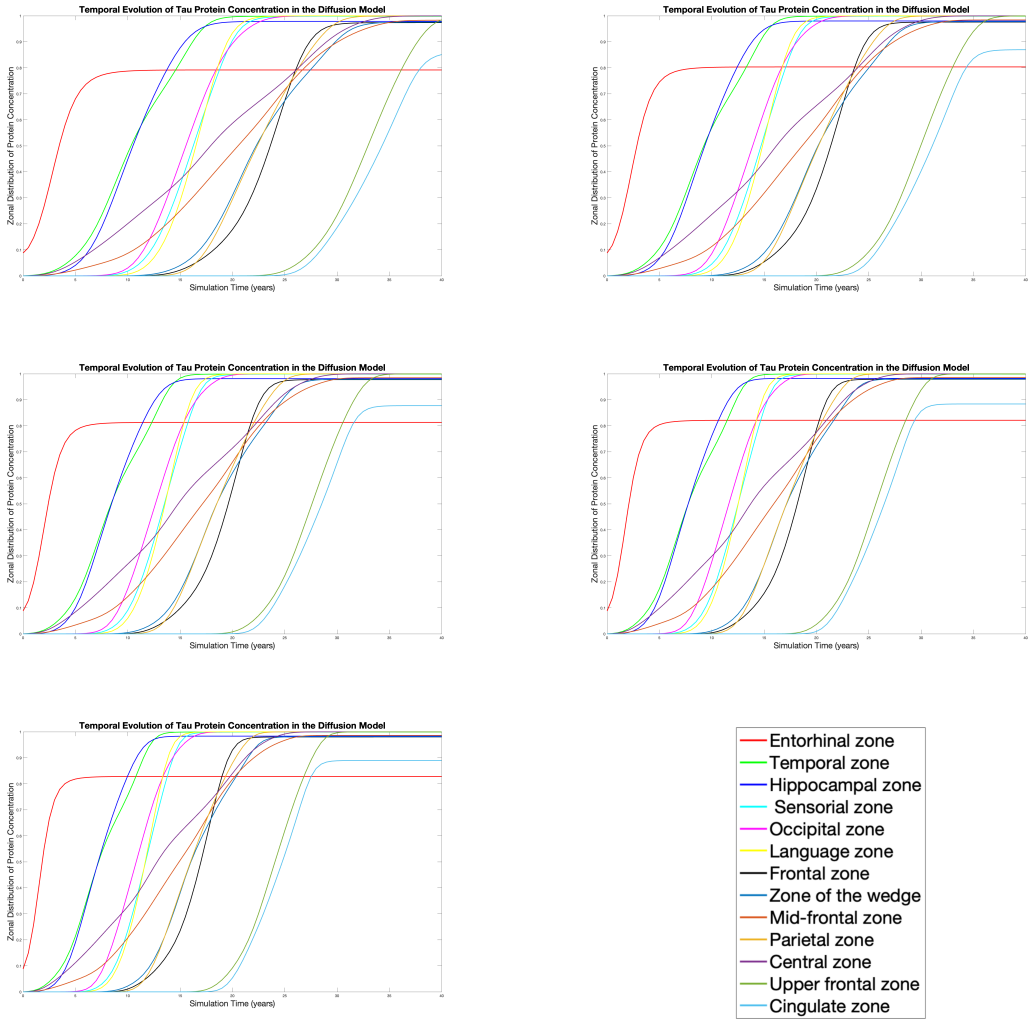

Figure 6.6: Average tau protein concentrations across brain regions in simulations with α_{tau} set to 3, 3.5, 4, 4.5, and 5 $\left[\frac{1}{year}\right]$, respectively.

Using MATLAB software, the evolution of the invasion times calculated by varying the parameter α_{tau} was analysed and plotted, as illustrated in figure 6.7. Additionally, table 6.1 reports the invasion times of the cerebral cortex obtained not only from the simulations presented above but also from additional simulations performed with intermediate values of the parameter α_{tau}, all ranging between 3 $\left[\frac{1}{year}\right]$ and 5 $\left[\frac{1}{year}\right]$.

α_{tau} $\left[\frac{1}{year}\right]$	**Invasion Time (years)**
3	40
3.25	38.5
3.5	37
3.75	36
4	34
4.25	33.5
4.5	32
4.75	31.5
5	30

Table 6.1: Summary of chosen α_{tau} values and the resulting times required for complete cerebral cortex invasion.

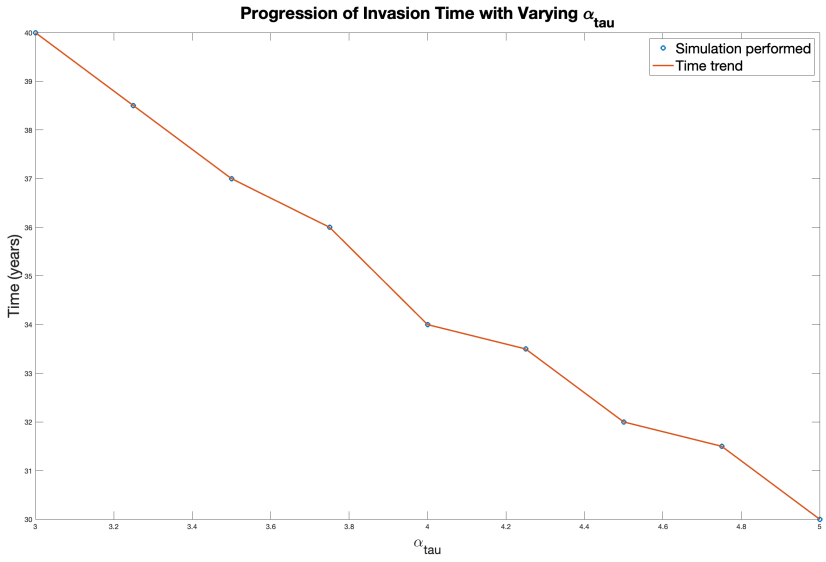

Figure 6.7: Trend of invasion time across different values of the parameter α_{tau}, highlighting the acceleration of disease progression with increasing misfolding rates.

6.4 Simulations with different parameters

6.4.1 First simulation: $\alpha_{tau} = 2.7$

In the first simulation, the parameters were set to $\alpha_{tau} = 2.7 \left[\frac{1}{\text{year}}\right]$ and $u_{0,tau} = 0.25$.

The diffusion of tau protein initiates in the entorhinal cortex and subsequently spreads to the temporal and hippocampal zones, which are among the first to be invaded. Propagation also occurs through the connectome structure, enabling rapid transfer to the central region. These areas, in turn, are connected to other cortical regions via the same network, facilitating both linear and quasi-instantaneous transmission of the pathology. As the diffusion advances, the language and sensorial areas are affected alongside the central, parietal, and occipital zones. The final regions to be involved are those located in the superior part of the brain, specifically the mid and upper frontal areas and the cingulate cortex.

Figure 6.8 shows the evolution of average tau protein concentrations across various brain regions. The full invasion of the cerebral cortex occurs in approximately 40 years, which is referred to as the saturation time. The resulting output consists of a series of sigmoid-like curves that align with patterns reported in the literature and reflect a plausible trajectory for tau propagation under idealized conditions.

In clinical cases of Alzheimer's disease, cortical invasion rarely unfolds over such a prolonged timescale. Instead, progression tends to occur more rapidly, leading to a range of neurological impairments. This acceleration is often due to the fact that diagnosis typically coincides with the onset of the first symptoms, by which time the corresponding brain regions have already undergone significant pathological changes. The complete invasion of the brain correlates with advanced stages of the disease, marked by severe cognitive and motor decline. Additionally, Alzheimer's pathology is associated with significant atrophy and loss of grey matter, which can ultimately compromise overall brain function.

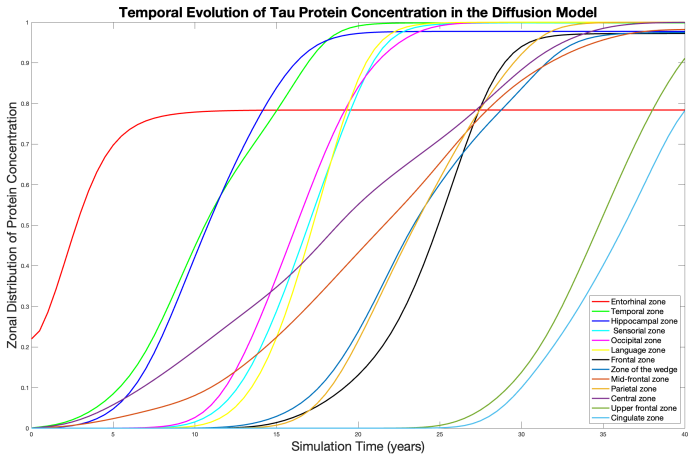

Figure 6.8: Simulation with parameters $\alpha_{tau} = 2.7 \left[\frac{1}{year}\right]$ and $u_{0,tau} = 0.25$. Average concentration trends of tau protein across different brain regions over a 40-year simulation period.

6.4.2 Second simulation: $\alpha_{tau} = 3$

In the second simulation, the parameters were set to $\alpha_{tau} = 3 \left[\frac{1}{\text{year}}\right]$ and $u_{0,tau} = 0.25$.

As in the previous case, the diffusion of tau protein begins in the entorhinal cortex and proceeds toward adjacent regions, both anatomically and via connectome-based connectivity.

From the trends shown in figure 6.9, the concentration curves rise earlier than those in the previous simulation, indicating an earlier onset of tau propagation. Although the final concentrations again approach saturation around 40 years, the advancement of the sigmoids suggests that cortical regions begin to be affected sooner than in the first simulation. This implies that the overall disease progression initiates earlier, potentially anticipating the emergence of clinical symptoms.

It is also observed that the invasion order of the brain regions remains unchanged: in fact, the upper-frontal and cingulate zones continue to be the last to reach saturation. This consistency suggests that the topological structure of the brain and the underlying connectome continue to drive the directional progression of the pathology, regardless of moderate changes in the misfolding rate parameter.

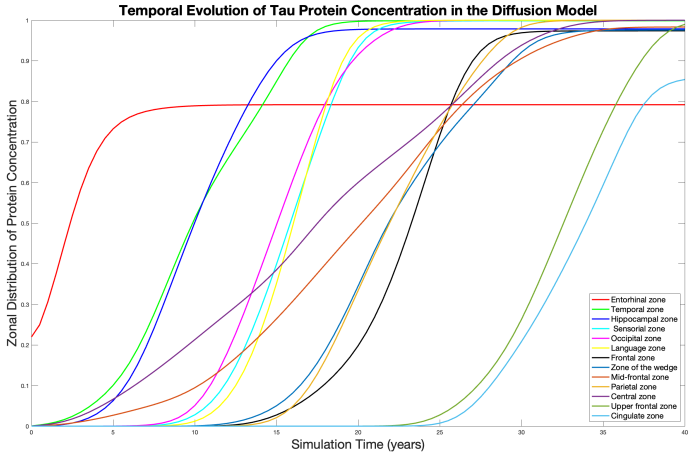

Figure 6.9: Simulation with parameters $\alpha_{tau} = 3 \left[\frac{1}{year}\right]$ and $u_{0,tau} = 0.25$. Average concentration trends of tau protein across different brain regions over a 40-year simulation period.

The following simulations highlight that the parameter α_{tau} plays a central role in this type of analysis, while the initial concentration $u_{0,tau}$ has a comparatively minor impact. Although both parameters are inherently patient-specific, the initial concentration is assumed to correspond to the early seeding level of the misfolded protein, a quantity that is rarely measurable in clinical settings. This is primarily due to the fact that, by the time Alzheimer's disease is typically diagnosed, the entorhinal cortex and adjacent regions are already partially invaded by the pathological agents, thereby reducing the relevance of precise knowledge of the initial condition.

6.4.3 Third simulation: $\alpha_{tau} = 3.7$

In the third simulation, the coefficient α_{tau} was increased to $3.7 \left[\frac{1}{\text{year}}\right]$, while the initial concentration $u_{0,tau}$ was slightly reduced to 0.2.

Compared to the first two simulations, the sigmoidal curves representing the regional concentrations emerge at an earlier time, despite the lower initial seeding level. This trend is illustrated in figure 6.10. The overall cortical invasion is completed in approximately 36 years, indicating a faster progression of the pathology relative to the previous cases.

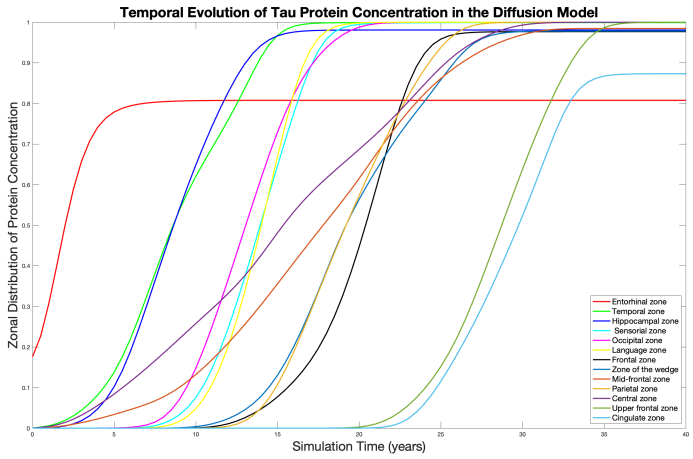

Figure 6.10: Simulation with parameters $\alpha_{tau} = 3.7 \left[\frac{1}{year}\right]$ and $u_{0,tau} = 0.2$. Average concentration trends of tau protein across different brain regions over a 40-year simulation period.

This result suggests that the conversion rate α_{tau} plays a more significant role than the initial concentration $u_{0,tau}$ in determining the speed of pathological spread. Even with a lower initial amount of tau protein, the increased rate of self-replication and misfolding leads to an earlier and more rapid invasion of brain regions. This highlights the importance of the kinetic properties of tau propagation in shaping the temporal profile of disease progression.

6.4.4 Fourth and fifth simulation: $\alpha_{tau} = 4$ and $\alpha_{tau} = 4.3$

The final two simulations further demonstrate how increasing the parameter α_{tau} leads to a progressive reduction in the time required for complete cortical invasion.

In the fourth simulation, shown in figure 6.11, α_{tau} is set to $4 \left[\frac{1}{\text{year}}\right]$, with an initial concentration $u_{0,tau} = 0.15$. In the fifth simulation, displayed in figure 6.12, the parameters are $\alpha_{tau} = 4.3 \left[\frac{1}{\text{year}}\right]$ and $u_{0,tau} = 0.1$.

The fourth and fifth simulations confirm the trend observed in previous analyses: increasing the parameter α_{tau} results in a faster invasion of the cerebral cortex, with total saturation occurring after approximately 34 and 33 years, respectively. Despite progressively lower initial concentrations, the outcome remains largely unchanged, reinforcing the

conclusion that the conversion rate α_{tau} is the primary driver of disease propagation, while the initial seeding level $u_{0,tau}$ has limited influence.

The expected and consistent graphical output across all cases remains a family of sigmoidal curves, each representing the temporal evolution of tau concentration within a specific brain region, thereby providing a clear and interpretable depiction of the progression dynamics.

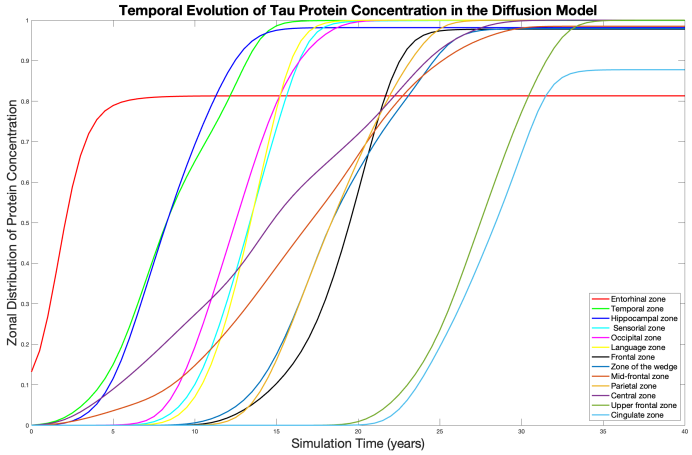

Figure 6.11: Simulation with parameters $\alpha_{tau} = 4\left[\frac{1}{year}\right]$ and $u_{0,tau} = 0.15$. Average concentration trends of tau protein across different brain regions over a 40-year simulation period.

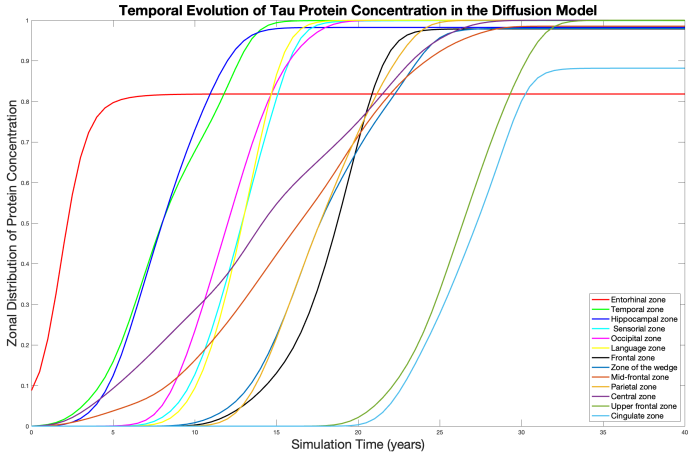

Figure 6.12: Simulation with parameters $\alpha_{tau} = 4.3\left[\frac{1}{year}\right]$ and $u_{0,tau} = 0.1$. Average concentration trends of tau protein across different brain regions over a 40-year simulation period.

6.5 Model 2: interaction between tau and Aβ proteins

In this section, the results of the simulations examining the interaction between tau and β-amyloid proteins within the brain are presented. The objective is to highlight how the progression of cerebral invasion differs from the case in which α_{tau} was the only active parameter.

The concentration dynamics of the tau and β-amyloid proteins are governed by the coupled reaction–diffusion equations defined in system (5.2). In this model, the key parameters are the conversion rates α_{tau} and α_β, the diffusion coefficient D, and the interaction coefficient γ_{int}, which quantifies the extent to which β-amyloid influences tau propagation.

As initial conditions, a non-zero concentration of the tau protein $u_{0,tau}$ was assigned exclusively to the entorhinal cortex, denoted by Ω_e and considered in the literature as the primary site of tau pathology, while a non-zero concentration of β-amyloid $u_{0,\beta}$ was set in the frontal region, denoted by Ω_f, which is known to exhibit early amyloid deposition.

All other brain regions were initialized with zero concentration for both proteins. As in the Model 1, a concentration value of 1 represents the saturation threshold, corresponding to complete pathological invasion of the brain tissue.

$$\begin{cases} \dfrac{\partial u_{tau}}{\partial t} = D\nabla^2 u_{tau} + \alpha_{tau} u_{tau}(1-u_{tau}) + \gamma_{int} u_\beta u_{tau}(1-u_{tau})\mathbb{H}(t-16) & \text{in } \Omega \setminus \Omega_{int} \\ \dfrac{\partial u_\beta}{\partial t} = D\nabla^2 u_\beta + \alpha_\beta u_\beta(1-u_\beta) & \text{in } \Omega \setminus \Omega_{int} \\ \dfrac{\partial u_{tau}}{\partial t} = ND\nabla^2 u_{tau} & \text{in } \Omega_c \\ u_{tau}(t=0) = u_{0,tau} & \text{in } \Omega_e \\ u_{tau}(t=0) = 0 & \text{in } \Omega \setminus \Omega_e \\ u_\beta(t=0) = u_{0,\beta} & \text{in } \Omega_f \\ u_\beta(t=0) = 0 & \text{in } \Omega \setminus \Omega_f \end{cases} \tag{6.2}$$

System (6.2) was implemented in COMSOL Multiphysics to enable a detailed visualization and analysis of the interaction dynamics between tau and β-amyloid proteins.

In the simulations conducted, it was assumed that the onset of the interaction occurs approximately 16 years after the onset of the disease, corresponding to the time when the diffusion front of the tau protein reaches the frontal region of the brain. This timing was established on the basis of the previous parametric study focusing exclusively on tau propagation. Accordingly, the interaction term $\gamma_{int} u_\beta u_{tau}(1-u_{tau})\mathbb{H}(t-16)$ within the model equations is activated at time $t = 200$. Furthermore, according to the scientific literature, the protein-protein interaction is understood to commence after a variable latent period, predominantly influenced by disease progression, subsequent to the initial seeding and early invasion of tau protein within the brain [18].

For each value of $\alpha_{tau} = 3{,}4{,}5 \left[\frac{1}{year}\right]$, simulations were conducted by progressively varying the parameter α_β among 2,3,4,5 $\left[\frac{1}{year}\right]$ and γ_{int} among 1.5,2.5,3 $\left[\frac{1}{year}\right]$. The resulting invasion times are reported in tables 6.2 and 6.3 below.

$\alpha_{tau}\left[\frac{1}{year}\right]$	$\alpha_{\beta}\left[\frac{1}{year}\right]$	$\gamma_{int}\left[\frac{1}{year}\right]$	**Invasion Time (years)**
3	2	1.5	37.5
4	2	1.5	32
5	2	1.5	28
3	3	1.5	35.5
4	3	1.5	31
5	3	1.5	28
3	4	1.5	35
4	4	1.5	31
5	4	1.5	28
3	5	1.5	35
4	5	1.5	31
5	5	1.5	27.5
3	2	2	35
4	2	2	31
5	2	2	28
3	3	2	34.5
4	3	2	30.5
5	3	2	27.5
3	4	2	34
4	4	2	30
5	4	2	27
3	5	2	33.5
4	5	2	30
5	5	2	27
3	2	2.5	35
4	2	2.5	31
5	2	2.5	28
3	3	2.5	33.5
4	3	2.5	30
5	3	2.5	27
3	4	2.5	33
4	4	2.5	29.5
5	4	2.5	27
3	5	2.5	32.5
4	5	2.5	29
5	5	2.5	27

Table 6.2: Respectively, from left to right, the coefficients of α_{tau}, α_{β}, γ_{int} and the invasion times resulting from the simulations performed.

$\alpha_{tau}\left[\frac{1}{year}\right]$	$\alpha_{\beta}\left[\frac{1}{year}\right]$	$\gamma_{int}\left[\frac{1}{year}\right]$	**Invasion Time (years)**
3	2	3	34
4	2	3	31
5	2	3	28
3	3	3	32.5
4	3	3	29.5
5	3	3	26.5
3	4	3	32
4	4	3	28.5
5	4	3	26
3	5	3	31.5
4	5	3	28
5	5	3	25.5

Table 6.3: Respectively, from left to right, the coefficients of α_{tau}, α_{β}, γ_{int} and the invasion times resulting from the simulations performed.

The simulation results yield several key insights. First, it is clear that, with both α_{tau} and α_{β} held constant, increasing the interaction parameter γ_{int} consistently reduces the invasion time of the cerebral cortex. This outcome aligns with existing literature, which suggests that the propagation of β-amyloid protein accelerates disease progression and consequently cognitive decline.

In contrast, the influence of α_{β} appears comparatively modest. When α_{tau} remains fixed, variations in α_{β} lead to only gradual, incremental decreases in invasion time, without any marked or abrupt effects.

Taken together, these findings suggest that among the parameters α_{β} and γ_{int}, the interaction coefficient plays the more decisive role in modulating the dynamics of disease progression. Accordingly, the reaction–diffusion process driving the spread of proteins associated with Alzheimer's disease is primarily influenced by their mutual interaction, as well as by the timing of β-amyloid diffusion initiation from the frontal brain region.

In figure 6.13 this trend is shown: on each line the parameter γ_{int} is kept constant and the parameter α_{β} is varied for each plot. Looking at the graphs from left to right, it can be seen how the invasion times vary for the values of $\alpha_{tau} = 3{,}4{,}5\left[\frac{1}{year}\right]$ shown on the x-axis.

Several simulations are presented to illustrate that, according to the results in tables 6.2 and 6.3, when α_{tau} and α_{β} are fixed, increasing the parameter γ_{int} leads to a decrease in the time required for the invasion of the cerebral cortex. The parameters $\alpha_{tau} = 5\left[\frac{1}{year}\right]$ and $\alpha_{\beta} = 3\left[\frac{1}{year}\right]$ are first considered, with $\alpha_{tau} > \alpha_{\beta}$. Four time points are recorded for each simulation: 7, 14, 21, and 28 years (i.e., 84, 168, 252, and 336 months). At each time point, the progression of diffusion is reported as the parameter γ_{int} increases. Next, the case where $\alpha_{tau} < \alpha_{\beta}$ is considered, with $\alpha_{tau} = 4\left[\frac{1}{year}\right]$ and $\alpha_{\beta} = 5\left[\frac{1}{year}\right]$. The trend of cerebral cortex invasion is shown for values of $\gamma_{int} = 1.5, 2, 2.5, 3\left[\frac{1}{year}\right]$ at the time points of 8, 16, 24, and 32 years (i.e., 96, 192, 288, and 384 months). Finally, the case where $\alpha_{tau} = \alpha_{\beta}$ is considered, with both parameters equal to $3\left[\frac{1}{year}\right]$. The process of cerebral

cortex invasion is presented for each value of γ_{int} at the four time points of 9, 18, 27, and 36 years, corresponding to 108, 216, 324, and 432 months, respectively.

All simulations were performed with an initial concentration of tau protein in the entorhinal zone equal to 0.1 and of β-amyloid protein equal to 0.1 in the frontal zone. For each simulation performed, the graph of the average protein concentrations accumulated in each area of the brain is shown, in order to have a complete view of how, as the parameter γ_{int} increases in all three cases studied, the invasion time gradually decreases.

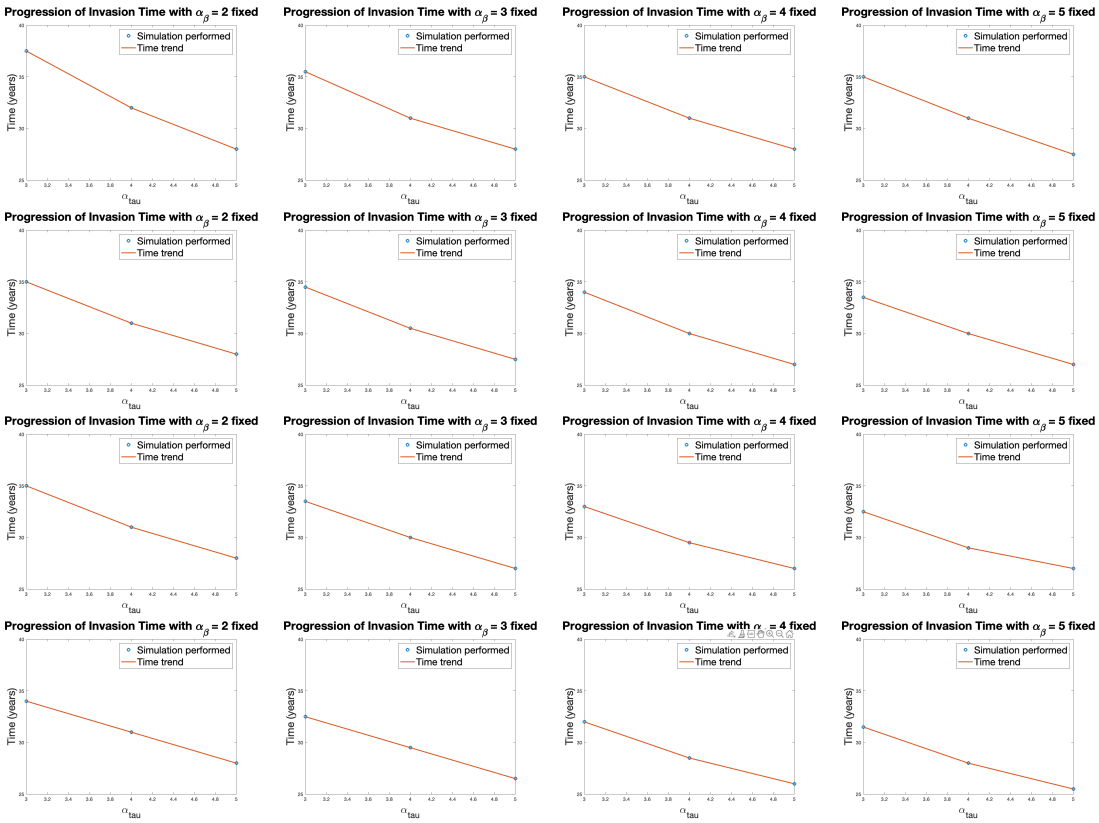

Figure 6.13: Trend of invasion times for varying values of γ_{int} and α_β. From top to bottom, γ_{int} assumes the values 1.5,2,2.5, and 3 $\left[\frac{1}{year}\right]$; within each row, from left to right, α_β = 2,3,4,5 $\left[\frac{1}{year}\right]$.

6.5.1 Case $\alpha_{tau} > \alpha_{\beta}$

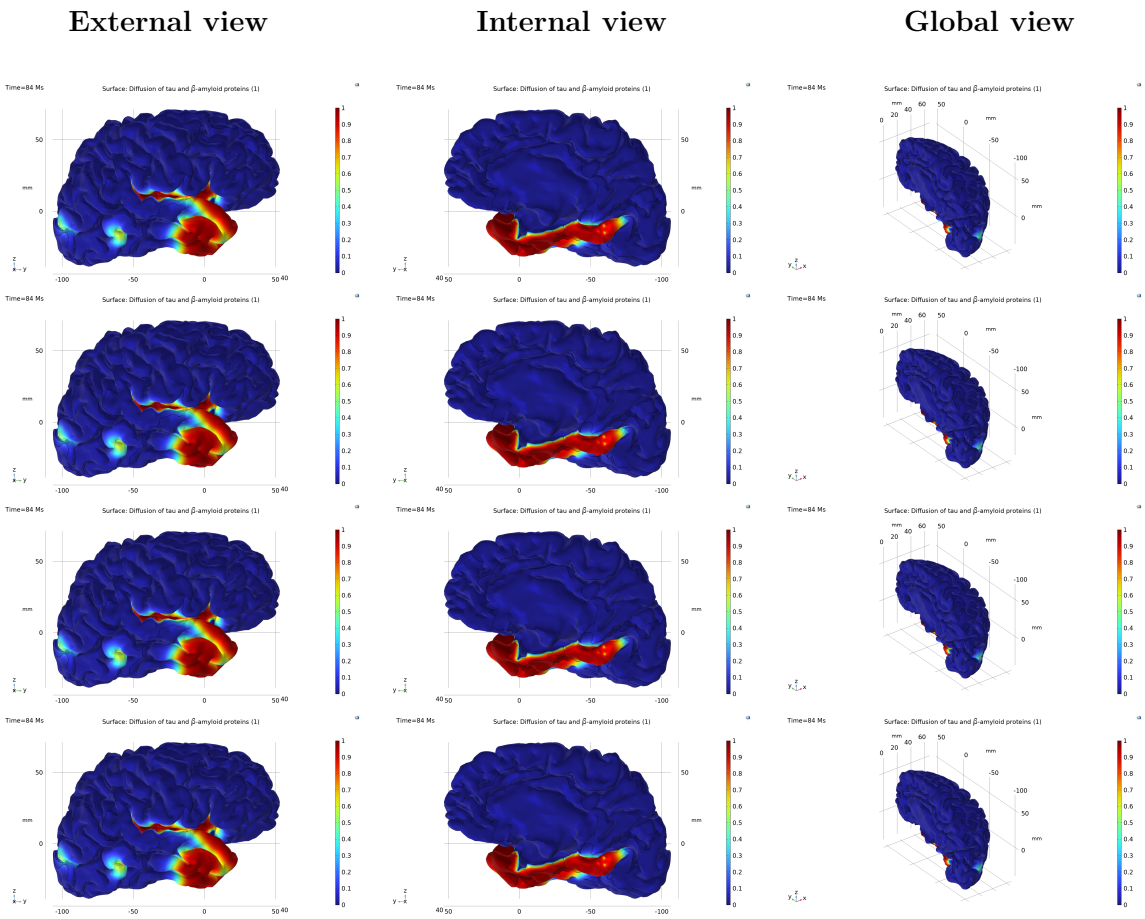

Figure 6.14: Year of evolution 7 with $\alpha_{tau} = 5\left[\frac{1}{year}\right]$, $\alpha_{\beta} = 3\left[\frac{1}{year}\right]$ fixed. From top to bottom, $\gamma_{int} = 1.5$,2,2.5 and 3 $\left[\frac{1}{year}\right]$.

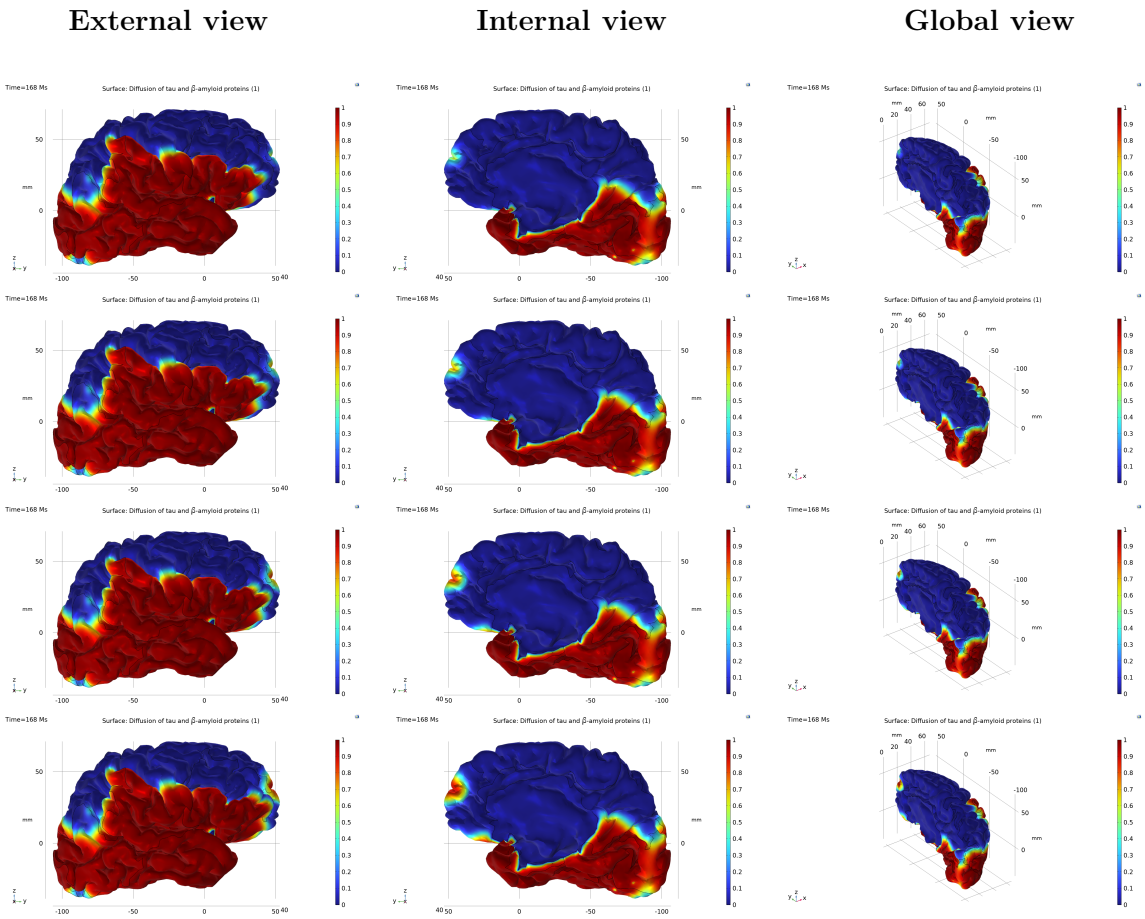

Figure 6.15: Year of evolution 14 with $\alpha_{tau} = 5\left[\frac{1}{year}\right]$, $\alpha_{\beta} = 3\left[\frac{1}{year}\right]$ fixed. From top to bottom, $\gamma_{int} = 1.5$,2,2.5 and 3 $\left[\frac{1}{year}\right]$.

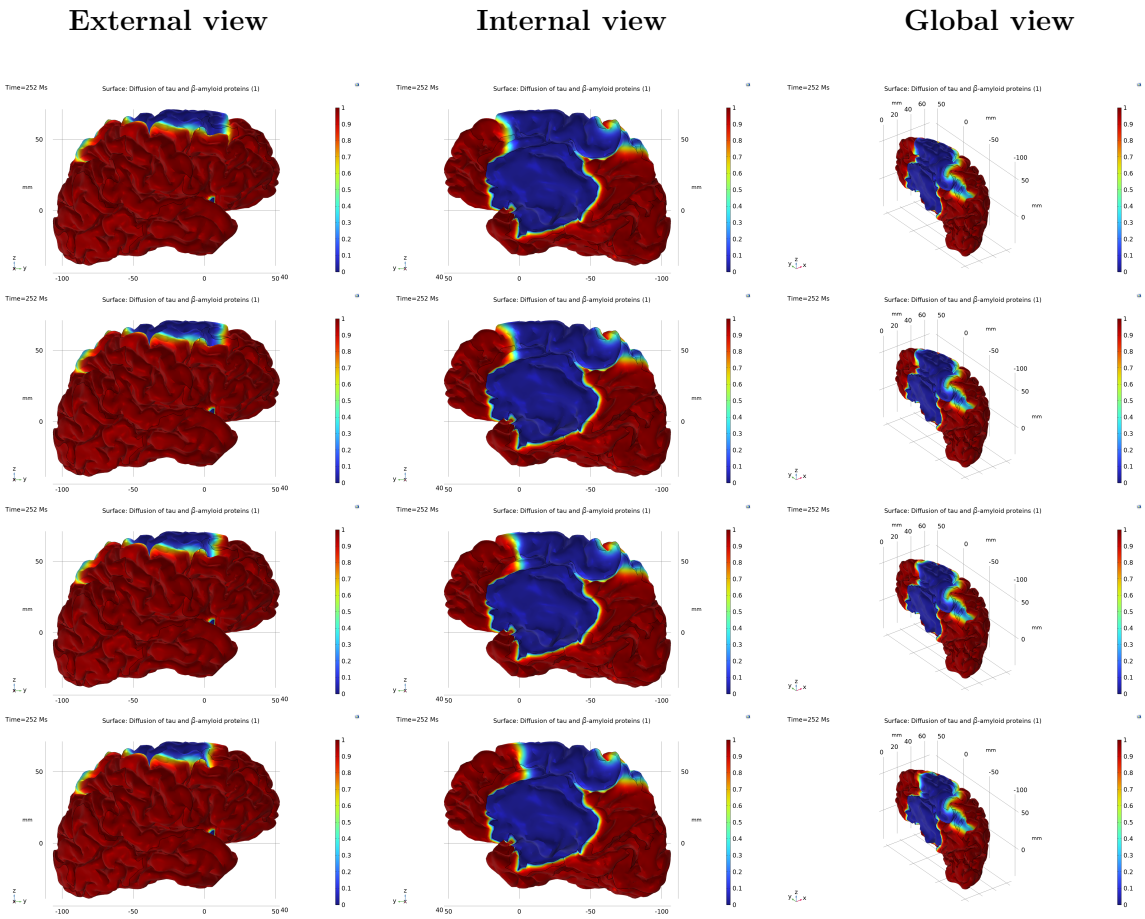

Figure 6.16: Year of evolution 21 with $\alpha_{tau} = 5\left[\frac{1}{year}\right]$, $\alpha_{\beta} = 3\left[\frac{1}{year}\right]$ fixed. From top to bottom, $\gamma_{int} = 1.5$,2,2.5 and 3 $\left[\frac{1}{year}\right]$.

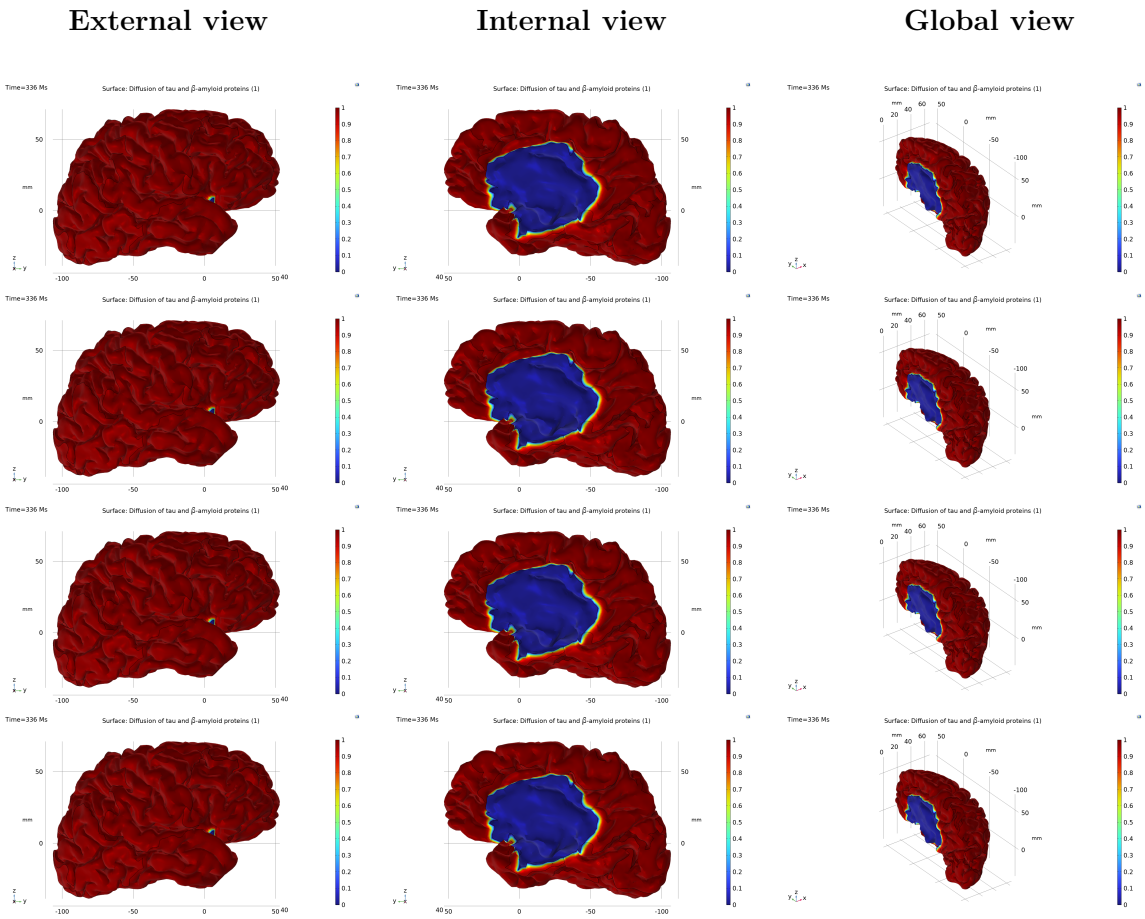

Figure 6.17: Year of evolution 28 with $\alpha_{tau} = 5\left[\frac{1}{year}\right]$, $\alpha_{\beta} = 3\left[\frac{1}{year}\right]$ fixed. From top to bottom, $\gamma_{int} = 1.5$,2,2.5 and 3 $\left[\frac{1}{year}\right]$.

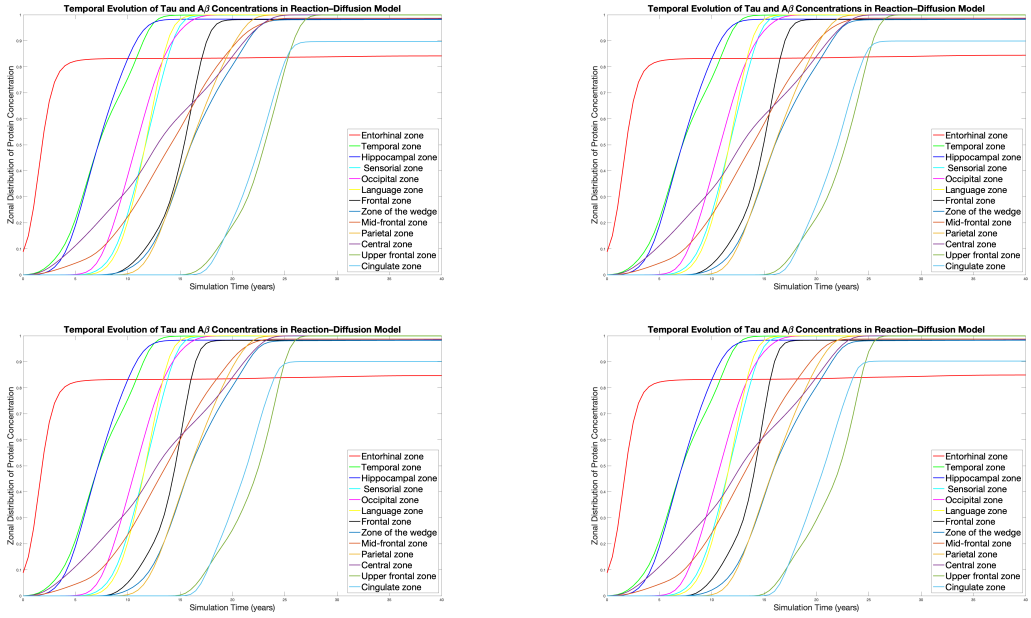

Figure 6.18: Trend of mean concentrations for each brain region resulting from simulations with $\alpha_{tau} = 5\left[\frac{1}{year}\right]$ and $\alpha_{\beta} = 3\left[\frac{1}{year}\right]$, for increasing values of the interaction parameter $\gamma_{int} = 1.5{,}2{,}2.5{,}3\ \left[\frac{1}{year}\right]$, respectively.

6.5.2 Case $\alpha_{tau} < \alpha_{\beta}$

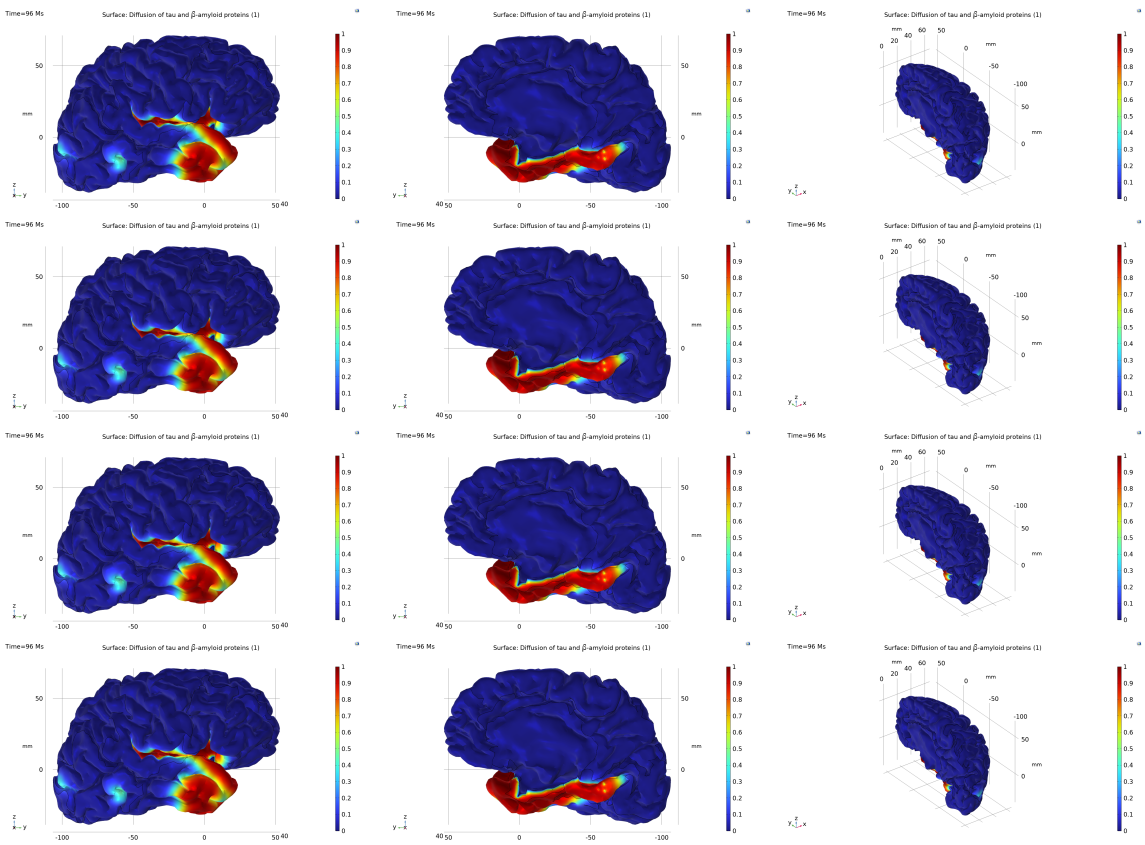

Figure 6.19: Year of evolution 8 with $\alpha_{tau} = 4\left[\frac{1}{year}\right]$, $\alpha_{\beta} = 5\left[\frac{1}{year}\right]$ fixed. From top to bottom, $\gamma_{int} = 1.5$,2,2.5 and 3 $\left[\frac{1}{year}\right]$.

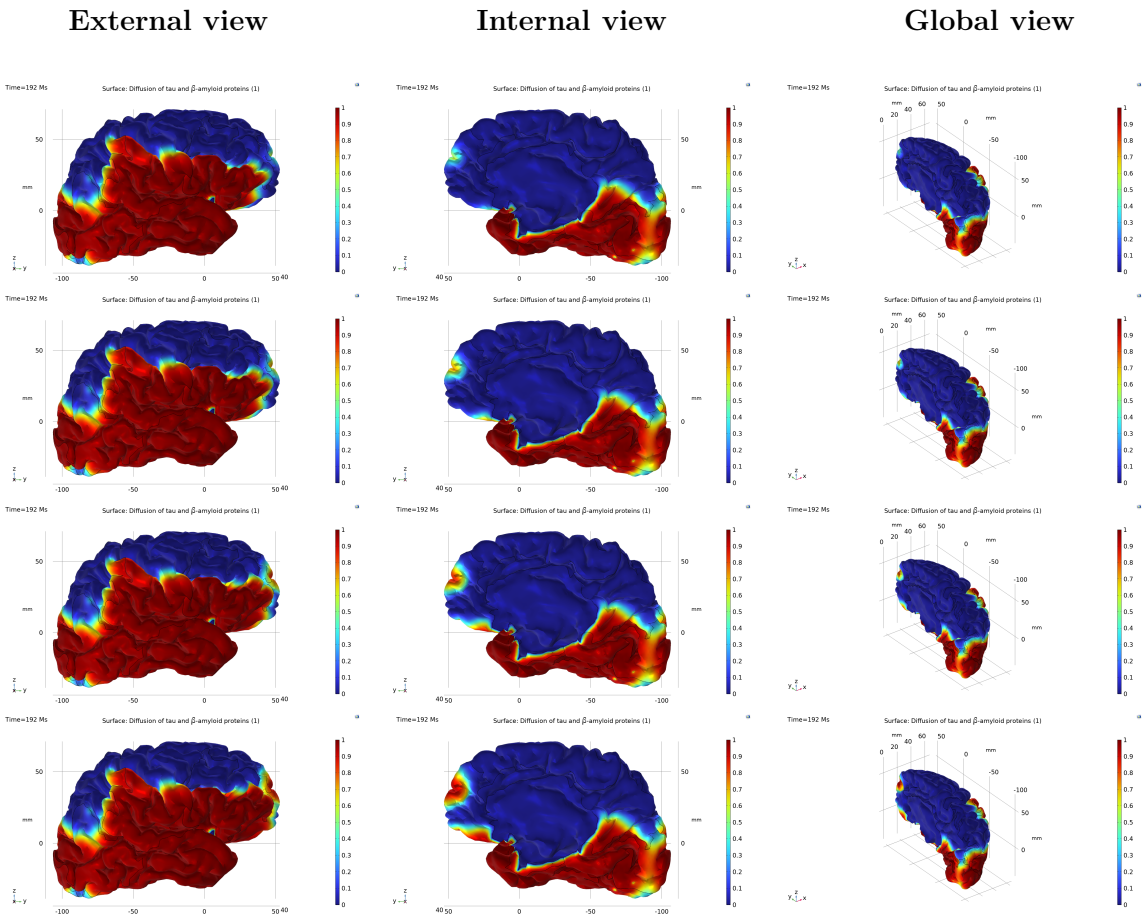

Figure 6.20: Year of evolution 16 with $\alpha_{tau} = 4\left[\frac{1}{year}\right]$, $\alpha_{\beta} = 5\left[\frac{1}{year}\right]$ fixed. From top to bottom, $\gamma_{int} = 1.5$,2,2.5 and 3 $\left[\frac{1}{year}\right]$.

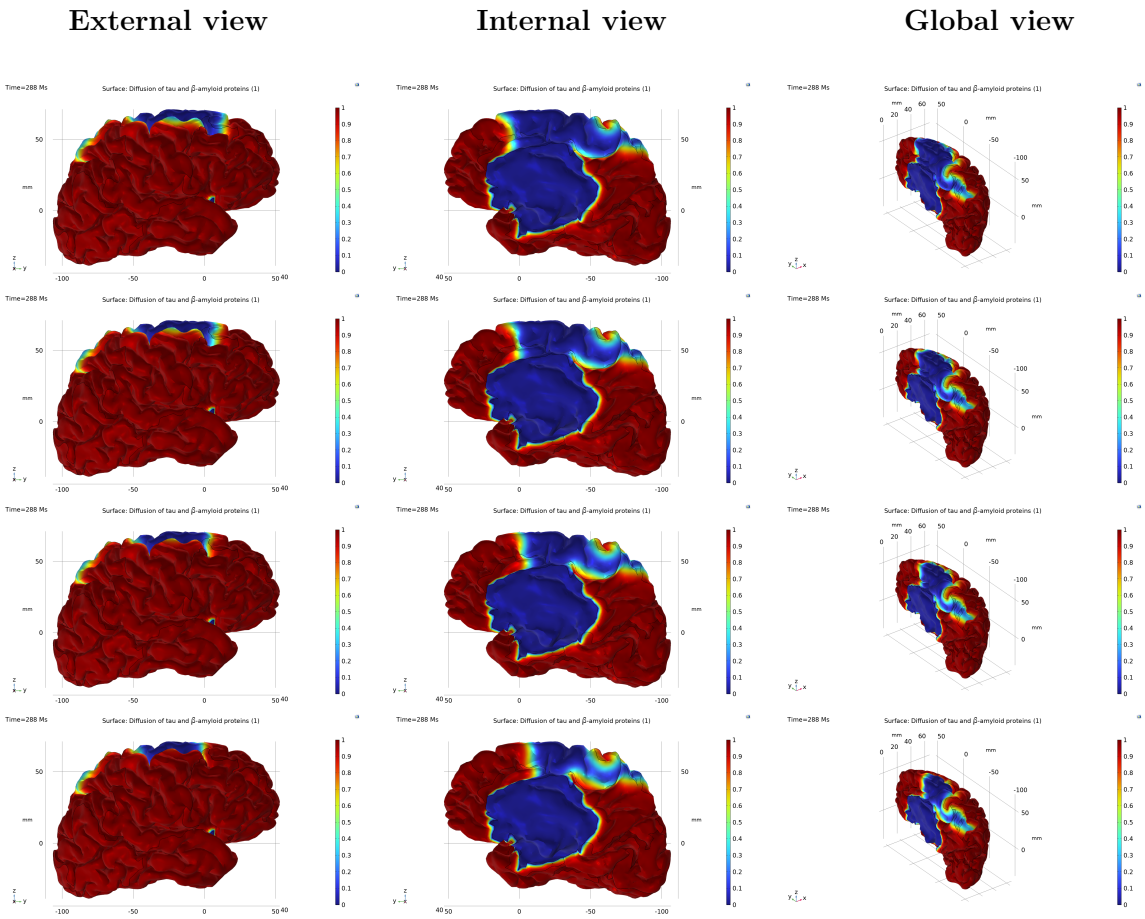

Figure 6.21: Year of evolution 24 with $\alpha_{tau} = 4\left[\frac{1}{year}\right]$, $\alpha_{\beta} = 5\left[\frac{1}{year}\right]$ fixed. From top to bottom, $\gamma_{int} = 1.5$,2,2.5 and 3 $\left[\frac{1}{year}\right]$.

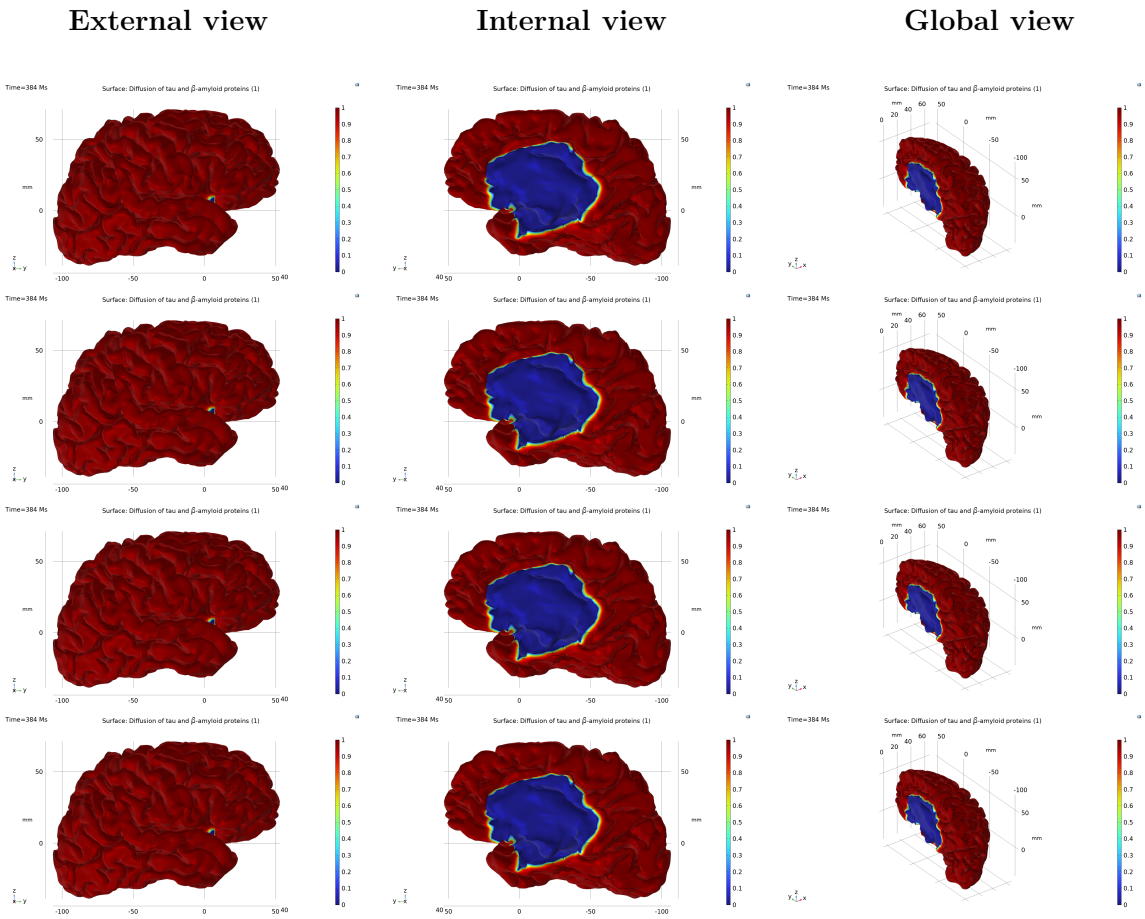

Figure 6.22: Year of evolution 32 with $\alpha_{tau} = 4\left[\frac{1}{year}\right]$, $\alpha_{\beta} = 5\left[\frac{1}{year}\right]$ fixed. From top to bottom, $\gamma_{int} = 1.5$,2,2.5 and 3 $\left[\frac{1}{year}\right]$.

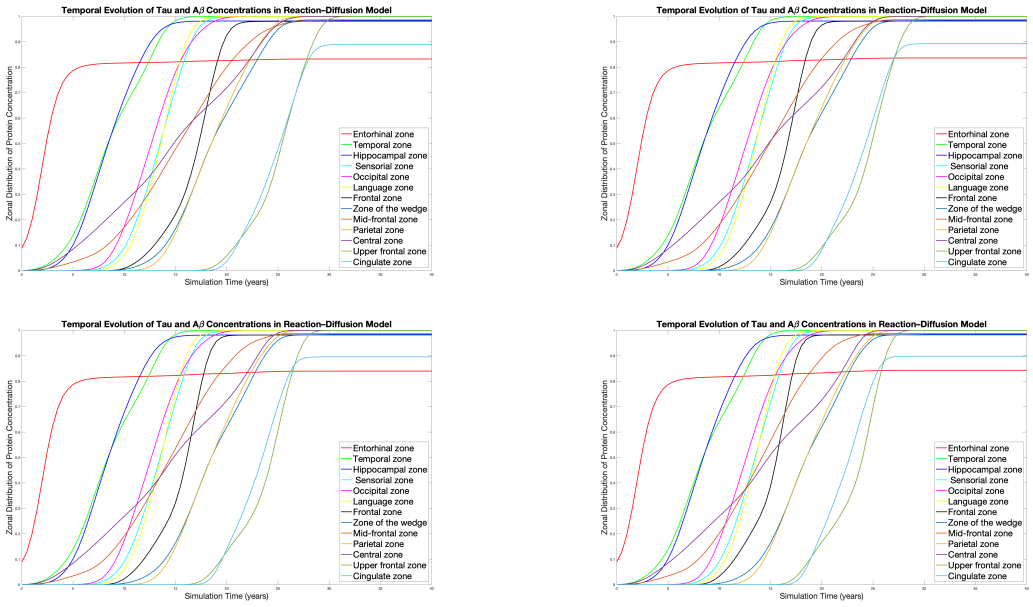

Figure 6.23: Trend of mean concentrations for each brain region resulting from simulations with $\alpha_{tau} = 4\left[\frac{1}{year}\right]$ and $\alpha_{\beta} = 5\left[\frac{1}{year}\right]$, for increasing values of the interaction parameter $\gamma_{int} = 1.5,2,2.5,3\ \left[\frac{1}{year}\right]$, respectively.

6.5.3 Case $\alpha_{tau} = \alpha_{\beta}$

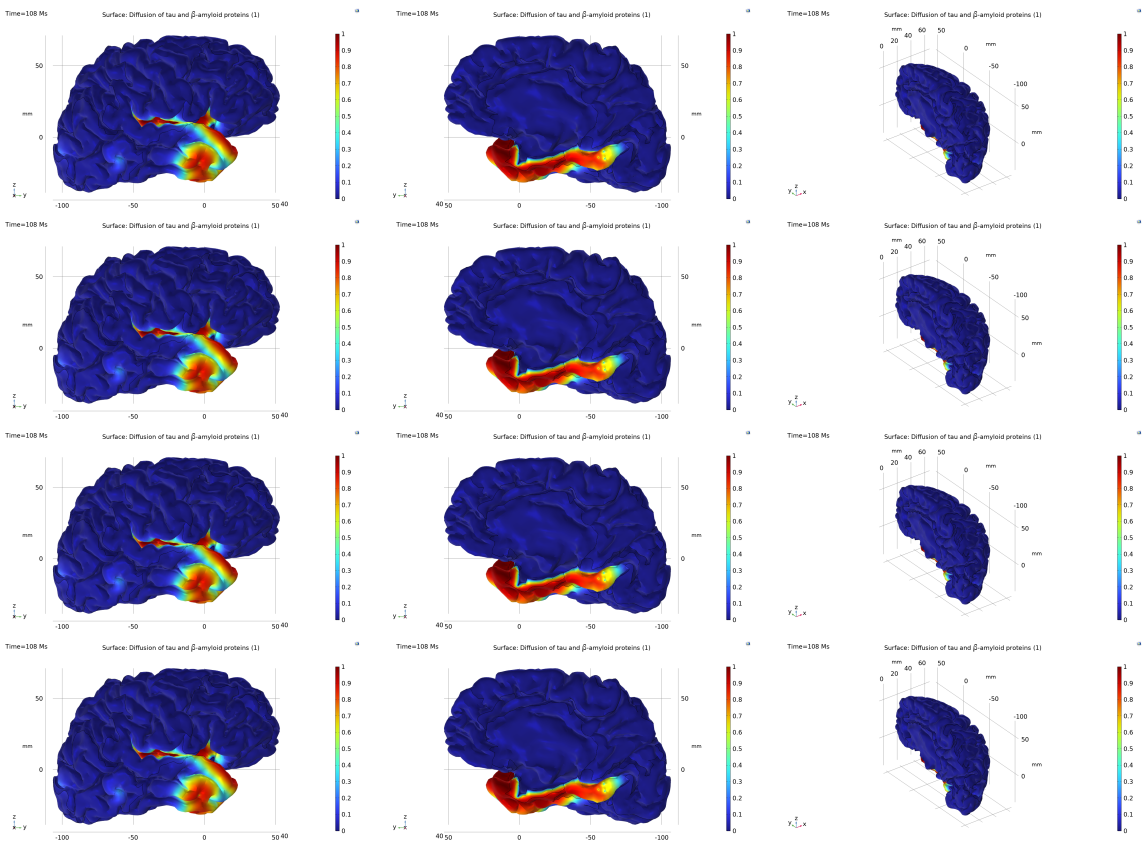

Figure 6.24: Year of evolution 9 with $\alpha_{tau} = 3\left[\frac{1}{year}\right]$, $\alpha_{\beta} = 3\left[\frac{1}{year}\right]$ fixed. From top to bottom, $\gamma_{int} = 1.5$,2,2.5 and $3\left[\frac{1}{year}\right]$.

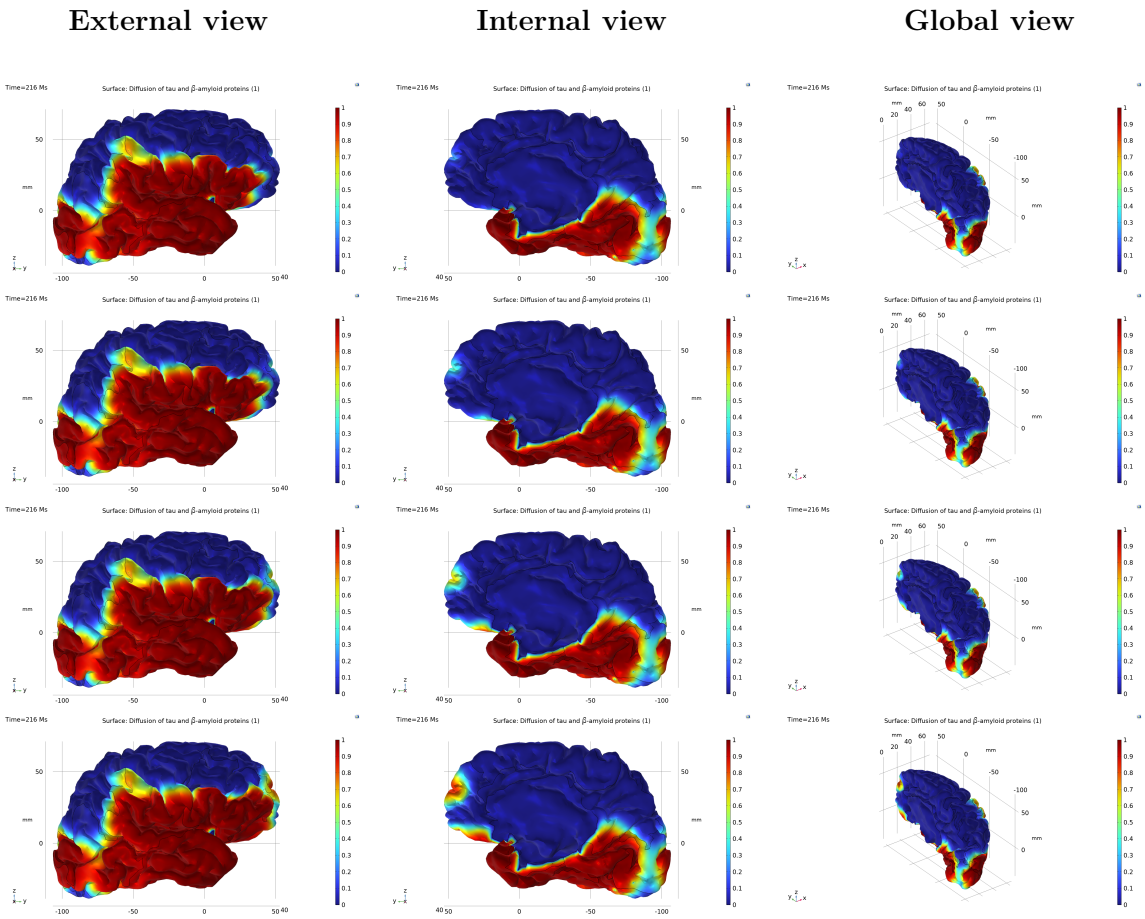

Figure 6.25: Year of evolution 18 with $\alpha_{tau} = 3\left[\frac{1}{year}\right]$, $\alpha_{\beta} = 3\left[\frac{1}{year}\right]$ fixed. From top to bottom, $\gamma_{int} = 1.5$,2,2.5 and $3\left[\frac{1}{year}\right]$.

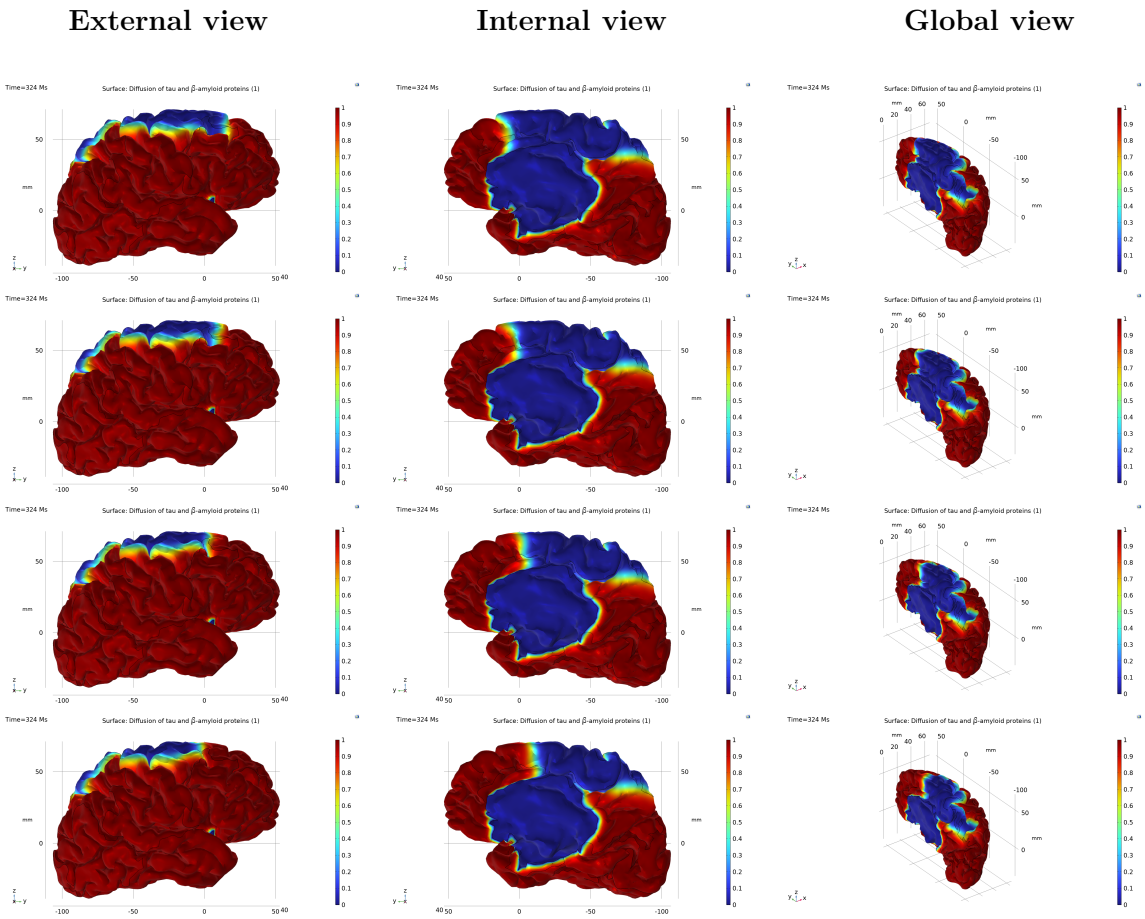

Figure 6.26: Year of evolution 27 with $\alpha_{tau} = 3\left[\frac{1}{year}\right]$, $\alpha_{\beta} = 3\left[\frac{1}{year}\right]$ fixed. From top to bottom, $\gamma_{int} = 1.5$,2,2.5 and $3\left[\frac{1}{year}\right]$.

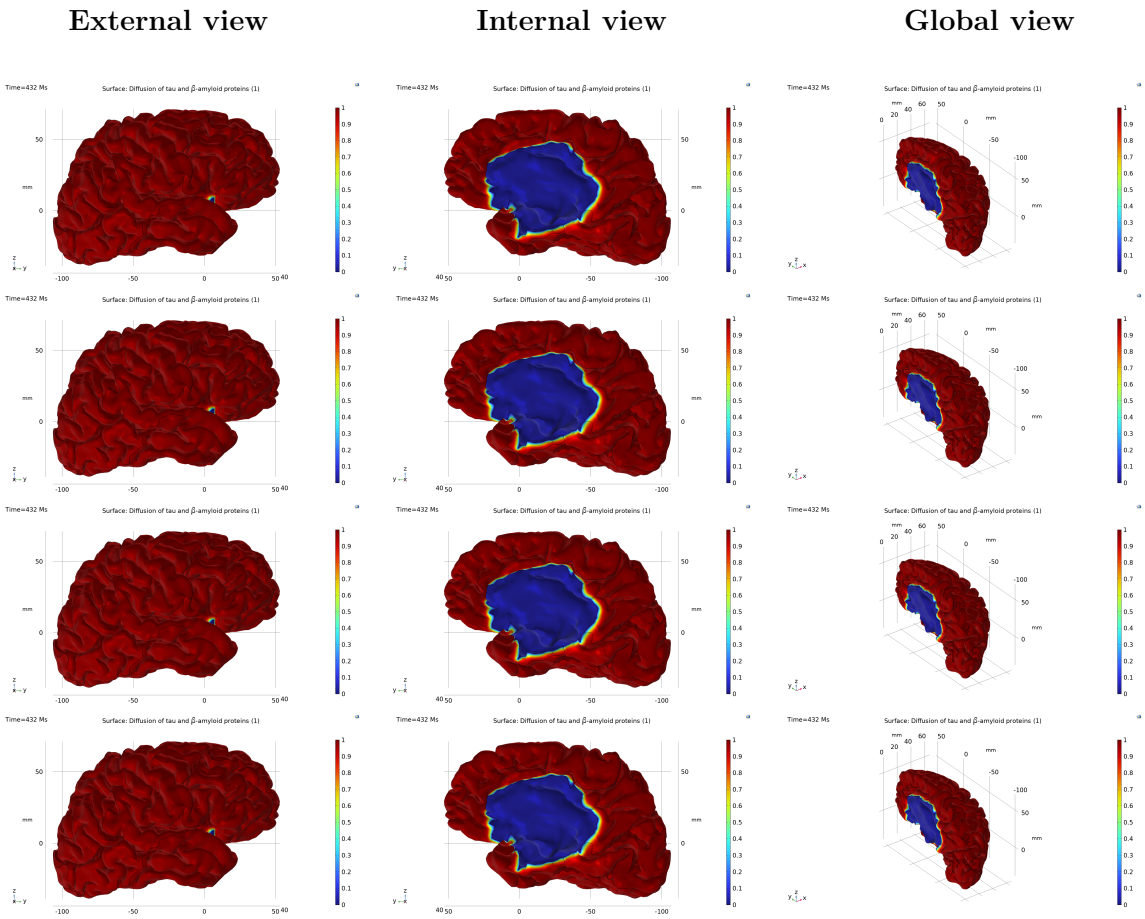

Figure 6.27: Year of evolution 36 with $\alpha_{tau} = 3\left[\frac{1}{year}\right]$, $\alpha_{\beta} = 3\left[\frac{1}{year}\right]$ fixed. From top to bottom, $\gamma_{int} = 1.5$,2,2.5 and $3\left[\frac{1}{year}\right]$.

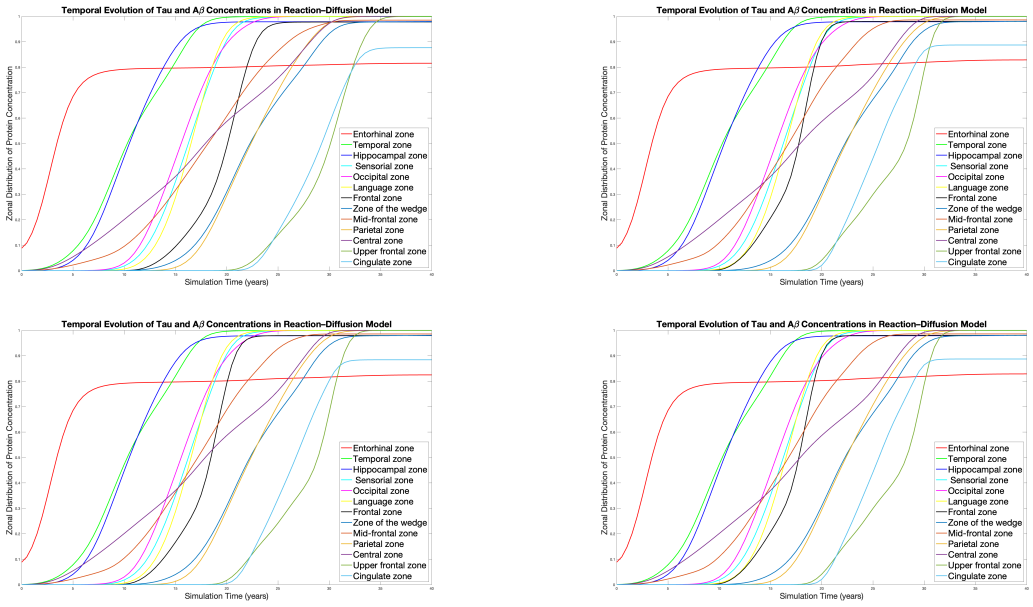

Figure 6.28: Trend of mean concentrations for each brain region resulting from simulations with $\alpha_{tau} = 3\left[\frac{1}{year}\right]$ and $\alpha_{\beta} = 3\left[\frac{1}{year}\right]$, for increasing values of the interaction parameter $\gamma_{int} = 1.5,2,2.5,3\ \left[\frac{1}{year}\right]$, respectively.

6.5.4 Overall results

Several significant results emerge from the analysis described above. Firstly, with the values considered, in the case where $\alpha_{tau} > \alpha_{\beta}$, an increase in the interaction coefficient γ_{int} corresponds to a gradual decrease in the cerebral cortex invasion time. Specifically, a 0.5 increment in γ_{int} results in an approximate reduction of 6 months in the overall invasion time. This behaviour suggests that a higher interaction rate between tau and β-amyloid proteins accelerates plaque formation, thereby hastening cognitive decline. A similar dynamic is observed when $\alpha_{tau} < \alpha_{\beta}$, although the effect is more pronounced. In this scenario, each 0.5 increment in γ_{int} leads to a reduction of about 12 months in the invasion time.

A fundamental aspect that emerges from the parametric study, visible in the tables 6.2 and 6.3 showing all the simulations, is the difference in the invasion times when the coefficient γ_{int} is kept constant. In particular, when $\alpha_{tau} > \alpha_{\beta}$, the invasion of the cerebral cortex occurs more rapidly than in the opposite case. This indicates that the disease progresses more aggressively under such conditions. Considering, for example, the simulations performed keeping the parameter $\gamma_{int} = 1.5 \left[\frac{1}{year}\right]$ constant: in the first case it is observed that the complete invasion of all brain regions can occur in as little as 28 years, whereas in the case $\alpha_{tau} < \alpha_{\beta}$, the complete accumulation of pathological proteins occurs at approximately 31 years. This result suggests a relatively slower progression of the disease, with the onset of severe cognitive decline delayed in the patient's clinical course. A similar trend is observed for values of $\gamma_{int} = 2$, 2.5 and 3 $\left[\frac{1}{year}\right]$.

A parallel tendency is also observed for the case where $\alpha_{tau} = \alpha_{\beta}$. Holding both coefficients constant while increasing γ_{int} results in a reduction of the invasion time. Specifically, for $\alpha_{tau} = 3 \left[\frac{1}{year}\right]$ and $\alpha_{\beta} = 3 \left[\frac{1}{year}\right]$, the maximum invasion time calculated is approximately 35.5 years, which decreases as γ_{int} increases. Tables 6.2 and 6.3 further illustrate that, as α_{tau} and α_{β} increase simultaneously, the invasion time decreases accordingly. Thus, the overall time trend is consistent with that observed in the two previous scenarios.

A qualitative analysis of the simulations reported can be conducted. In all three cases examined, at the initial time points considered (7, 8, and 9 years), it is evident that even in the presence of protein interaction, the connectome structure plays a fundamental role. This mechanism, which links spatially non-adjacent regions of the brain, facilitates diffusion in multiple directions. The distinct 'spots' observed in the lower left frontal view of the cerebral cortex, shown in the first column of Figures 6.14, 6.19, and 6.24, correspond to the propagation of tau protein originating from the areas depicted in the adjacent snapshots, representing the brain's inner view.

The enlargement of these initial 'spots', combined with the progressive tau diffusion from the temporal region, leads to the eventual invasion of all brain areas. This progression can be observed in the snapshots presented in Figures 6.15, 6.20, and 6.25. The second time frame, particularly in the central view, represents a key moment for highlighting how an increase in the interaction parameter γ_{int} results in a temporally accelerated diffusion process across all examined cases. In the upper left portion of these images, corresponding to the frontal region, a red area is visible, indicating high concentrations of the diffusing tau and β-amyloid proteins. This region becomes more pronounced and spatially extended in the simulations where, for fixed values of α_{tau} and α_{β}, a higher value of γ_{int} is employed.

The results presented further underscore the significance of the interaction parameter γ_{int}, which strongly influences both the timing and the rate of disease progression. In figures 6.16, 6.21, and 6.26, which represent advanced diffusion stages, an increasingly accelerated propagation is observed as γ_{int} increases. In the frontal views on the left of each figure, the uninvolved cortical regions, displays in blue, progressively decrease in size. A similar trend is visible in the central inner-brain views, where the upper-frontal and cingulate areas exhibit a more extensive accumulation of pathological proteins for higher values of γ_{int}. Finally, in the full-brain views on the right, the superior region and part of the wedge zone are shown to approach full plaque formation. This effect becomes increasingly evident when examining the figures from top to bottom, further reinforcing the accelerating impact of protein interaction on disease spread.

In the snapshots shown in figures 6.17, 6.22 and 6.27, the simulations display the final stage of disease progression, characterised by the complete invasion of the cerebral cortex by the pathological proteins tau and β-amyloid. This state corresponds to the maximum saturation of the system and is strongly associated with the most severe cognitive and neurological disturbances observed in the advanced stages of Alzheimer's disease. A comparative analysis of these final-stage snapshots reveals a key trend: as the interaction parameter γ_{int} increases, the spatial uniformity of the protein concentration becomes more pronounced and is reached in a shorter time-frame. This suggests that the strength of the interaction between tau and β-amyloid proteins significantly influences the global dynamics of disease spread, effectively accelerating the transition from localised pathology to widespread neurodegeneration.

This spatial progression is further supported by the temporal graphs of average concentrations for each brain region reported in figures 6.18, 6.23, and 6.28, which consistently show a sigmoidal shape. These curves not only illustrate the progressive temporal accumulation in different regions at the onset of pathology, but also reflect the interplay between intrinsic diffusion parameters and non-linear effects introduced by protein interactions. An increase in γ_{int} results in an earlier inflection point and a steeper growth rate in the concentration curves, underscoring the pivotal role of protein interaction in accelerating both the onset and spatial progression of the pathology.

Table 6.4 shows the values of the parameters selected for the simulations discussed above, while figure 6.29 illustrates the time course of the resulting invasion in the three scenarios considered. The curves highlight the influence of the interaction parameter γ_{int} on the temporal dynamics of disease progression.

In particular, the green line corresponds to the case where $\alpha_{tau} = \alpha_{\beta} = 3\left[\frac{1}{year}\right]$, with the black dots indicating the invasion times calculated at increasing values of γ_{int}. The light blue line represents the scenario $\alpha_{tau} < \alpha_{\beta}$, with blue dots indicating the associated invasion times. In contrast, the magenta line refers to the $\alpha_{tau} > \alpha_{\beta}$ case, with red dots indicating the times resulting from each simulation.

These trends collectively demonstrate how increasing γ_{int} accelerates disease progression in all configurations, with changes in α_{tau} and α_{β} modulating the overall rate and timing of cortical invasion.

$\alpha_{tau}\left[\frac{1}{year}\right]$	$\alpha_{\beta}\left[\frac{1}{year}\right]$	$\gamma_{int}\left[\frac{1}{year}\right]$	**Invasion Time (years)**
5	3	1.5	28
		2	27.5
		2.5	27
		3	26.5
4	5	1.5	31
		2	30
		2.5	29
		3	28
3	3	1.5	35.5
		2	34.5
		2.5	33.5
		3	32.5

Table 6.4: Table with the parameters of the simulations shown in the figures 6.14, 6.15, 6.16, 6.17, 6.19, 6.20, 6.21, 6.22, 6.24, 6.25, 6.26, 6.27.

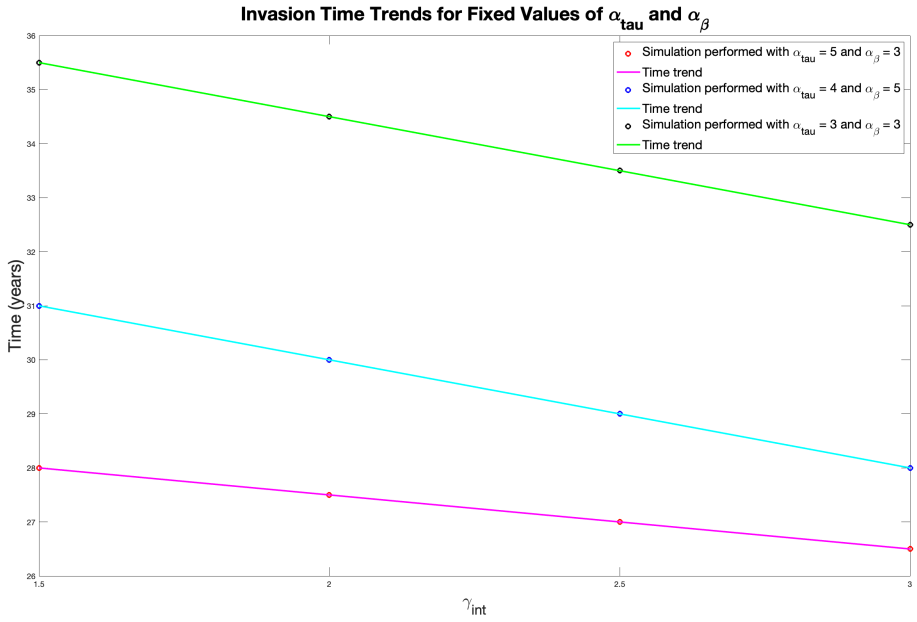

Figure 6.29: The graph illustrates the temporal evolution of cerebral cortex invasion times as a function of the interaction parameter γ_{int}. A consistent decrease in invasion time is observed with increasing γ_{int}, highlighting the accelerating effect of protein interaction on disease progression. Specifically, the light blue curve represents the case $\alpha_{tau} = 4\left[\frac{1}{year}\right]$ and $\alpha_{\beta} = 5\left[\frac{1}{year}\right]$, the magenta curve corresponds to $\alpha_{tau} = 5\left[\frac{1}{year}\right]$ and $\alpha_{\beta} = 3\left[\frac{1}{year}\right]$, and the green curve illustrates the scenario with $\alpha_{tau} = 3\left[\frac{1}{year}\right]$ and $\alpha_{\beta} = 3\left[\frac{1}{year}\right]$.

The observed trends appear consistent across all cases, reaffirming that an increase in the interaction parameter γ_{int} leads to a decrease in the invasion time of the cerebral cortex. This behaviour is further confirmed in the scenario where $\alpha_{tau} = \alpha_{\beta}$, extended to the cases with both coefficients equal to $4\left[\frac{1}{year}\right]$ and $5\left[\frac{1}{year}\right]$.

These results are presented in figure 6.30. The graph further demonstrates that even when α_{tau} and α_{β} are simultaneously increased, the overall temporal dynamics remain unchanged: higher values of γ_{int} consistently result in shorter plaque formation times, indicating a faster progression of the disease and a more rapid onset of cognitive decline.

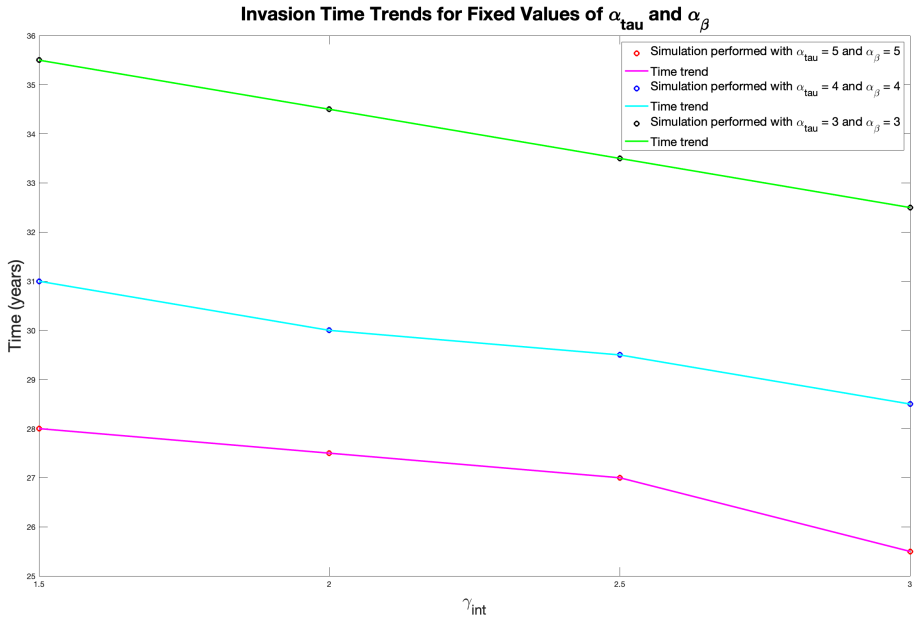

Figure 6.30: The graph illustrates the temporal evolution of cerebral cortex invasion times as a function of the interaction parameter γ_{int}. A consistent decrease in invasion time is observed with increasing γ_{int}, highlighting the accelerating effect of protein interaction on disease progression. Specifically, the light blue curve represents the case $\alpha_{tau} = 4\left[\frac{1}{year}\right]$ and $\alpha_{\beta} = 4\left[\frac{1}{year}\right]$, the magenta curve corresponds to $\alpha_{tau} = 5\left[\frac{1}{year}\right]$ and $\alpha_{\beta} = 5\left[\frac{1}{year}\right]$, and the green curve illustrates the scenario with $\alpha_{tau} = 3\left[\frac{1}{year}\right]$ and $\alpha_{\beta} = 3\left[\frac{1}{year}\right]$.

7. Application of the Model to Patient-Specific Data

The application of the reaction–diffusion model defined in equation (5.3) is now presented, incorporating an extended range for the concentrations of tau and β-amyloid proteins. Four patients were selected as representative cases, each corresponding to a distinct stage of Alzheimer's disease progression.

Prior to the presentation of the simulation results, it is useful to outline the clinical classification framework used for patients with Alzheimer's disease and the parameters involved. When a patient undergoes a PET (Positron Emission Tomography) scan, used to assess the average concentration of pathological proteins in the brain, the resulting data are spatially distributed across the 84 anatomical regions into which the brain is subdivided. This regional segmentation enables a detailed mapping of protein accumulation.

In parallel, patients are subjected to cognitive evaluations, from which specific clinical indices are derived to support disease staging and classification.

One of the most widely adopted metrics is the Mini-Mental State Examination (MMSE), a neuropsychological test designed to assess global cognitive function. The test has a maximum score of 30, with lower scores indicating increasing cognitive impairment. In clinical settings, the MMSE is routinely employed to monitor disease progression and categorize patients by the severity of cognitive decline. However, recent literature suggests that the MMSE alone may not serve as a reliable predictor of disease trajectory, thereby motivating the integration of additional biomarkers and diagnostic modalities for more comprehensive assessments [27].

Based on MMSE scores in combination with PET scan findings, patients are generally classified into four broad categories that reflect the degree of cognitive decline:

1. Cognitive Normals (CN): MMSE $28 - 30$, PET scan with no pathological findings.
2. Mild Cognitive Impairment (MCI): MMSE $24 - 27$, PET scan indicating mild hypometabolism.
3. Mild Dementia: MMSE $20 - 23$, PET scan showing moderate hypometabolism.
4. Moderate to Severe Dementia: MMSE < 20, PET scan revealing extensive hypometabolism.

7.1 Case study

The present case study focuses on a cohort of four patients, each exhibiting Alzheimer's disease at different stages of progression.

For each subject, the following clinical and demographic information was collected: the RID (Research ID) associated with the ADNI database [1], the Mini-Mental State Examination (MMSE) score, the diagnostic category (GROUP) to which the subject was assigned, chronological age, and the mean regional concentrations of tau and β-amyloid proteins as obtained from PET imaging data.

To integrate clinical imaging data with the mathematical model developed in this study, the original division of the brain into 84 regions was adapted to match the 14 macro-regions defined within the computational framework. This aggregation was performed by calculating the average value of protein concentration within each macro-area, based on the individual values from the original 84 regions. This transformation ensured consistency between clinical observations and simulation domains, facilitating a meaningful comparison between real and simulated data.

As with the parametric studies presented earlier, the inner zone is excluded from this analysis, since it is not directly involved in the local accumulation of pathological proteins. For this reason, its associated mean concentration remains null and does not appear in table 7.1.

ID	Patient 1	Patient 2	Patient 3	Patient 4
RID	31	800	1190	467
GROUP	CN	MCI	DEMENTIA	DEMENTIA
AGE	90.18	83.01	87.27	91.1
MMSE	30	26	25	19
Entorhinal zone	0.61	2.35	2.44	2.61
Temporal zone	0.07	2.21	3	3
Hippocampal zone	0.01	2.44	2.95	3
Sensorial zone	0.005	0.52	2.98	3
Occipital zone	0.003	0.77	2.91	3
Language zone	0.0007	0.45	3	3
Frontal zone	0.003	2.12	2.97	3
Zone of the wedge	0.0002	0.007	1.99	2.9
Mid-frontal zone	0.02	2.12	3	2.92
Parietal zone	0.0001	0.0001	1.89	3
Central zone	0.04	0.45	2.48	3
Upper-frontal zone	0.003	0.43	2.21	3
Cingulate zone	0.001	1.12	2.31	2.44

Table 7.1: Average concentrations of tau and β-amyloid proteins calculated and adjusted within the 14 macro-areas into which the brain was subdivided for the purposes of this study. The values refer to four patients, each presenting Alzheimer's disease at a different stage of progression. The inner zone is not included because it is not directly affected by the diffusion or accumulation of misfolded proteins and therefore consistently exhibits zero concentration.

7.2 Model 3: Clinically adapted model for patient data integration

Following the adaptation of the interaction model to accommodate clinically realistic concentration limits for misfolded proteins, the simulation framework was applied to a cohort of four patients diagnosed with Alzheimer's disease at different stages of progression. The simulations, based on system (5.3), incorporate patient-specific data and enable the analysis of tau and β-amyloid propagation dynamics in vivo.

$$\begin{cases} \dfrac{\partial u_{tau}}{\partial t} = D\nabla^2 u_{tau} + \alpha_{tau} u_{tau}(3 - u_{tau}) + \gamma_{int} u_\beta u_{tau}(3 - u_{tau})\mathbb{H}(t - 16) & \text{in } \Omega \setminus \Omega_{int} \\ \dfrac{\partial u_\beta}{\partial t} = D\nabla^2 u_\beta + \alpha_\beta u_\beta(3 - u_\beta) & \text{in } \Omega \setminus \Omega_{int} \\ \dfrac{\partial u_{tau}}{\partial t} = ND\nabla^2 u_{tau} & \text{in } \Omega_c \\ u_{tau}(t = 0) = u_{0,tau} & \text{in } \Omega_e \\ u_{tau}(t = 0) = 0 & \text{in } \Omega \setminus \Omega_e \\ u_\beta(t = 0) = u_{0,\beta} & \text{in } \Omega_f \\ u_\beta(t = 0) = 0 & \text{in } \Omega \setminus \Omega_f \end{cases} \tag{7.1}$$

In this patient-specific analysis, the diffusion coefficient was maintained at $D = 10\left[\frac{mm^2}{year}\right]$, and the connectome scaling factor was set to $N = 10^6$, consistent with the previous simulations. For all simulations described below, the initial concentrations of misfolded proteins were uniformly set to 0.05 for both $u_{0,tau}$ and $u_{0,\beta}$.

The primary objective of this study is to identify, for each patient, the specific time point along the simulated disease trajectory that best corresponds to their clinical condition, as inferred from PET imaging data. In particular, the goal is to determine the simulation step at which the spatial distribution and mean concentrations of misfolded proteins match those observed in the patient's brain. Once this temporal alignment is achieved, the model can then be used to qualitatively predict the future evolution of pathological burden, offering valuable insight into the expected progression of cognitive decline in each individual case.

To this end, a comprehensive series of numerical simulations was performed, systematically varying the reaction parameters α_{tau} and α_β, which govern the autocatalytic accumulation of tau and β-amyloid, respectively, as well as the interaction parameter γ_{int}, which regulates the synergistic feedback between the two proteins. The resulting simulation outputs were then compared with the PET-derived concentration patterns to identify the configuration that most accurately reflects each patient's current disease stage.

7.3 Results

This section presents the results obtained from the application of model (7.1) to the individual cases listed in table 7.1. For each simulation, the average concentrations of misfolded proteins were computed and recorded for each of the defined brain regions, enabling a direct comparison with the PET-derived values. Based on the positioning of the PET

values along the simulated temporal evolution, a corresponding average reference year was inferred for each patient, representing the estimated stage of disease progression.

The first simulation was performed using the following parameter values: $\alpha_{tau} = 0.9 \left[\frac{1}{year}\right]$, $\alpha_{\beta} = 0.9 \left[\frac{1}{year}\right]$, and $\gamma_{int} = 1.2 \left[\frac{1}{year}\right]$. This configuration corresponds to a scenario in which the transformation rates of healthy tau and β-amyloid proteins into their misfolded counterparts are equal.

First and foremost, it is evident that in this scenario, the total invasion of the cerebral cortex occurs approximately 35 years after the initial onset of misfolded protein propagation. The diffusion process, originating in the entorhinal cortex, follows a progression pattern remarkably similar to that observed in the earlier simulations. Notably, the cingulate cortex and the upper-frontal regions continue to represent the final areas to be affected, reflecting a consistent and biologically plausible trajectory. Following the simulation, the spatially averaged concentration values for each brain region were meticulously recorded and subsequently compared with the corresponding PET-derived measurements for each individual patient.

The analysis begins with the first patient, who is approximately 90 years old, presents an MMSE score of 30, and is identified by the RID code 31. This individual belongs to the Cognitively Normal (CN) group, exhibiting no significant abnormalities in the PET scan. This positioning makes him a crucially representative subject for the early — or potentially even preclinical — stage of disease progression. This is supported by the low average concentrations of tau and β-amyloid proteins, which remain significantly below the critical 3 threshold established for complete cortical invasion. Based on these observations, the model estimates that the patient's disease course corresponds to within the first 10 years following the initial onset of protein propagation. This inference aligns with the patient's clinical profile: the MMSE score of 30 and classification within the Cognitively Normal (CN) group all indicate the absence of overt symptoms typically associated with Alzheimer's progression. This assessment is further supported by the MMSE result, which shows no measurable deficits in the main cognitive domains, including attention, memory, orientation, language, and executive functions, reinforcing the thesis that the patient is in a pre-clinical phase of the disease.

The next step involves analysing the comparison between protein concentrations measured via PET imaging and those simulated by the proposed model. The highest concentrations are consistently observed in the entorhinal, temporal, and hippocampal regions, areas known to be the initial sites of pathological onset. According to the connectome-based diffusion structure implemented in the model, these regions exhibit strong connectivity with the central and mid-frontal zones, which indeed display elevated levels of misfolded proteins in the simulations. Based on this correspondence, the model estimates the average disease progression time for this patient to be 8.26 years, suggesting that the pathological process began approximately eight years prior to the imaging evaluation.

Table 7.2 presents a detailed comparison between the PET-derived concentrations, the simulated values, and the corresponding simulation time points at which these concentrations are reached. Additionally, histogram 7.1 graphically illustrates the discrepancy between clinical observations and model outputs, offering a visual assessment of the model's predictive accuracy in reproducing the patient-specific pathological burden.

Zones	Patient 1 values	Simulation values	Reference times (years)
Entorhinal zone	0.61	0.607	4
Temporal zone	0.07	0.071	5
Hippocampal zone	0.01	0.013	4.5
Sensorial zone	0.005	0.0036	9.5
Occipital zone	0.003	0.0034	9
Language zone	0.0007	0.0008	9.5
Frontal zone	0.003	0.0007	8
Zone of the wedge	0.0002	0.0002	10.5
Mid-frontal zone	0.02	0.024	5
Parietal zone	0.0001	0.0001	13
Central zone	0.04	0.039	4.5
Upper-frontal zone	0.003	0.003	12.5
Cingulate zone	0.001	0.0003	12.5

Table 7.2: Average concentrations of tau and β-amyloid proteins measured via the patient's PET scan, alongside the corresponding concentrations obtained from the simulation conducted with parameters $\alpha_{tau} = 0.9 \left[\frac{1}{\text{year}}\right]$, $\alpha_{\beta} = 0.9 \left[\frac{1}{\text{year}}\right]$, and $\gamma_{int} = 1.2 \left[\frac{1}{\text{year}}\right]$, as well as the respective reference times at which these simulated concentrations were recorded.

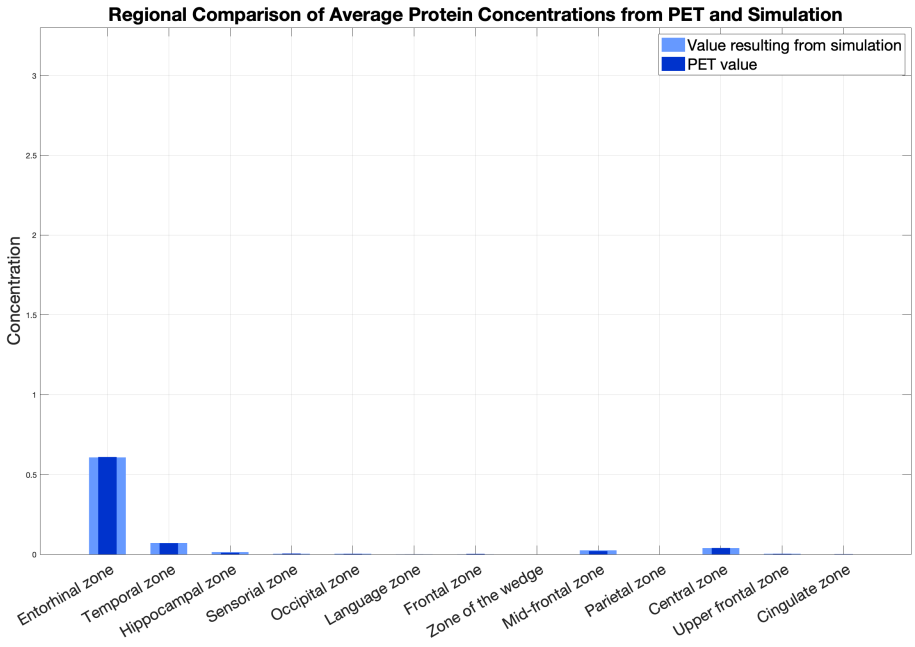

Figure 7.1: Comparison between the average concentrations obtained from the patient's PET scan (darker bars) and those computed by the simulation with parameters $\alpha_{tau} = 0.9 \left[\frac{1}{year}\right]$, $\alpha_{\beta} = 0.9 \left[\frac{1}{year}\right]$ and $\gamma_{int} = 1.2 \left[\frac{1}{year}\right]$ (lighter bars) for patient 1.

It is possible to make a further observation on the progression of Alzheimer's disease in patient 1. Going to investigate the sigmoids resulting from the simulation carried out in the figure 7.2, one can see the hypothesized diffusion of tau and β-amyloid proteins zone by zone. Plotting the values obtained from the PET scan on the graph, by means of filled dots, one obtains that their dislocation occurs in the first 12 years of the simulation, in the zone where the sigmoids representing most of the areas interesting from the diffusion have not risen yet. This leads to the assumption that the average protein concentration is still very low within the entire cerebral cortex. The only exception is observed for the entorhinal area, which in fact turns out to be the site of disease onset.

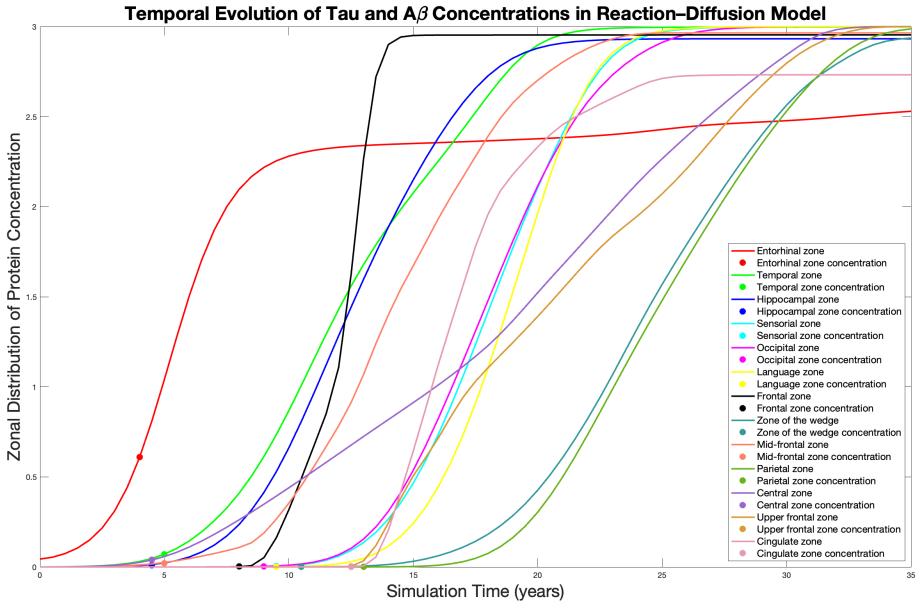

Figure 7.2: Trend of mean concentrations of tau and β-amyloid proteins in the simulation with parameters $\alpha_{tau} = 0.9\left[\frac{1}{year}\right]$, $\alpha_{\beta} = 0.9\left[\frac{1}{year}\right]$ and $\gamma_{int} = 1.2\left[\frac{1}{year}\right]$. The dots represent the average concentrations per zone calculated by PET for patient 1.

A comparison between the patient's condition at the time of the PET scan and the corresponding simulation output at the estimated average disease stage is shown in figure 7.3.

The simulation presents three views of the cerebral cortex at year 8 of disease progression, a time point selected based on the average concentrations derived from the PET data. This corresponds to the stage in which the model predicts similar levels of pathological protein accumulation. It is noticeable that the entorhinal zone exhibits a higher concentration of misfolded proteins in the simulation compared to the PET scan. This discrepancy can be explained by the fact that this region is one of the earliest sites of tau accumulation; therefore, its local concentration may exceed the average at the reference time. Apart from this local difference, the spatial distribution of pathological proteins across the cortex shows good agreement between simulation and clinical data, supporting the validity of the

model in reproducing the patient's condition at the estimated stage of disease.

Finally, the simulation illustrates how the connectome structure facilitates the spread of tau and β-amyloid proteins from the entorhinal cortex to adjacent areas, such as the temporal lobe. This process is visually captured by the signal observed in the lower right quadrant of the second cortical view.

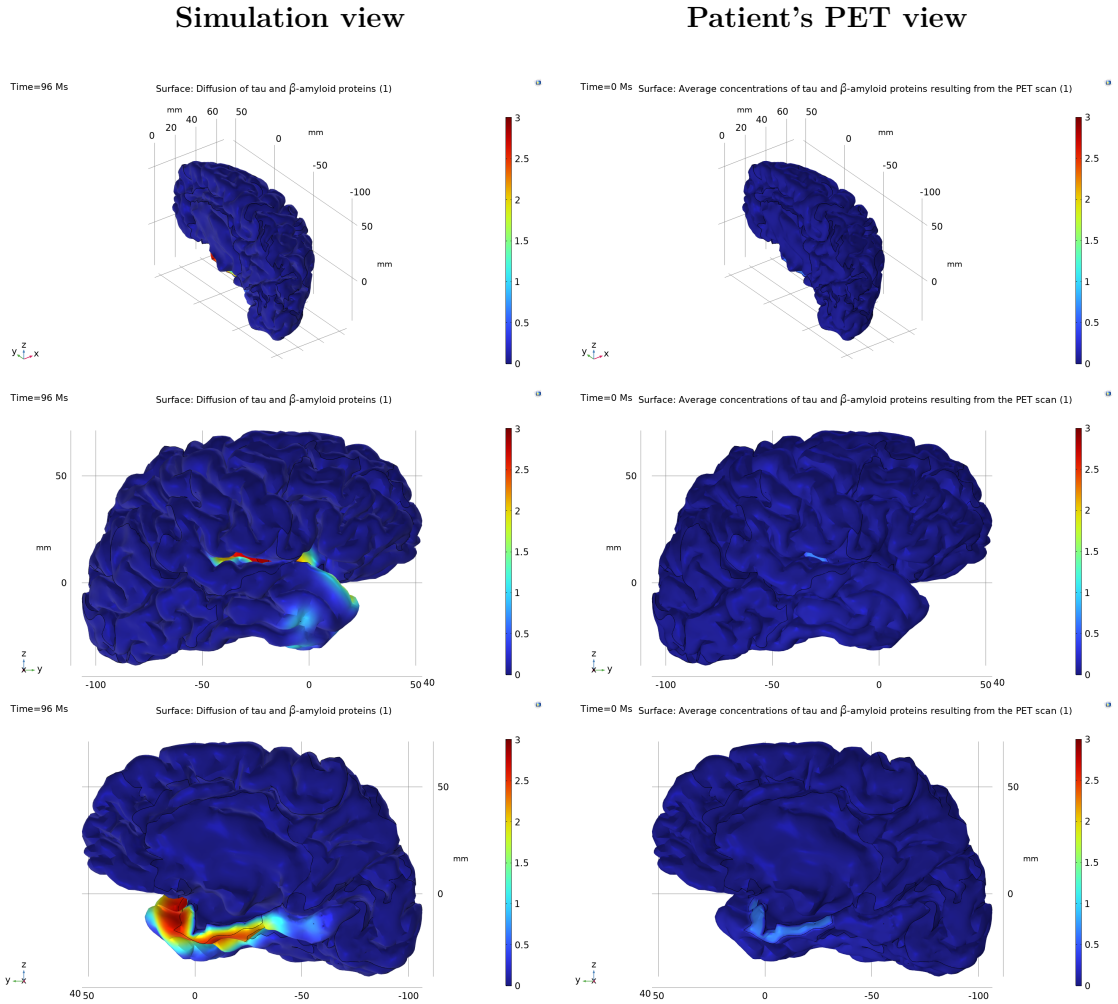

Figure 7.3: Comparison between the simulation with the parameters $\alpha_{tau} = 0.9\left[\frac{1}{year}\right]$, $\alpha_{\beta} = 0.9\left[\frac{1}{year}\right]$, $\gamma_{int} = 1.2\left[\frac{1}{year}\right]$ and the real data for patient 1. Left: view of the cerebral cortex invasion trend at time 96 months. Right: view of the cerebral cortex with the values of the concentrations calculated by PET in the respective areas.

The same type of analysis was carried out for patient 2 (RID= 800). The patient is 83 years old, has an MMSE score of 26, and belongs to the MCI (Mild Cognitive Impairment) diagnostic group.

Based on these clinical indicators, it can be inferred that the patient presents with symptoms typically associated with MCI, such as memory lapses and mild cognitive difficulties, as reflected in the Mini-Mental State Examination score. Common manifestations at this stage may include forgetfulness regarding recent events, repetition of questions, and difficulty retaining new information. Language-related disorders may involve word-finding difficulties or naming errors, while orientation-related problems may include confusion about dates and times or episodes of distraction and slowed cognitive processing. Despite these symptoms, the patient maintains an overall preserved level of functional independence and does not yet meet the criteria for dementia. However, the risk of progression to Alzheimer's disease increases with age and severity of symptoms.

Analysing the average concentrations of simulated misfolded proteins by zone, it is evident that regions involved in memory, language and orientation are already significantly affected. In particular, many of these regions have concentrations above the 2 threshold value.

The model estimates the patient's position within the disease timeline to be at year 14.73, thus approximately 15 years from the onset of misfolded protein propagation. According to the simulation, the pathological proteins spread beyond the entorhinal cortex and reached the temporal, hippocampal, sensorial, and language areas. Through the connectome structure, further progression to the central and frontal cortical regions is evident.

Table 7.3 reports the average protein concentrations measured from the patient's PET scan, the corresponding values obtained from the simulation, and the estimated year at which each concentration level is reached in the model.

Zones	Patient 2 values	Simulation values	Reference times (years)
Entorhinal zone	2.35	2.350	15
Temporal zone	2.21	2.252	16
Hippocampal zone	2.44	2.484	16.5
Sensorial zone	0.52	0.465	15
Occipital zone	0.77	0.823	16
Language zone	0.45	0.444	16
Frontal zone	2.12	2.263	13
Zone of the wedge	0.007	0.008	13.5
Mid-frontal zone	2.12	2.165	17
Parietal zone	0.0001	0.0001	13
Central zone	0.45	0.439	10
Upper-frontal zone	0.43	0.383	14.5
Cingulate zone	1.12	1.121	16

Table 7.3: Average concentrations of tau and β-amyloid proteins measured via the patient's PET scan, alongside the corresponding concentrations obtained from the simulation conducted with parameters $\alpha_{tau} = 0.9 \left[\frac{1}{\text{year}}\right]$, $\alpha_{\beta} = 0.9 \left[\frac{1}{\text{year}}\right]$, and $\gamma_{int} = 1.2 \left[\frac{1}{\text{year}}\right]$, as well as the respective reference times at which these simulated concentrations were recorded.

The histogram in figure 7.4 illustrates the discrepancy between the PET-derived and simulated data. Overall, the simulation results show good agreement with the concentrations measured from the PET scan, confirming the model's ability to reproduce the observed protein distribution in the patient's brain.

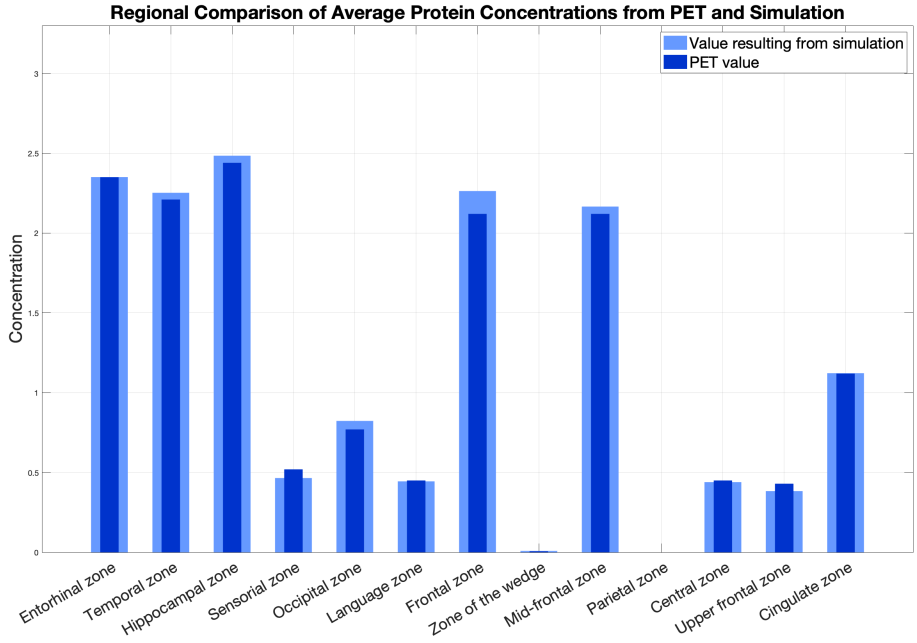

Figure 7.4: Comparison between the average concentrations obtained from the patient's PET scan (darker bars) and those computed by the simulation with parameters $\alpha_{tau} = 0.9\left[\frac{1}{year}\right]$, $\alpha_{\beta} = 0.9\left[\frac{1}{year}\right]$ and $\gamma_{int} = 1.2\left[\frac{1}{year}\right]$ (lighter bars) for patient 2.

Finally, the temporal trends of the average protein concentrations per zone and the positioning of the values derived from the PET scan for patient 2 are examined.

As shown in figure 7.5, the markers representing the patient's average concentrations are mostly clustered around years 15 and 16 of the simulation, with the exception of the central area, which still exhibits a relatively low level of diffusion and corresponds to an earlier simulation time, approximately year 10. In particular, all reference values fall within the ascending phase of the concentration curves. This temporal location is consistent with the patient's clinical symptoms and suggests a phase of the disease characterised by the initial formation and accumulation of misfolded protein plaques, particularly in brain regions associated with memory, language, and spatial orientation.

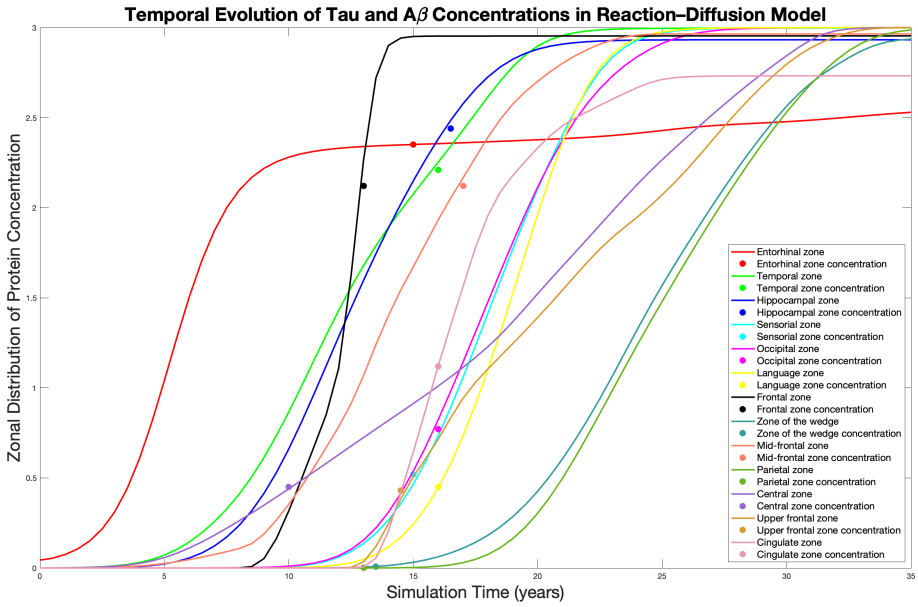

Figure 7.5: Trend of mean concentrations of tau and β-amyloid proteins in the simulation with parameters $\alpha_{tau} = 0.9 \left[\frac{1}{year}\right]$, $\alpha_{\beta} = 0.9 \left[\frac{1}{year}\right]$ and $\gamma_{int} = 1.2 \left[\frac{1}{year}\right]$. The dots represent the average concentrations per zone calculated by PET for patient 2.

Finally, the correspondence between the simulation and the actual PET data is examined. For patient 2, the simulation at year 15, very close to the computed average invasion time, was selected for comparison.

The correspondence between the simulated model and the observed data appears to be quite strong. The entorhinal and hippocampal regions are completely invaded by misfolded proteins, as indicated by their dark red colouring in the simulation. Temporal and frontal regions, which are later in the progression pathway, show intermediate levels of involvement, represented by lighter shades. The remaining regions, on the other hand, show predominantly blue tones, indicating limited or no invasion at this stage.

The differences in colour intensity between the PET data and the simulation can be explained by the nature of the two data representations. In simulation, protein diffusion is continuous and spatially heterogeneous: pathological proteins gradually propagate both locally and through the connectome structure, leading to partial and spatially variable saturation within each region. In contrast, PET imaging provides an average value for each anatomical region, represented uniformly. To reconcile these perspectives, one can imagine that a region with partial invasion, as suggested by the simulation, has a composite protein concentration, resulting from both strongly affected subregions (darker tones) and subregions not yet affected (lighter or blue tones). The PET value, in this case, actually reflects an average of these internal variations.

Therefore, the shades observed in the simulated cortical maps are consistent with the average concentrations recorded in the PET data. This supports the conclusion that the estimated average disease time is a plausible representation of the patient's actual disease

stage.

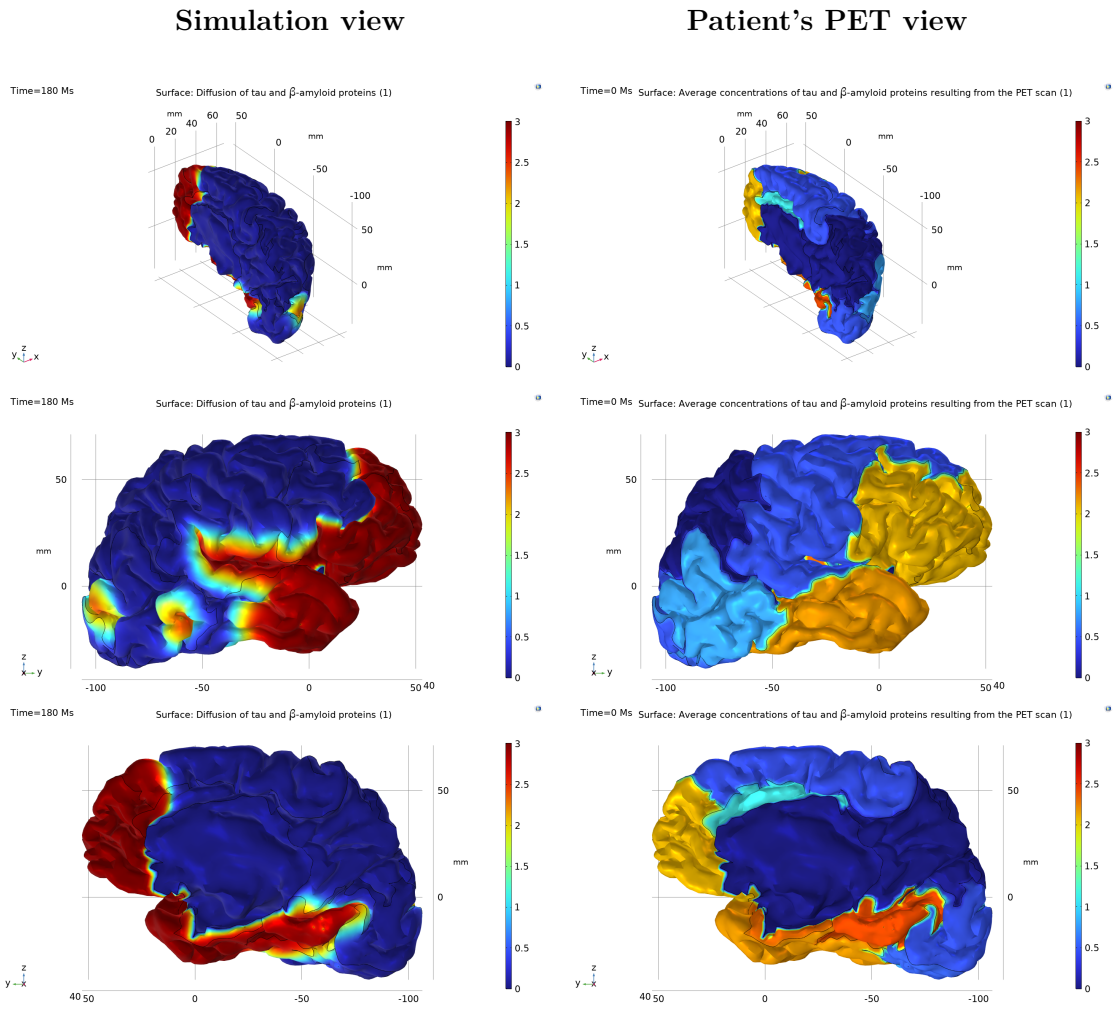

Figure 7.6: Comparison between the simulation with the parameters $\alpha_{tau} = 0.9 \left[\frac{1}{year}\right]$, $\alpha_{\beta} = 0.9 \left[\frac{1}{year}\right]$, $\gamma_{int} = 1.2 \left[\frac{1}{year}\right]$ and the real data for patient 2. Left: view of the cerebral cortex invasion trend at time 180 months. Right: view of the cerebral cortex with the values of the concentrations calculated by PET in the respective areas.

The same type of analysis was conducted for patient 3 (RID = 1190). This individual is approximately 87 years old and has an MMSE score of 25, placing him within the range for Mild Cognitive Impairment (MCI).

The symptoms typically associated with this condition are slight but evident to both the patient and those around them. They may include difficulties with recent memory, such as repeating questions or statements or forgetting names and appointments, temporal or spatial disorientation, language-related difficulties (e.g. difficulty following complex conversations) and disturbances in planning or organisation of tasks. From a psychological point of view, changes in humour and behaviour may also be present, including anxiety, irritability, or depression, often related to difficulties in daily functioning.

As shown in table 7.4, the temporal, hippocampal, sensorial, and language regions show average protein concentrations close to the saturation threshold, suggesting that these areas are completely or almost completely invaded by misfolded proteins. These numerical results are consistent with the clinical symptoms manifested by the patient. Furthermore, the simulation results closely match the PET-derived data, with an average stage of disease progression corresponding to year 25.73, i.e. approximately 26 years from the onset of pathological protein propagation.

The histogram in figure 7.7 provides a visual comparison between the average protein concentrations derived from the patient's PET scan and those predicted by the computational model. A strong correspondence is observed for most brain regions. In contrast, some discrepancies emerge in the language, frontal, and mid-frontal areas, where PET values are slightly higher than those predicted by the simulation. This divergence could indicate a more advanced local accumulation of protein plaques in these areas than expected. A possible explanation could be a higher rate of propagation of the β-amyloid protein than tau in this particular patient.

Zones	Patient 3 values	Simulation values	Reference times (years)
Entorhinal zone	2.44	2.443	26
Temporal zone	3	2.996	26
Hippocampal zone	2.95	2.932	26
Sensorial zone	2.98	2.980	25.5
Occipital zone	2.91	2.912	25
Language zone	3	2.990	26
Frontal zone	2.97	2.953	26
Zone of the wedge	1.99	2.008	27
Mid-frontal zone	3	2.964	27
Parietal zone	1.89	1.936	27
Central zone	2.48	2.515	27
Upper-frontal zone	2.21	2.213	26
Cingulate zone	2.31	2.332	20

Table 7.4: Average concentrations of tau and β-amyloid proteins measured via the patient's PET scan, alongside the corresponding concentrations obtained from the simulation conducted with parameters $\alpha_{tau} = 0.9 \left[\frac{1}{\text{year}}\right]$, $\alpha_{\beta} = 0.9 \left[\frac{1}{\text{year}}\right]$, and $\gamma_{int} = 1.2 \left[\frac{1}{\text{year}}\right]$, as well as the respective reference times at which these simulated concentrations were recorded.

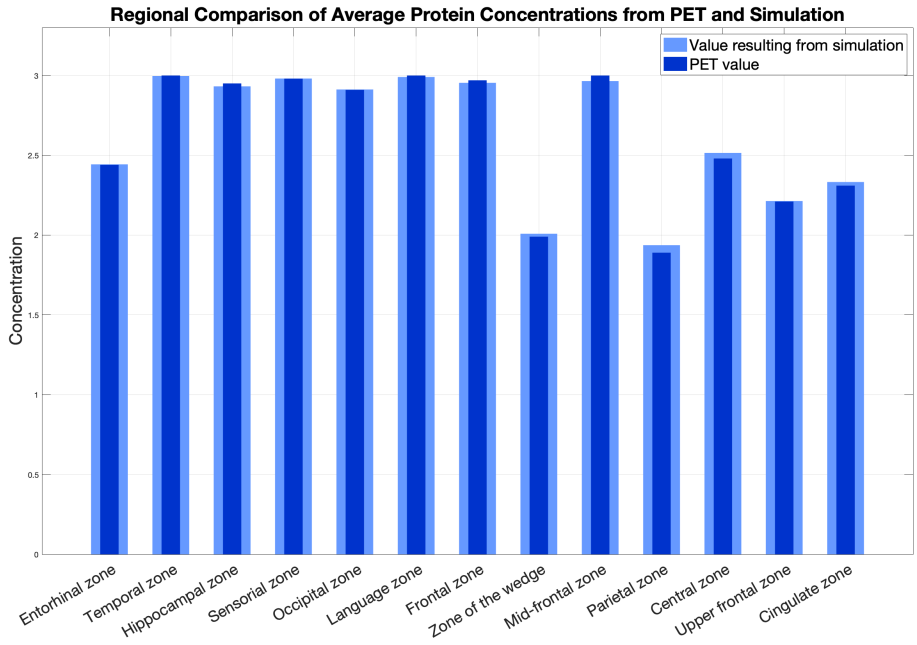

Figure 7.7: Comparison between the average concentrations obtained from the patient's PET scan (darker bars) and those computed by the simulation with parameters $\alpha_{tau} = 0.9 \left[\frac{1}{year}\right]$, $\alpha_{\beta} = 0.9 \left[\frac{1}{year}\right]$ and $\gamma_{int} = 1.2 \left[\frac{1}{year}\right]$ (lighter bars) for patient 3.

The sigmoidal curves representing the trend of the average protein accumulation in each brain region are now examined. The concentrations detected by PET were added to the graph as data points. It is evident that most of these points lie around the 26 year, with the exception of the cingulate region, which appears slightly earlier along the timeline.

This last observation is particularly relevant, as it confirms the model's ability to accurately interpret the data: the cingulate and upper-frontal regions should indeed be among the last to be affected by the spread of the pathological protein. However, one might wonder why the cingulate area is estimated to be affected before the superior frontal region.

One possible explanation lies in its location and geometric conformation: the cingulate cortex is spatially closer to the frontal area, identified as the origin of the β-amyloid protein epidemic, and much smaller than the superior frontal area, so it is completely invaded first by the spreading protein.

Furthermore, the sigmoid curve describing the concentration trend in the cingulate area shows a strong initial increase followed by a longer accumulation plateau. This trend suggests that in the cingulate cortex, the clinical manifestations of the disease may become more evident during this latent accumulation phase, when plaque accumulation reaches a critical threshold.

As also shown in the histogram of figure 7.7, most brain regions have already been significantly invaded by the misfolded proteins. All PET-based data points are located in the ascending end of the sigmoid curves, suggesting that the pathological process is firmly established within the cortex.

Given this clinical picture, it is likely that the patient will experience progressive cognitive decline over the next few years, resulting in deteriorating neurological function.

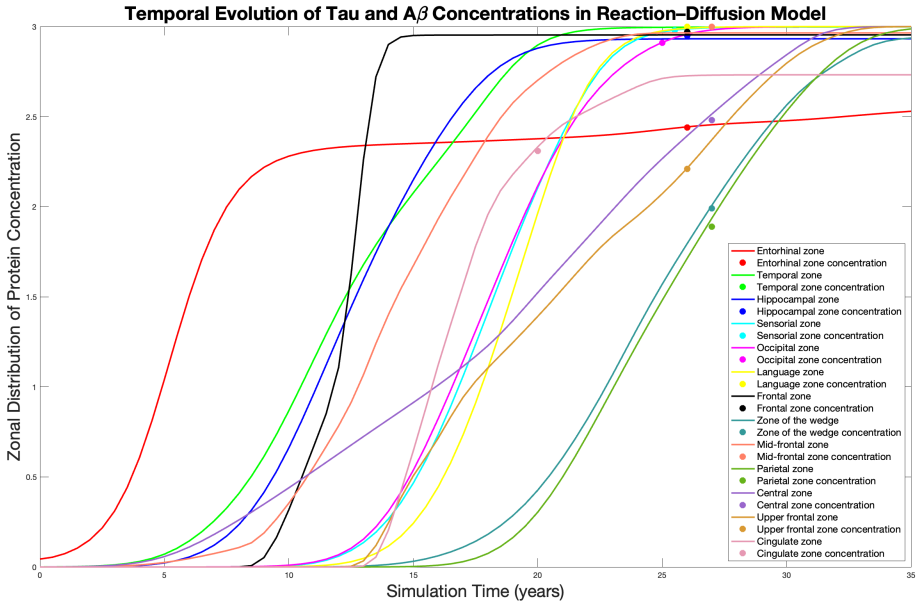

Figure 7.8: Trend of mean concentrations of tau and β-amyloid proteins in the simulation with parameters $\alpha_{tau} = 0.9\left[\frac{1}{year}\right]$, $\alpha_{\beta} = 0.9\left[\frac{1}{year}\right]$ and $\gamma_{int} = 1.2\left[\frac{1}{year}\right]$. The dots represent the average concentrations per zone calculated by PET for patient 3.

Finally, the correspondence between the simulation implemented in COMSOL Multiphysics and the patient's real data, also displayed in the software, is analysed. On the left, the simulation is shown at 312 months, i.e. 26 years, which corresponds to the average state of disease progression calculated for the patient. On the right, the distribution of pathological protein concentrations derived from the PET scan is displayed.

From the global view of the cerebral cortex, it can be seen that the invasion is almost complete, with the exception of a few regions such as the cingulate, upper-frontal, and the area of the wedge.

The frontal view reveals that the spread of misfolded proteins has already reached the temporal, occipital, language, and mid-frontal regions, while parts of the frontal, upper-frontal, and the wedge areas remain less affected. In fact, in the PET-based representation, these latter regions appear lighter in colour than the deep red tone, indicating that total saturation has not yet occurred.

At last, the internal view shows that the propagation of pathological proteins is approaching completion in the uppermost cortical regions, suggesting that cognitive functions associated with the frontal and superior cingulate areas are likely to be affected later. In years to come, this progression could lead to cognitive decline, resulting in a loss of self-awareness and the patient's ability to maintain emotional relationships.

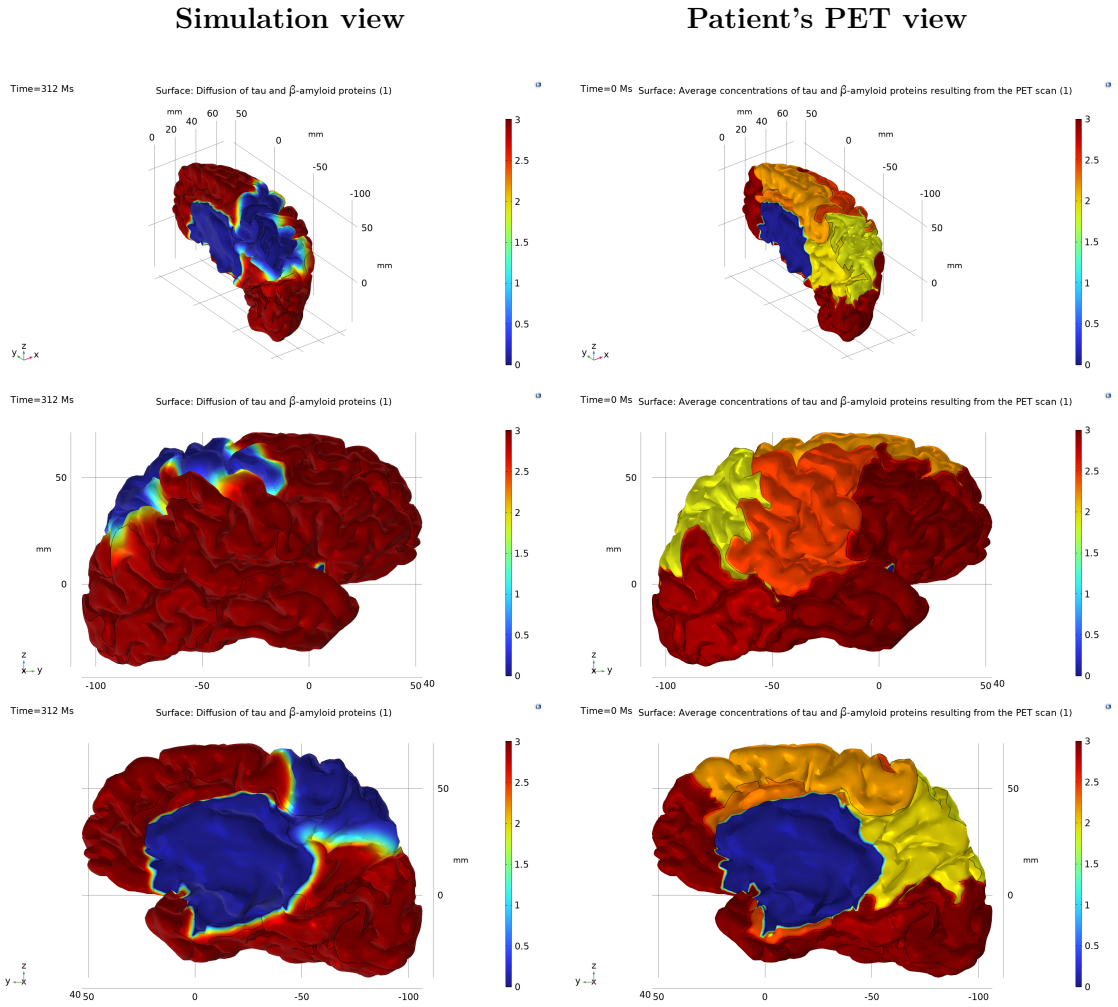

Figure 7.9: Comparison between the simulation with the parameters $\alpha_{tau} = 0.9 \left[\frac{1}{year}\right]$, $\alpha_{\beta} = 0.9 \left[\frac{1}{year}\right]$, $\gamma_{int} = 1.2 \left[\frac{1}{year}\right]$ and the real data for patient 3. Left: view of the cerebral cortex invasion trend at time 312 months. Right: view of the cerebral cortex with the values of the concentrations calculated by PET in the respective areas.

The same type of analysis was carried out for patient 4 (RID = 467). This patient is 91 years old and has an MMSE score of 19, indicating a condition of Moderate Cognitive Impairment. Generally, this score corresponds to an intermediate stage of the disease, where symptoms are more pronounced and personal autonomy is considerably compromised.

Typical symptoms associated with a MMSE of 19 include a marked deterioration of memory, with severe difficulty remembering recent events, a tendency to forget important personal information, and the occasional inability to recognise familiar or recently met people. The patient also shows considerable disorientation, sometimes getting lost even in familiar surroundings. Language and communication may be compromised, with difficulty expressing thoughts or engaging in basic conversations. Daily functioning is also affected, with difficulty in performing routine tasks such as preparing meals or using the telephone. From a psychological point of view, the patient may present with humour disorders such as irritability, anxiety, depression, mood swings, and reduced social inhibition. In some cases, mild psychotic symptoms such as suspiciousness or paranoia may also emerge.

The table 7.5 shows the values obtained from the patient's PET scan, together with the corresponding results of the computational simulation. The average time of disease progression in which the patient was placed is approximately 31 years from the onset of misfolded protein propagation. In fact, almost all of the simulated protein concentration values approach the critical threshold of 3, with the exception of the entorhinal and cingulate regions, which present slightly lower values. The latter, in agreement with both previous analyses and model predictions, is among the last areas to be affected by disease progression and plaque accumulation. In this case, the cortex invasion is almost complete, which corresponds to the severity of the patient's clinical symptoms.

Zones	Patient 4 values	Simulation values	Reference times (years)
Entorhinal zone	2.61	2.529	35
Temporal zone	3	2.998	34.5
Hippocampal zone	3	2.932	34
Sensorial zone	3	2.998	32
Occipital zone	3	2.999	30.5
Language zone	3	2.999	29
Frontal zone	3	2.953	29.5
Zone of the wedge	2.9	2.899	33.5
Mid-frontal zone	2.92	2.931	23
Parietal zone	3	2.987	35
Central zone	3	2.996	33
Upper-frontal zone	3	2.998	34
Cingulate zone	2.44	2.455	21

Table 7.5: Average concentrations of tau and β-amyloid proteins measured via the patient's PET scan, alongside the corresponding concentrations obtained from the simulation conducted with parameters $\alpha_{tau} = 0.9 \left[\frac{1}{\text{year}}\right]$, $\alpha_{\beta} = 0.9 \left[\frac{1}{\text{year}}\right]$, and $\gamma_{int} = 1.2 \left[\frac{1}{\text{year}}\right]$, as well as the respective reference times at which these simulated concentrations were recorded.

As shown in the histogram in figure 7.10, the protein concentrations measured by PET correspond closely to those obtained from the COMSOL simulation in most cortical regions.

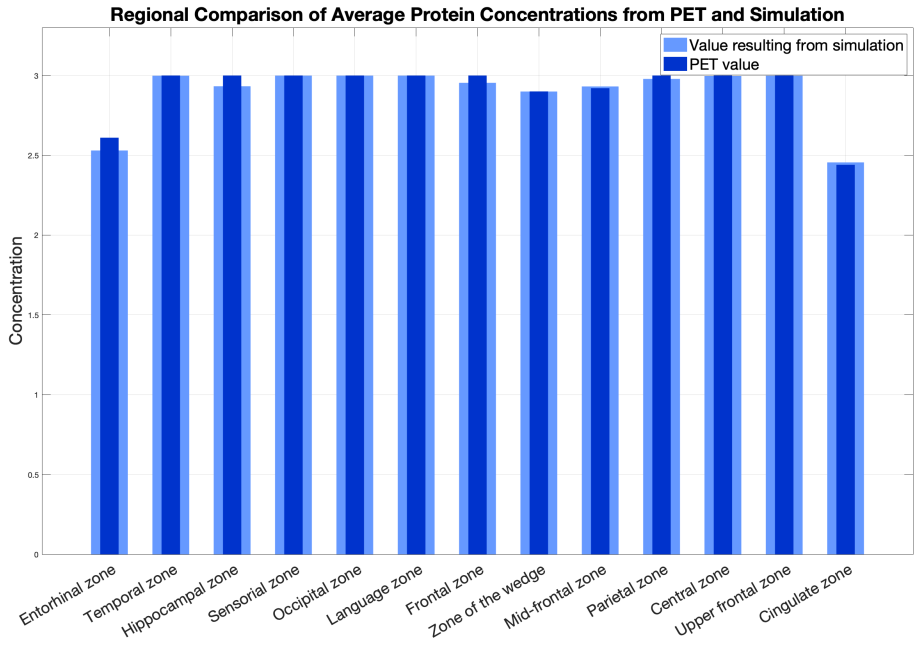

Figure 7.10: Comparison between the average concentrations obtained from the patient's PET scan (darker bars) and those computed by the simulation with parameters $\alpha_{tau} = 0.9\left[\frac{1}{year}\right]$, $\alpha_{\beta} = 0.9\left[\frac{1}{year}\right]$ and $\gamma_{int} = 1.2\left[\frac{1}{year}\right]$ (lighter bars) for patient 4.

Once again, trends in mean protein concentrations are examined through the sigmoid curves shown in figure 7.11. It can be observed that the markers representing the values obtained from the PET scan are all grouped on the right side of the curves: an indication that, in almost all cortical regions, the concentrations of pathological proteins have approached a state of full or almost complete saturation.

These PET-derived values are located within a time span of 29 to 35 years, which includes the model's estimated average disease time of 31 years since the start of propagation. This close correspondence between the simulation and the empirical data reinforces the reliability of the model in capturing the temporal dynamics of protein diffusion and plaque formation.

In particular, the consistent positioning of all regional values within the saturated phase of the sigmoids implies that the functional capacity of the affected brain areas can be severely impaired. This aligns well with the patient's clinical picture, which shows significant cognitive and functional impairment. The convergence of simulated and clinical data at an advanced stage of disease progression provides further validation of the predictive capability of the model.

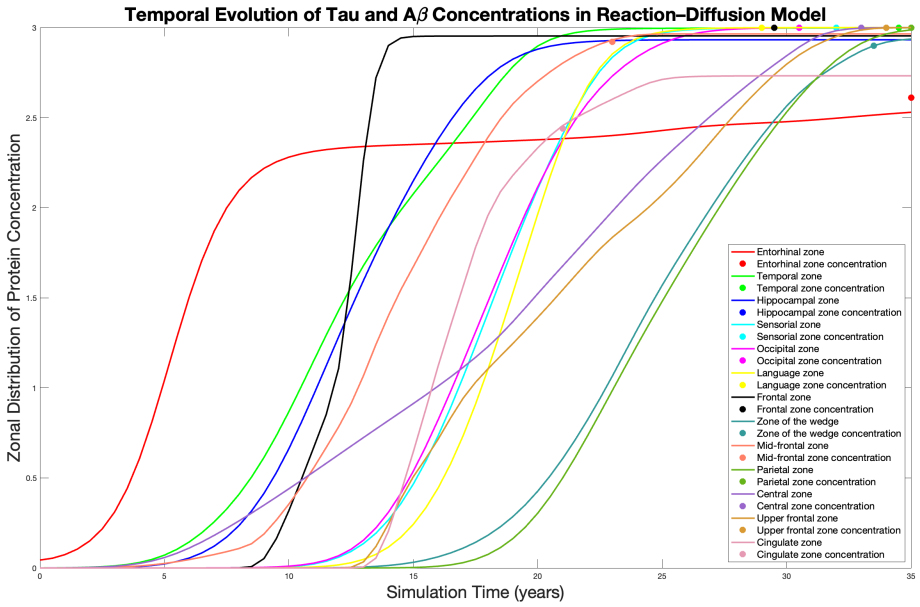

Figure 7.11: Trend of mean concentrations of tau and β-amyloid proteins in the simulation with parameters $\alpha_{tau} = 0.9\left[\frac{1}{year}\right]$, $\alpha_{\beta} = 0.9\left[\frac{1}{year}\right]$ and $\gamma_{int} = 1.2\left[\frac{1}{year}\right]$. The dots represent the average concentrations per zone calculated by PET for patient 4.

Finally, the comparison between the simulation data processed in COMSOL Multiphysics and the real PET-derived data is analysed.

It is immediately evident that, at the time of 372 months (31 years), the invasion of the cerebral cortex is almost complete. In the global cortical view, the only regions not yet completely invaded are small areas located between the zone of the wedge and the upper-frontal region. In the PET-based representation of the patient, these areas still show lighter red hues, indicating that full saturation of pathological proteins has not yet occurred. Since the PET data reflect average protein concentrations across regions, it is not possible to directly observe partially invaded sub-areas. Therefore, as in previous cases, a proper comparison between simulation and PET values requires interpreting the simulated spatial data in an averaged form.

The external and inner views of the cortex confirm that nearly all areas are affected by the propagation of misfolded proteins, consistent with the expected advanced stage of the disease. Over time, this widespread diffusion leads to extensive plaque accumulation and progressive neurodegeneration.

As also observed in patients 1, 2 and 3, the internal region of the brain remains unchanged by the reaction-diffusion dynamics of tau and beta-amyloid proteins. This is due to the anatomical composition of the inner zone, which consists mainly of white matter that is not directly involved in the cortical spreading mechanisms of Alzheimer's disease.

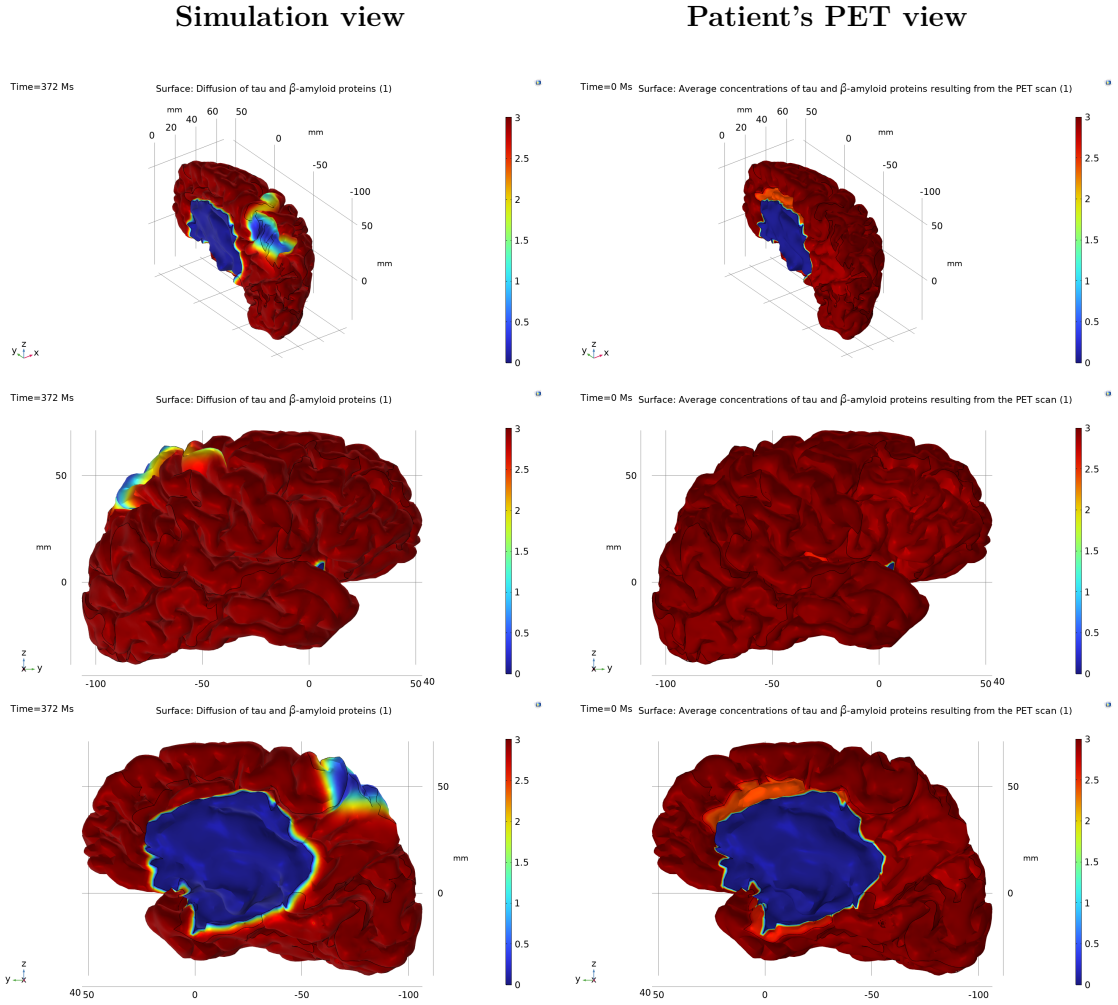

Figure 7.12: Comparison between the simulation with the parameters $\alpha_{tau} = 0.9 \left[\frac{1}{year}\right]$, $\alpha_{\beta} = 0.9 \left[\frac{1}{year}\right]$, $\gamma_{int} = 1.2 \left[\frac{1}{year}\right]$ and the real data for patient 4. Left: view of the cerebral cortex invasion trend at time 372 months. Right: view of the cerebral cortex with the values of the concentrations calculated by PET in the respective areas.

7.4 Parametric study

The simulation performed using the parameters $\alpha_{tau} = 0.9 \left[\frac{1}{\text{year}}\right]$, $\alpha_{\beta} = 0.9 \left[\frac{1}{\text{year}}\right]$, and $\gamma_{int} = 1.2 \left[\frac{1}{\text{year}}\right]$ has proven capable of accurately interpreting the data of the patient cohort. To ensure the flexibility and adaptability of the constructed model, a parametric study based on additional simulations is now presented.

Given the variability in biological conditions for each patient at the time of diagnosis — particularly in terms of propagation dynamics and the misfolding rates of pathological proteins — a parametric analysis is essential to ensure the model's flexibility and generalizability. The aim of the following analysis is to investigate how variations in the parameters α_{tau}, α_{β}, and γ_{int} influence the estimated progression timeline of the disease within the same patient cohort. In particular, by fixing the interaction parameter at $\gamma_{int} = 1.5 \left[\frac{1}{\text{year}}\right]$, a parametric study is performed on α_{tau} and α_{β}, while the initial concentrations of tau and β-amyloid proteins are kept constant at 0.05.

7.4.1 Case $\alpha_{tau} = \alpha_{\beta}$

The following simulation was performed with parameters set to $\alpha_{tau} = 1.5 \left[\frac{1}{\text{year}}\right]$, $\alpha_{\beta} = 1.5 \left[\frac{1}{\text{year}}\right]$, and $\gamma_{int} = 1.5 \left[\frac{1}{\text{year}}\right]$.

Compared to the previous simulation, all parameters have higher values, which should result in shorter invasion times and a faster progression of the disease. This is actually observed: under these conditions, the accumulation of misfolded proteins throughout the cerebral cortex occurs in approximately 26 years.

For patient 1 (RID = 31), table 7.6 shows the comparison between the average protein concentrations obtained from the PET scan and those computed from the simulation, along with the corresponding reference times. In this case, the estimated average invasion time is approximately 5.7 years. Compared to the first simulation, this result places the patient at an earlier stage of cortical invasion.

The same procedure was applied to patient 2 (RID = 800), for whom an average estimated placement time of approximately 10 years was observed. Once again, the disease progression time is shorter than that obtained in the initial simulation.

For patient 3 (RID = 1190), the estimated average time is approximately 17 years, highlighting a significant discrepancy of about 9 years when compared to the earlier simulation — an indication of a notable acceleration in disease progression under the new parameter set.

Finally, for patient 4 (RID = 467), an average progression time of 25 years was calculated. In this case, the time difference compared to the previous simulation, with parameters $\alpha_{tau} = 0.9 \left[\frac{1}{\text{year}}\right]$, $\alpha_{\beta} = 0.9 \left[\frac{1}{\text{year}}\right]$, and $\gamma_{int} = 1.2 \left[\frac{1}{\text{year}}\right]$, is approximately 6 years.

The values reported in tables 7.6, 7.7, 7.8, and 7.9 correspond, respectively, to the average protein concentrations measured by PET scan, those computed through the simulation, and the estimated times at which such concentrations are reached for each patient.

Zones	Patient 1 values	Simulation values	Reference times (years)
Entorhinal zone	0.61	0.495	2
Temporal zone	0.07	0.061	3
Hippocampal zone	0.01	0.018	3
Sensorial zone	0.005	0.006	7
Occipital zone	0.003	0.003	6
Language zone	0.0007	0.00068	6.5
Frontal zone	0.003	0.0015	6
Zone of the wedge	0.0002	0.00019	7.5
Mid-frontal zone	0.02	0.020	3
Parietal zone	0.0001	0.0002	9.5
Central zone	0.04	0.047	3
Upper-frontal zone	0.003	0.001	9.5
Cingulate zone	0.001	0.002	10

Table 7.6: Average concentrations of tau and β-amyloid proteins measured via the patient's PET scan, alongside the corresponding concentrations obtained from the simulation conducted with parameters $\alpha_{tau} = 1.5 \left[\frac{1}{\text{year}}\right]$, $\alpha_{\beta} = 1.5 \left[\frac{1}{\text{year}}\right]$, and $\gamma_{int} = 1.5 \left[\frac{1}{\text{year}}\right]$, as well as the respective reference times at which these simulated concentrations were recorded.

Zones	Patient 2 values	Simulation values	Reference times (years)
Entorhinal zone	2.35	2.315	5
Temporal zone	2.21	2.194	11
Hippocampal zone	2.44	2.389	11
Sensorial zone	0.52	0.601	11
Occipital zone	0.77	0.729	10.5
Language zone	0.45	0.452	11
Frontal zone	2.12	2.180	10
Zone of the wedge	0.007	0.008	9.5
Mid-frontal zone	2.12	2.079	12.5
Parietal zone	0.0001	0.0002	9.5
Central zone	0.45	0.455	7
Upper-frontal zone	0.43	0.444	11.5
Cingulate zone	1.12	1.120	12.5

Table 7.7: Average concentrations of tau and β-amyloid proteins measured via the patient's PET scan, alongside the corresponding concentrations obtained from the simulation conducted with parameters $\alpha_{tau} = 1.5 \left[\frac{1}{\text{year}}\right]$, $\alpha_{\beta} = 1.5 \left[\frac{1}{\text{year}}\right]$, and $\gamma_{int} = 1.5 \left[\frac{1}{\text{year}}\right]$, as well as the respective reference times at which these simulated concentrations were recorded.

Zones	Patient 3 values	Simulation values	Reference times (years)
Entorhinal zone	2.44	2.440	6.5
Temporal zone	3	2.994	16
Hippocampal zone	2.95	2.937	15
Sensorial zone	2.98	2.983	18
Occipital zone	2.91	2.902	17.5
Language zone	3	2.991	18
Frontal zone	2.97	2.961	15
Zone of the wedge	1.99	2.027	19.5
Mid-frontal zone	3	2.969	19.5
Parietal zone	1.89	1.877	19
Central zone	2.48	2.471	19.5
Upper-frontal zone	2.21	2.230	19.5
Cingulate zone	2.31	2.292	15

Table 7.8: Average concentrations of tau and β-amyloid proteins measured via the patient's PET scan, alongside the corresponding concentrations obtained from the simulation conducted with parameters $\alpha_{tau} = 1.5 \left[\frac{1}{\text{year}}\right]$, $\alpha_{\beta} = 1.5 \left[\frac{1}{\text{year}}\right]$, and $\gamma_{int} = 1.5 \left[\frac{1}{\text{year}}\right]$, as well as the respective reference times at which these simulated concentrations were recorded.

Zones	Patient 4 values	Simulation values	Reference times (years)
Entorhinal zone	2.61	2.612	25.5
Temporal zone	3	2.999	25.5
Hippocampal zone	3	2.948	26.5
Sensorial zone	3	2.999	24
Occipital zone	3	2.999	23.5
Language zone	3	2.999	24
Frontal zone	3	2.961	25
Zone of the wedge	2.9	2.919	24.5
Mid-frontal zone	2.92	2.928	17
Parietal zone	3	2.999	26
Central zone	3	2.996	24.5
Upper-frontal zone	3	2.999	25
Cingulate zone	2.44	2.414	15.5

Table 7.9: Average concentrations of tau and β-amyloid proteins measured via the patient's PET scan, alongside the corresponding concentrations obtained from the simulation conducted with parameters $\alpha_{tau} = 1.5 \left[\frac{1}{\text{year}}\right]$, $\alpha_{\beta} = 1.5 \left[\frac{1}{\text{year}}\right]$, and $\gamma_{int} = 1.5 \left[\frac{1}{\text{year}}\right]$, as well as the respective reference times at which these simulated concentrations were recorded.

Let us now examine the comparison between the distribution of average concentrations obtained from the simulation and those derived from PET imaging, as shown in the histograms in figure 7.13 and the sigmoidal plots in figure 7.14 for patients 1, 2, 3, and 4.

The histograms indicate that the average concentrations computed using the simulation with parameters $\alpha_{tau} = 1.5\left[\frac{1}{\text{year}}\right]$, $\alpha_{\beta} = 1.5\left[\frac{1}{\text{year}}\right]$, and $\gamma_{int} = 1.5\left[\frac{1}{\text{year}}\right]$ are generally consistent with those measured via PET. Slight discrepancies observed in specific regions for patients 1 and 2 may be attributed to the time discretization of the simulation, which was carried out at six-month intervals. It is likely that a finer temporal resolution would yield an even closer correspondence.

The sigmoidal plots further support these findings. For patient 1, the PET-derived concentration points are concentrated within the first 10 years of the simulation, in agreement with the estimated average time. In patient 2, the points are clustered around the period in which pathological proteins begin to propagate extensively across the cortex, starting from the entorhinal region. This is reflected by the fact that the PET value for the entorhinal cortex is located near the peak of its corresponding sigmoid, indicating advanced invasion in that region. In patient 3, most PET-derived values fall within the range of 16 to 20 years, corresponding to the phase during which the cortical regions located at the top of the brain are progressively invaded. Finally, for the patient 4, most of the values are placed on the sigmoid plateau, indicating an almost complete saturation of the protein accumulation in the cortical cortex, consistent with an already advanced and diffuse pathological state.

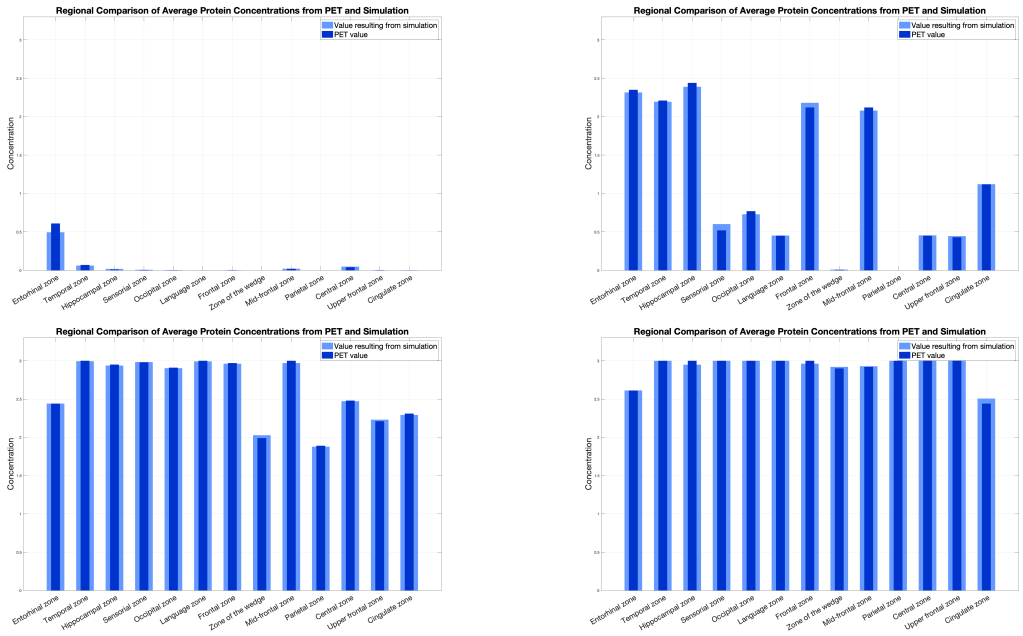

Figure 7.13: Comparison between the average concentrations obtained from the patient's PET scan (darker bars) and those computed by the simulation with parameters $\alpha_{tau} = 1.5\left[\frac{1}{year}\right]$, $\alpha_{\beta} = 1.5\left[\frac{1}{year}\right]$ and $\gamma_{int} = 1.5\left[\frac{1}{year}\right]$ (lighter bars) for patient 1, 2, 3 and 4, respectively.

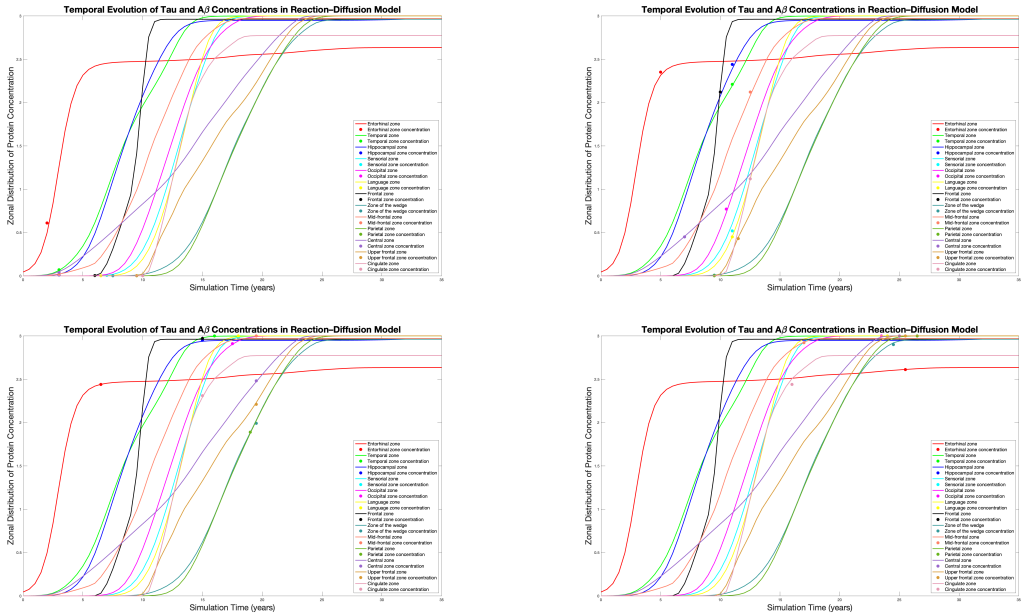

Figure 7.14: Trend of mean concentrations of tau and β-amyloid proteins in the simulation with parameters $\alpha_{tau} = 1.5 \left[\frac{1}{year}\right]$, $\alpha_{\beta} = 1.5 \left[\frac{1}{year}\right]$ and $\gamma_{int} = 1.5 \left[\frac{1}{year}\right]$. The dots represent the average concentrations per zone calculated by PET for patient 1, 2, 3 and 4, respectively.

Finally, the simulation results at the four mean time points corresponding to the clinical placement of each patient in the study are analysed.

For patient 1, the estimated mean time since the onset of pathological protein propagation is approximately 5.7 years. Accordingly, the simulation output at 66 months is shown in figure 7.15.

Compared to the PET-derived data, the simulation appears to overestimate the accumulation of pathological proteins in the entorhinal cortex, suggesting a more advanced stage of local invasion than is actually observed. Despite this discrepancy, the simulation correctly captures the subsequent spread of proteins to adjacent regions, particularly the temporal cortex through the connectome structure, as visible in the external view of the simulated brain. In all other cortical areas, the concentrations obtained from the simulation show good agreement with those measured by PET.

This suggests that, in the case of the patient 1, the estimated mean disease progression time of 5.5 years may be slightly higher than the patient's actual clinical stage.

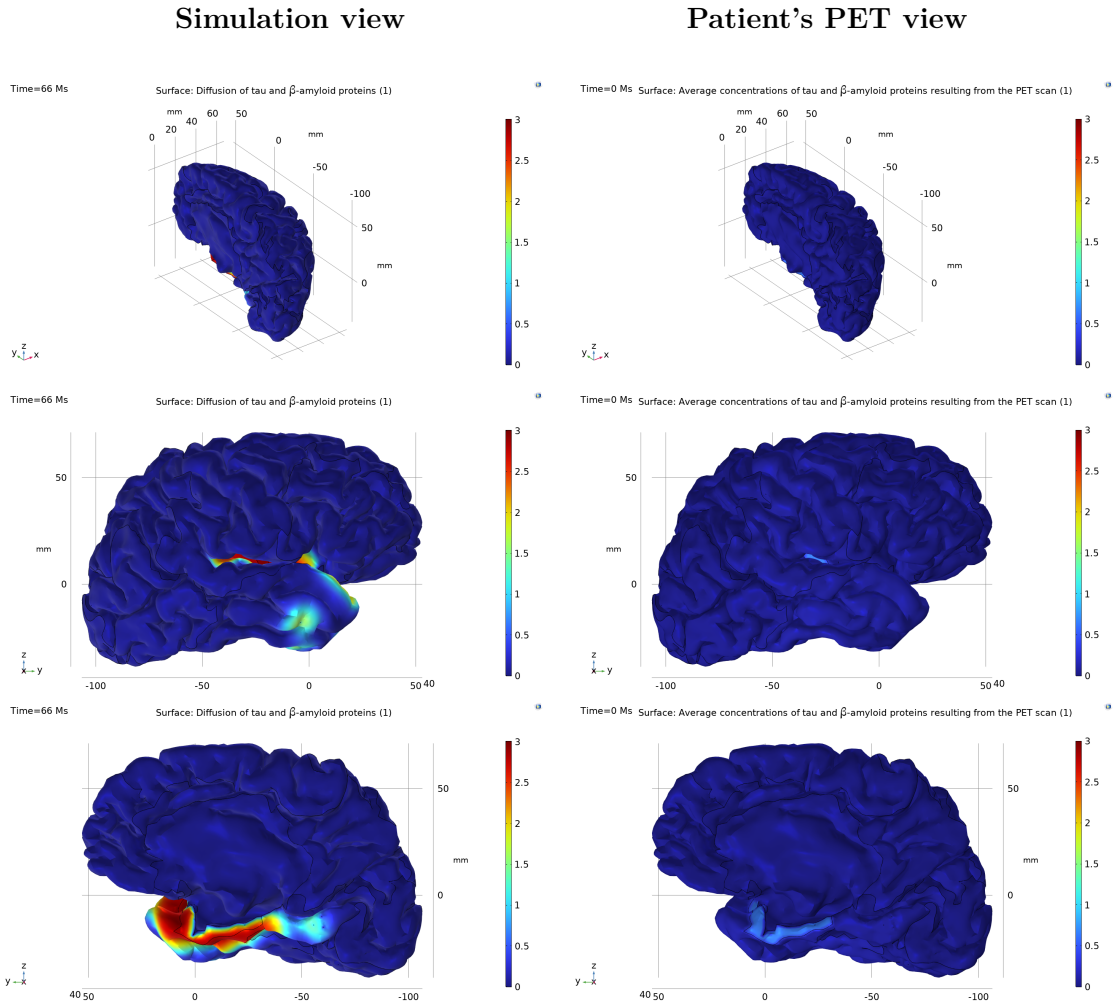

Figure 7.15: Comparison between the simulation with the parameters $\alpha_{tau} = 1.5 \left[\frac{1}{year}\right]$, $\alpha_{\beta} = 1.5 \left[\frac{1}{year}\right]$, $\gamma_{int} = 1.5 \left[\frac{1}{year}\right]$ and the real data for patient 1. Left: view of the cerebral cortex invasion trend at time 66 months. Right: view of the cerebral cortex with the values of the concentrations calculated by PET in the respective areas.

In the case of patient 2, the comparison between the PET scan results (shown on the right) and the simulation output at 120 months (shown on the left) is encouraging.

The PET images highlight regions with higher average protein concentrations through red and orange hues. Correspondingly, the simulation results indicate that these same regions were the initial targets for the propagation of misfolded proteins and plaque accumulation. Conversely, areas depicted in blue in both the PET scan and the simulation correspond to regions where cognitive functions are still largely preserved.

Simulation view **Patient's PET view**

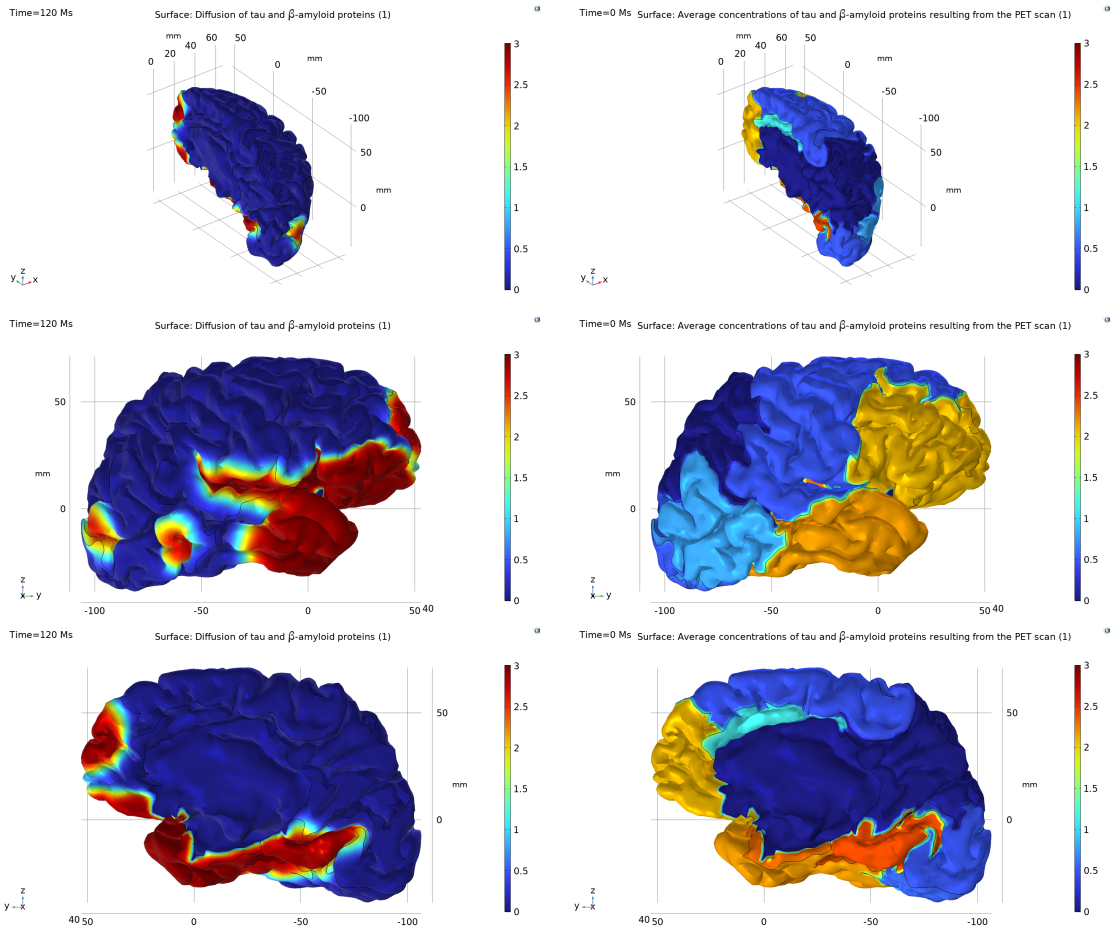

Figure 7.16: Comparison between the simulation with the parameters $\alpha_{tau} = 1.5\left[\frac{1}{year}\right]$, $\alpha_{\beta} = 1.5\left[\frac{1}{year}\right]$, $\gamma_{int} = 1.5\left[\frac{1}{year}\right]$ and the real data for patient 2. Left: view of the cerebral cortex invasion trend at time 120 months. Right: view of the cerebral cortex with the values of the concentrations calculated by PET in the respective areas.

In the case of patient 3, it is observed that the majority of brain regions are affected by a widespread presence of tau and β-amyloid proteins, indicating that the disease is progressively involving nearly all areas of the brain.

The protein concentrations measured by the PET scan show a good agreement with the simulation results captured at 198 months (i.e. 16.5 years). Regions appearing in lighter colors — such as yellow, orange, and light red — correspond to areas that the simulation indicates have not yet been fully invaded by the pathology. This correspondence suggests that these areas are likely to be the last to experience cognitive decline and, as the simulation further demonstrates, the last to be affected by plaque accumulation.

Simulation view **Patient's PET view**

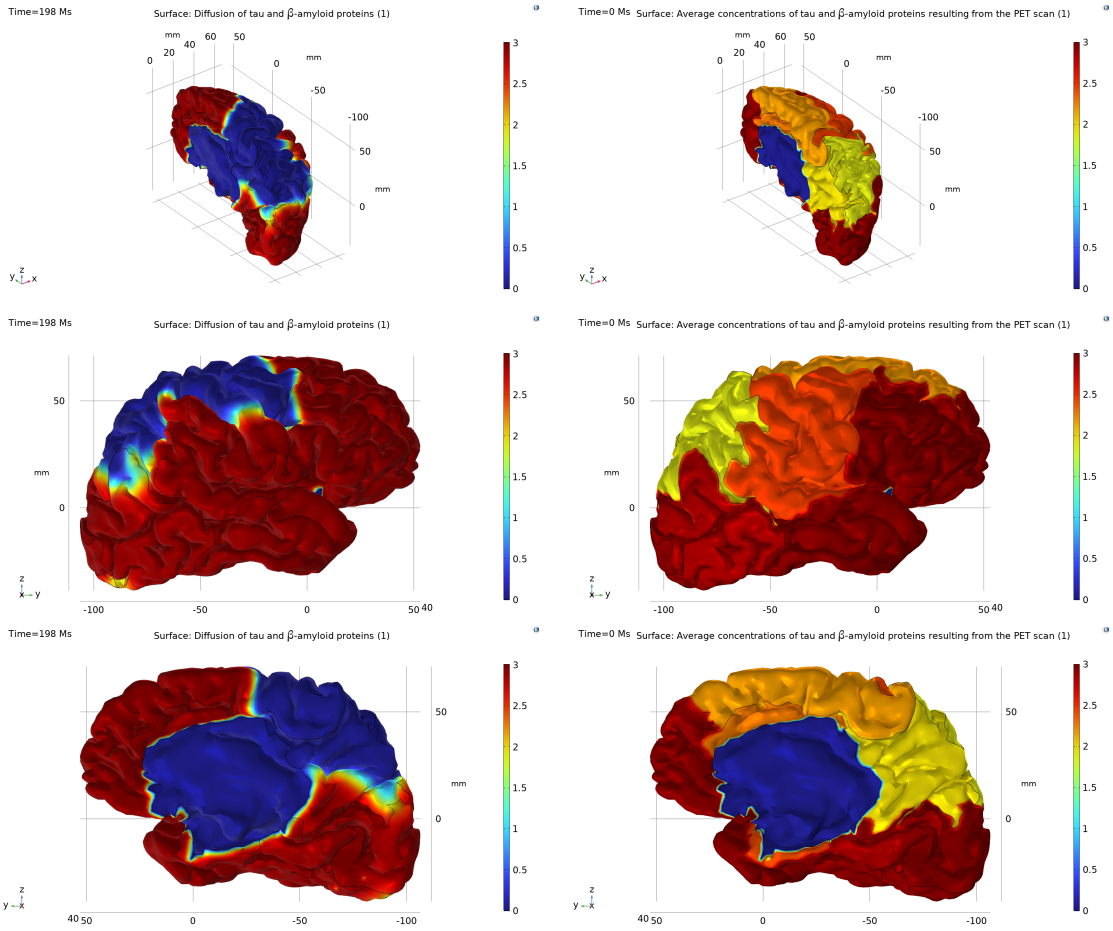

Figure 7.17: Comparison between the simulation with the parameters $\alpha_{tau} = 1.5\left[\frac{1}{year}\right]$, $\alpha_{\beta} = 1.5\left[\frac{1}{year}\right]$, $\gamma_{int} = 1.5\left[\frac{1}{year}\right]$ and the real data for patient 3. Left: view of the cerebral cortex invasion trend at time 198 months. Right: view of the cerebral cortex with the values of the concentrations calculated by PET in the respective areas.

Ultimately, in the case of patient 4, the simulation shown on the left side of figure 7.18 indicates that the invasion of the cerebral cortex is nearly complete, with all areas affected by the accumulation of misfolded proteins. This is well reflected on the right side of the figure, which displays the PET scan results. Both the simulation performed with parameters $\alpha_{tau} = 0.9 \left[\frac{1}{year}\right]$, $\alpha_{\beta} = 0.9 \left[\frac{1}{year}\right]$, $\gamma_{int} = 1.2 \left[\frac{1}{year}\right]$ and the current simulation place the patient in an advanced stage of the disease, characterized by ongoing cognitive decline.

The primary difference between the two simulations consists in the estimated average time of cortical invasion: approximately 31 years in the first simulation, compared to about 25 years in the second. This reduction in estimated time correlates with the increased parameter values, indicating a faster disease progression and an earlier placement of the patient along the disease timeline.

This observation suggests that the simulation with parameters $\alpha_{tau} = 1.5 \left[\frac{1}{year}\right]$, $\alpha_{\beta} = 1.5 \left[\frac{1}{year}\right]$, and $\gamma_{int} = 1.5 \left[\frac{1}{year}\right]$ may more accurately represent the patient's condition, positioning them around 25 years from the initial appearance of misfolded tau protein in the entorhinal region. The subsequent years are characterized by continued cognitive decline and neurodegeneration, during which the average concentration of misfolded proteins stabilizes upon reaching the threshold value of 3, while plaque formation continues.

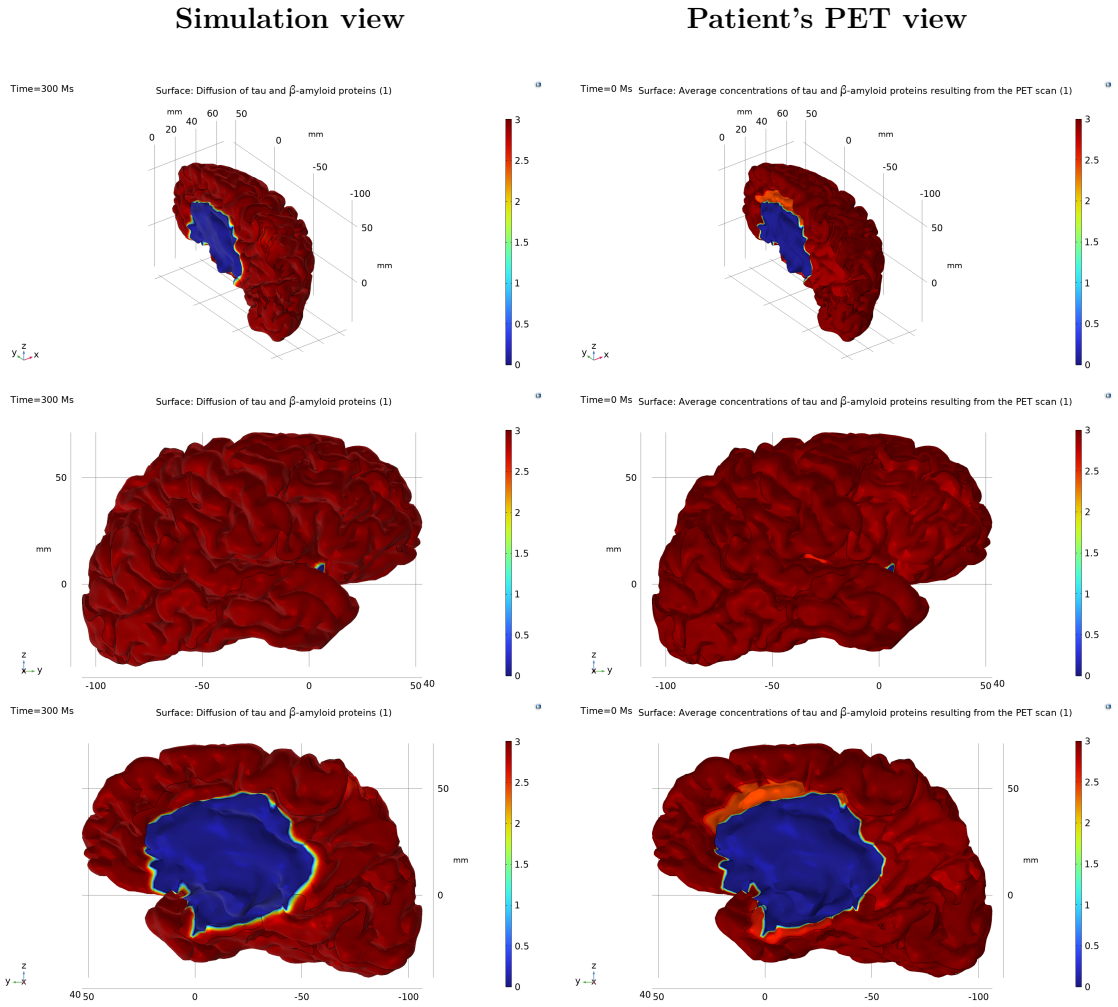

Figure 7.18: Comparison between the simulation with the parameters $\alpha_{tau} = 1.5 \left[\frac{1}{year}\right]$, $\alpha_{\beta} = 1.5 \left[\frac{1}{year}\right]$, $\gamma_{int} = 1.5 \left[\frac{1}{year}\right]$ and the real data for patient 4. Left: view of the cerebral cortex invasion trend at time 300 months. Right: view of the cerebral cortex with the values of the concentrations calculated by PET in the respective areas.

7.4.2 Case $\alpha_{tau} > \alpha_{\beta}$

In this section, the case in which the parameter α_{tau} is greater than α_{β} is analyzed. The assigned values are $\alpha_{tau} = 1.7 \left[\frac{1}{\text{year}}\right]$ and $\alpha_{\beta} = 1.1 \left[\frac{1}{\text{year}}\right]$, thus assuming a faster conversion rate from healthy to misfolded proteins for tau compared to β-amyloid.

For patient 1 (RID = 31), the calculated mean cerebral cortex invasion time is 5.52 years, confirming an early stage of the disease in which no acute symptoms are present. This is evident in the first histogram of figure 7.19 and the first concentration graph in figure 7.20, where only the entorhinal zone shows a significant protein concentration different from zero.

Patient 2 (RID = 800) has an estimated mean invasion time of approximately 9.61 years, consistent with previous simulations placing the patient in a mildly symptomatic stage. As shown in the second histogram of figure 7.19 and the corresponding sigmoid graph in figure 7.20, almost all brain areas exhibit non-zero protein concentrations concentrated within the first 10 years of the simulation, indicating the early spread of the disease across the cerebral cortex.

For patient 3 (RID = 1190), the average invasion time is 16.26 years, reflecting disseminated disease presence and initial protein accumulation in most brain regions. This timing aligns with the appearance of noticeable clinical symptoms during testing. The third histogram in figure 7.19 illustrates the correspondence between simulated and PET-derived values over time, while the third sigmoid graph in figure 7.20 shows PET concentration dots clustered after approximately 15 years from disease onset.

Finally, patient 4 (RID = 467) presents a mean invasion time of 22.84 years, indicating advanced disease progression. This patient already exhibits symptoms consistent with a deteriorating condition. The last histogram in figure 7.19 and the fourth concentration trend graph in figure 7.20 reveal that PET values correspond to a near-total cerebral invasion with plaque formation.

Tables 7.10, 7.11, 7.12, and 7.13 report the PET values, simulation results, and corresponding reference times for each patient. Comparative histograms between calculated and PET concentrations for each patient are shown in figure 7.19, alongside the average concentration trends per brain region in figure 7.20.

Lastly, the simulation results at the average times — 66 months for patient 1, 114 months for patient 2, 192 months for patient 3, and 276 months for patient 4 — are presented and compared with the corresponding PET data in figures 7.21, 7.22, 7.23, and 7.24.

Zones	Patient 1 values	Simulation values	Reference times (years)
Entorhinal zone	0.61	0.69	2
Temporal zone	0.07	0.093	3
Hippocampal zone	0.01	0.013	2.5
Sensorial zone	0.005	0.0025	6
Occipital zone	0.003	0.003	5.5
Language zone	0.0007	0.0007	6
Frontal zone	0.003	0.0061	6.5
Zone of the wedge	0.0002	0.0002	7
Mid-frontal zone	0.02	0.016	2.5
Parietal zone	0.0001	0.0001	8.5
Central zone	0.04	0.036	2.5
Upper-frontal zone	0.003	0.0006	9.5
Cingulate zone	0.001	0.001	10

Table 7.10: Average concentrations of tau and β-amyloid proteins measured via the patient's PET scan, alongside the corresponding concentrations obtained from the simulation conducted with parameters $\alpha_{tau} = 1.7 \left[\frac{1}{\text{year}}\right]$, $\alpha_{\beta} = 1.1 \left[\frac{1}{\text{year}}\right]$, and $\gamma_{int} = 1.5 \left[\frac{1}{\text{year}}\right]$, as well as the respective reference times at which these simulated concentrations were recorded.

Zones	Patient 2 values	Simulation values	Reference times (years)
Entorhinal zone	2.35	2.365	4.5
Temporal zone	2.21	2.167	10
Hippocampal zone	2.44	2.518	10.5
Sensorial zone	0.52	0.552	10
Occipital zone	0.77	0.712	9.5
Language zone	0.45	0.434	10
Frontal zone	2.12	2.081	10
Zone of the wedge	0.007	0.0061	8.5
Mid-frontal zone	2.12	2.097	13
Parietal zone	0.0001	0.0001	8.5
Central zone	0.45	0.467	6.5
Upper-frontal zone	0.43	0.407	11.5
Cingulate zone	1.12	1.046	12.5

Table 7.11: Average concentrations of tau and β-amyloid proteins measured via the patient's PET scan, alongside the corresponding concentrations obtained from the simulation conducted with parameters $\alpha_{tau} = 1.7 \left[\frac{1}{\text{year}}\right]$, $\alpha_{\beta} = 1.1 \left[\frac{1}{\text{year}}\right]$, and $\gamma_{int} = 1.5 \left[\frac{1}{\text{year}}\right]$, as well as the respective reference times at which these simulated concentrations were recorded.

Zones	Patient 3 values	Simulation values	Reference times (years)
Entorhinal zone	2.44	2.458	5.5
Temporal zone	3	2.996	15
Hippocampal zone	2.95	2.950	15.5
Sensorial zone	2.98	2.981	16.5
Occipital zone	2.91	2.893	16
Language zone	3	2.999	18
Frontal zone	2.97	2.960	12.5
Zone of the wedge	1.99	2.063	18.5
Mid-frontal zone	3	2.968	20
Parietal zone	1.89	1.877	17.5
Central zone	2.48	2.454	19
Upper-frontal zone	2.21	2.263	21.5
Cingulate zone	2.31	2.290	16

Table 7.12: Average concentrations of tau and β-amyloid proteins measured via the patient's PET scan, alongside the corresponding concentrations obtained from the simulation conducted with parameters $\alpha_{tau} = 1.7 \left[\frac{1}{\text{year}}\right]$, $\alpha_{\beta} = 1.1 \left[\frac{1}{\text{year}}\right]$, and $\gamma_{int} = 1.5 \left[\frac{1}{\text{year}}\right]$, as well as the respective reference times at which these simulated concentrations were recorded.

Zones	Patient 4 values	Simulation values	Reference times (years)
Entorhinal zone	2.61	2.612	31
Temporal zone	3	2.999	28
Hippocampal zone	3	2.950	22
Sensorial zone	3	2.999	23
Occipital zone	3	2.999	20
Language zone	3	2.999	19.5
Frontal zone	3	2.961	20.5
Zone of the wedge	2.9	2.906	23
Mid-frontal zone	2.92	2.908	18
Parietal zone	3	2.999	24.5
Central zone	3	2.999	25
Upper-frontal zone	3	2.999	25.5
Cingulate zone	2.44	2.438	17

Table 7.13: Average concentrations of tau and β-amyloid proteins measured via the patient's PET scan, alongside the corresponding concentrations obtained from the simulation conducted with parameters $\alpha_{tau} = 1.7 \left[\frac{1}{\text{year}}\right]$, $\alpha_{\beta} = 1.1 \left[\frac{1}{\text{year}}\right]$, and $\gamma_{int} = 1.5 \left[\frac{1}{\text{year}}\right]$, as well as the respective reference times at which these simulated concentrations were recorded.

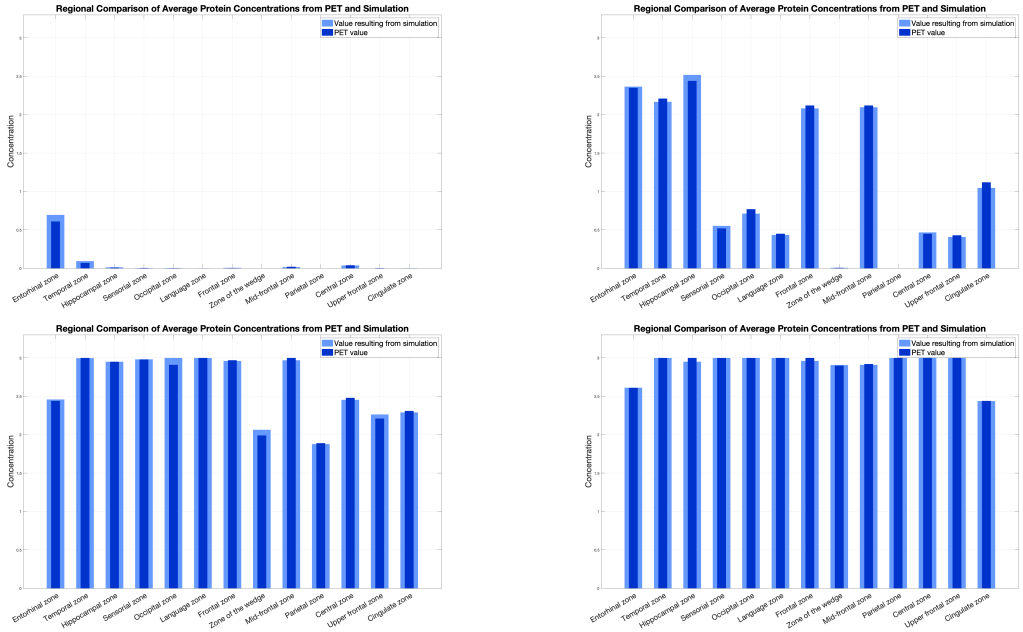

Figure 7.19: Comparison between the average concentrations obtained from the patient's PET scan (darker bars) and those computed by the simulation with parameters $\alpha_{tau} = 1.7\left[\frac{1}{year}\right]$, $\alpha_{\beta} = 1.1\left[\frac{1}{year}\right]$ and $\gamma_{int} = 1.5\left[\frac{1}{year}\right]$ (lighter bars) for patient 1, 2, 3 and 4, respectively.

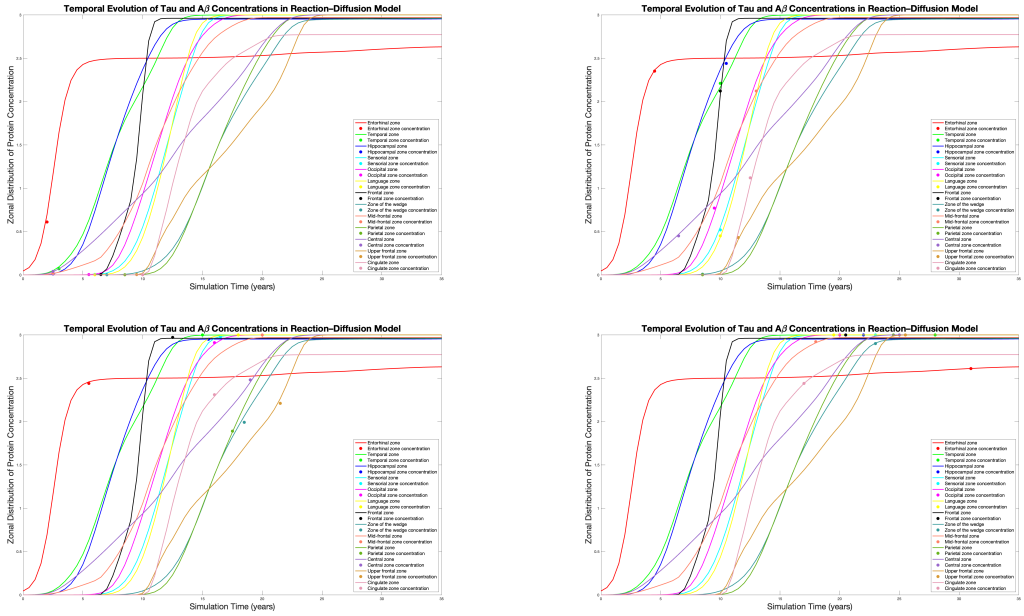

Figure 7.20: Trend of mean concentrations of tau and β-amyloid proteins in the simulation with parameters $\alpha_{tau} = 1.7\left[\frac{1}{year}\right]$, $\alpha_{\beta} = 1.1\left[\frac{1}{year}\right]$ and $\gamma_{int} = 1.5\left[\frac{1}{year}\right]$. The dots represent the average concentrations per zone calculated by PET for patient 1, 2, 3 and 4, respectively.

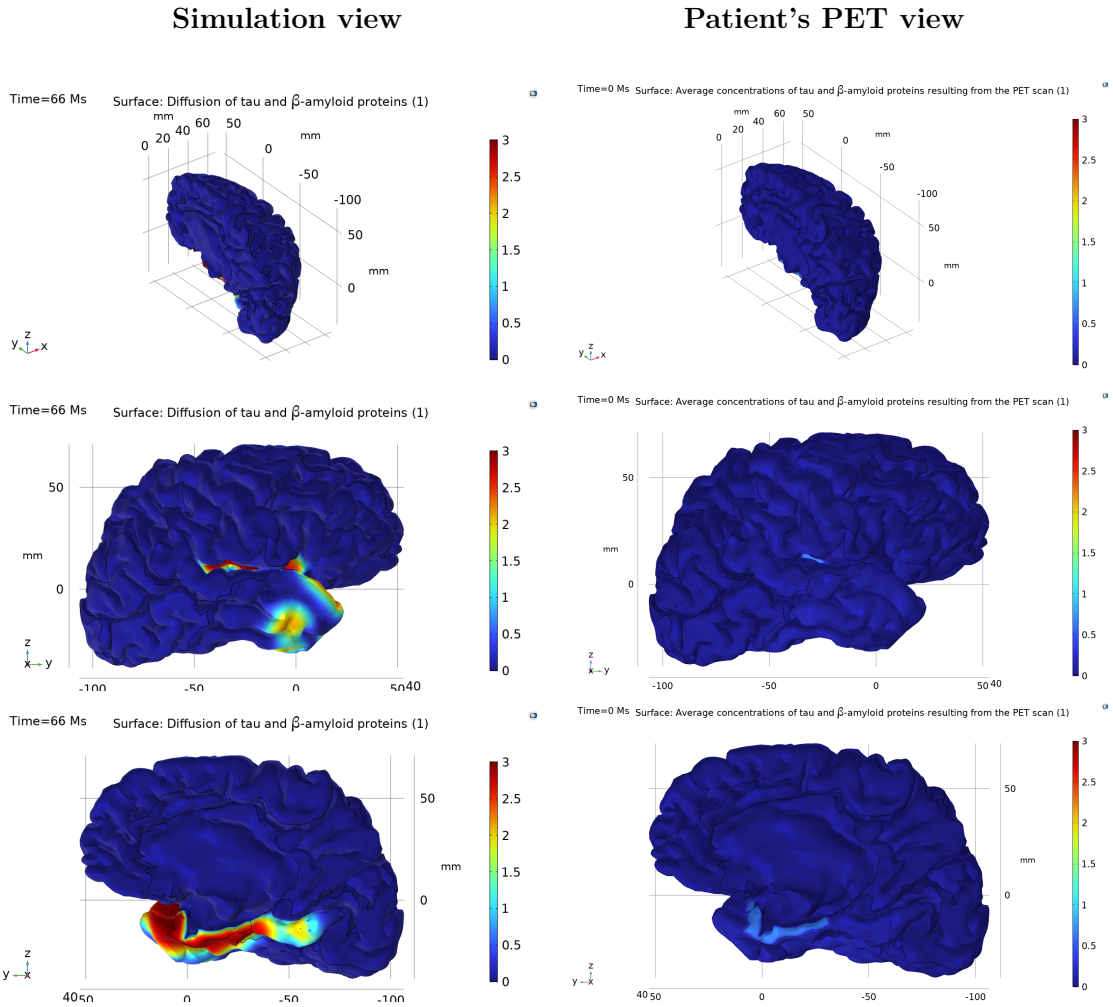

Figure 7.21: Comparison between the simulation with the parameters $\alpha_{tau} = 1.7 \left[\frac{1}{year}\right]$, $\alpha_{\beta} = 1.1 \left[\frac{1}{year}\right]$, $\gamma_{int} = 1.5 \left[\frac{1}{year}\right]$ and the real data for patient 1. Left: view of the cerebral cortex invasion trend at time 66 months. Right: view of the cerebral cortex with the values of the concentrations calculated by PET in the respective areas.

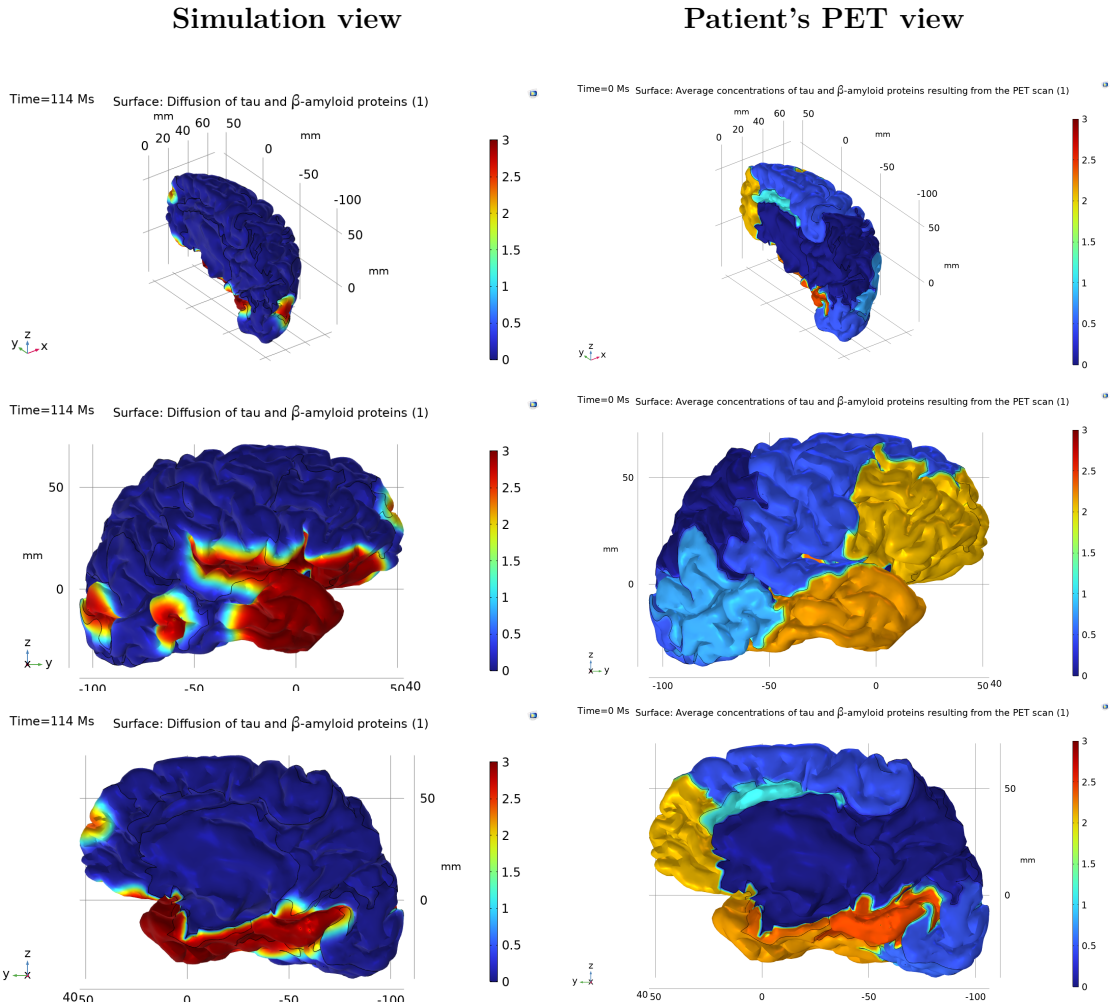

Figure 7.22: Comparison between the simulation with the parameters $\alpha_{tau} = 1.7\left[\frac{1}{year}\right]$, $\alpha_{\beta} = 1.1\left[\frac{1}{year}\right]$, $\gamma_{int} = 1.5\left[\frac{1}{year}\right]$ and the real data for patient 2. Left: view of the cerebral cortex invasion trend at time 114 months. Right: view of the cerebral cortex with the values of the concentrations calculated by PET in the respective areas.

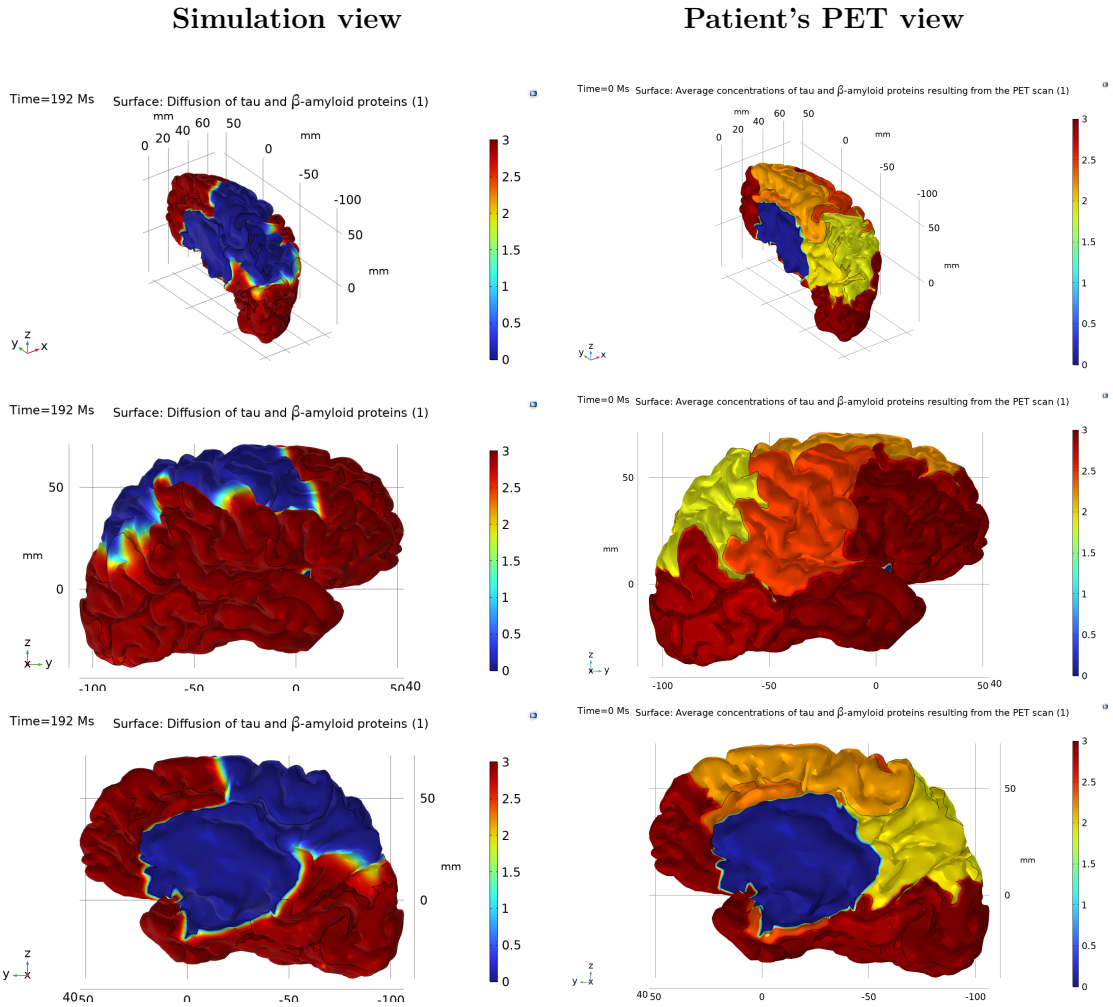

Figure 7.23: Comparison between the simulation with the parameters $\alpha_{tau} = 1.7 \left[\frac{1}{year}\right]$, $\alpha_{\beta} = 1.1 \left[\frac{1}{year}\right]$, $\gamma_{int} = 1.5 \left[\frac{1}{year}\right]$ and the real data for patient 3. Left: view of the cerebral cortex invasion trend at time 192 months. Right: view of the cerebral cortex with the values of the concentrations calculated by PET in the respective areas.

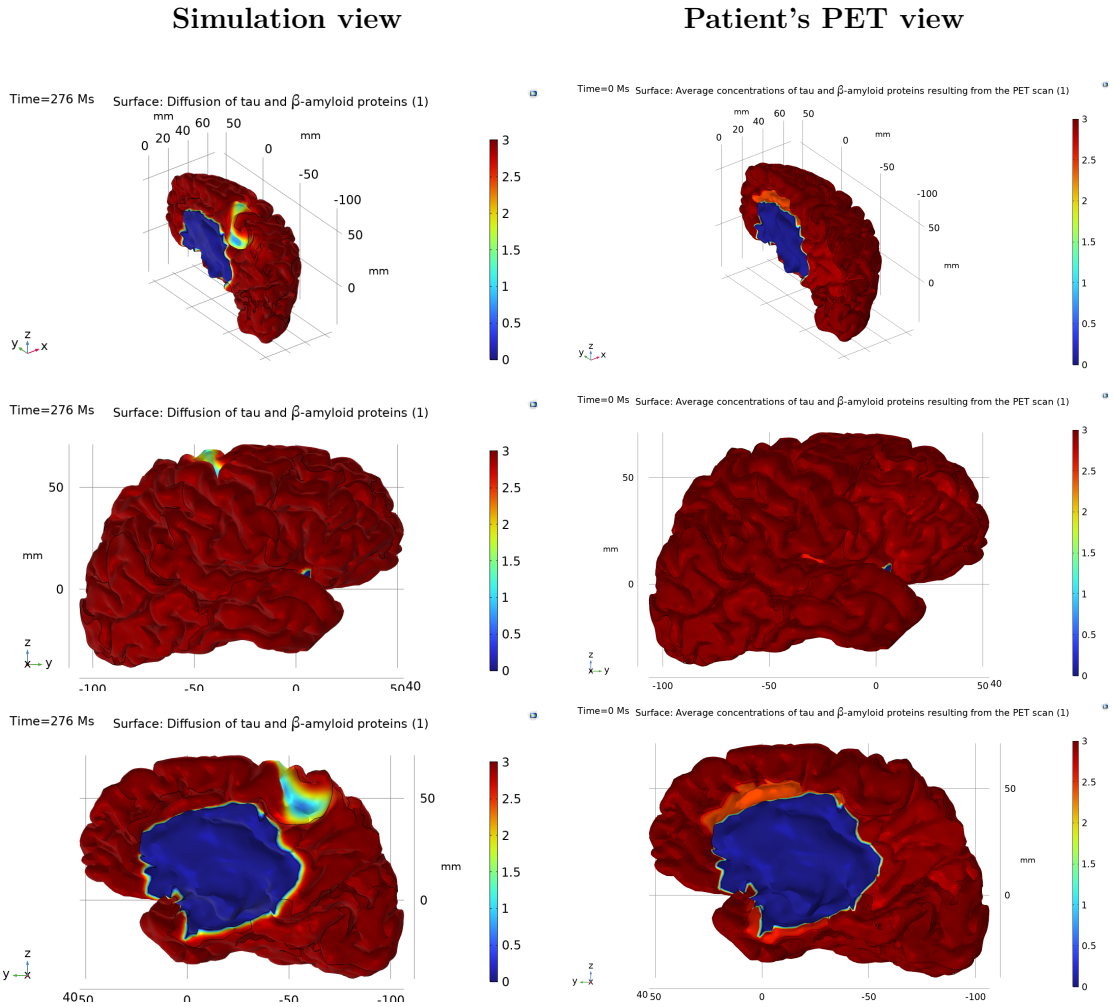

Figure 7.24: Comparison between the simulation with the parameters $\alpha_{tau} = 1.7 \left[\frac{1}{year}\right]$, $\alpha_{\beta} = 1.1 \left[\frac{1}{year}\right]$, $\gamma_{int} = 1.5 \left[\frac{1}{year}\right]$ and the real data for patient 4. Left: view of the cerebral cortex invasion trend at time 276 months. Right: view of the cerebral cortex with the values of the concentrations calculated by PET in the respective areas.

7.4.3 Case $\alpha_{tau} < \alpha_{\beta}$

The last case analysed corresponds to the condition $\alpha_{tau} < \alpha_{\beta}$, with parameter values set to $\alpha_{tau} = 1.1 \left[\frac{1}{year}\right]$ and $\alpha_{\beta} = 1.7 \left[\frac{1}{year}\right]$. Following the same procedure adopted in the previous sections, the subsequent discussion addresses the results obtained for each of the four patients.

For patient 1 (RID = 31), the estimated mean time for cerebral cortex invasion is approximately 6.88 years. As shown in the first histogram of figure 7.25, only the entorhinal region presents a concentration different from zero, indicating that the disease is still in an initial phase. In the corresponding concentration graph in figure 7.26, the PET-derived values fall entirely within the first 10 years of the simulation. In figure 7.27, which compares the simulation at the calculated average time with the PET-derived spatial map, all brain areas appear in shades of blue, reporting negligible protein accumulation, except for the entorhinal region, where the spread has just begun.

For patient 2 (RID = 800), the mean invasion time is approximately 12.03 years. The second histogram in figure 7.25 shows non-zero concentrations in almost all brain regions, with higher values in the entorhinal, temporal, hippocampal, frontal, and mid-frontal areas. This pattern is also confirmed in figure 7.28, where the comparison between the simulation and the PET data reveals that regions with more intense red coloring are those with higher protein accumulation, while lighter shades and transitions toward blue indicate lower concentrations.

In the case of the patient 3 (RID = 1190), the average estimated invasion time is about 20.42 years. The third histogram in figure 7.25 illustrates that most regions of the brain are invaded by tau and β-amyloid proteins, with lower concentrations persisting only in the frontal, upper frontal, cingulate, and the wedge regions. As shown in figure 7.29, these areas are the last to be reached by the spread of the disease. In addition, the third graph of the concentration in figure 7.26 shows that the PET values, represented as points, are in the second half of the sigmoid curves, close to saturation.

Lastly, patient 4 (RID = 467) shows a calculated average invasion time of about 25.73 years, indicating an advanced stage of the disease. This is reflected in the fourth histogram of figure 7.25 and in the fourth concentration graph in figure 7.26, where the PET-derived dots appear in the final portion of the sigmoids. The advanced progression is further confirmed by figure 7.30, which shows a fully invaded cortex in both the simulation (left) and the PET-based reconstruction (right).

Tables 7.14, 7.15, 7.16, and 7.17 report the PET values, the corresponding simulation outputs, and the reference times for each patient. The histograms comparing simulated and PET-derived concentrations are presented in figure 7.25, while the corresponding average concentration trends by brain region are shown in figure 7.26.

Finally, the simulation outputs at the average time points — 78 months for patient 1, 144 months for patient 2, 246 months for patient 3, and 312 months for patient 4 — are compared with the respective PET data in figures 7.27, 7.28, 7.29, and 7.30.

Zones	Patient 1 values	Simulation values	Reference times (years)
Entorhinal zone	0.61	0.54	3
Temporal zone	0.07	0.062	4
Hippocampal zone	0.01	0.010	3.5
Sensorial zone	0.005	0.005	8.5
Occipital zone	0.003	0.0027	7.5
Language zone	0.0007	0.00059	8
Frontal zone	0.003	0.00034	6
Zone of the wedge	0.0002	0.00015	9
Mid-frontal zone	0.02	0.021	4
Parietal zone	0.0001	0.0001	11.5
Central zone	0.04	0.049	4
Upper-frontal zone	0.003	0.001	10
Cingulate zone	0.001	0.002	10.5

Table 7.14: Average concentrations of tau and β-amyloid proteins measured via the patient's PET scan, alongside the corresponding concentrations obtained from the simulation conducted with parameters $\alpha_{tau} = 1.1 \left[\frac{1}{\text{year}}\right]$, $\alpha_{\beta} = 1.7 \left[\frac{1}{\text{year}}\right]$, and $\gamma_{int} = 1.5 \left[\frac{1}{\text{year}}\right]$, as well as the respective reference times at which these simulated concentrations were recorded.

Zones	Patient 2 values	Simulation values	Reference times (years)
Entorhinal zone	2.35	2.359	8.5
Temporal zone	2.21	2.174	13.5
Hippocampal zone	2.44	2.439	14
Sensorial zone	0.52	0.463	13
Occipital zone	0.77	0.771	13.5
Language zone	0.45	0.508	14
Frontal zone	2.12	2.149	10.5
Zone of the wedge	0.007	0.0066	11.5
Mid-frontal zone	2.12	2.122	13
Parietal zone	0.0001	0.0001	11.5
Central zone	0.45	0.428	8.5
Upper-frontal zone	0.43	0.429	12
Cingulate zone	1.12	1.069	13

Table 7.15: Average concentrations of tau and β-amyloid proteins measured via the patient's PET scan, alongside the corresponding concentrations obtained from the simulation conducted with parameters $\alpha_{tau} = 1.1 \left[\frac{1}{\text{year}}\right]$, $\alpha_{\beta} = 1.7 \left[\frac{1}{\text{year}}\right]$, and $\gamma_{int} = 1.5 \left[\frac{1}{\text{year}}\right]$, as well as the respective reference times at which these simulated concentrations were recorded.

Zones	Patient 3 values	Simulation values	Reference times (years)
Entorhinal zone	2.44	2.441	13.5
Temporal zone	3	2.990	19.5
Hippocampal zone	2.95	2.951	28.5
Sensorial zone	2.98	2.981	22
Occipital zone	2.91	2.895	21.5
Language zone	3	2.991	22.5
Frontal zone	2.97	2.960	19
Zone of the wedge	1.99	1.992	22
Mid-frontal zone	3	2.968	18
Parietal zone	1.89	1.91	23.5
Central zone	2.48	2.515	21.5
Upper-frontal zone	2.21	2.24	19
Cingulate zone	2.31	2.281	15

Table 7.16: Average concentrations of tau and β-amyloid proteins measured via the patient's PET scan, alongside the corresponding concentrations obtained from the simulation conducted with parameters $\alpha_{tau} = 1.1 \left[\frac{1}{\text{year}}\right]$, $\alpha_{\beta} = 1.7 \left[\frac{1}{\text{year}}\right]$, and $\gamma_{int} = 1.5 \left[\frac{1}{\text{year}}\right]$, as well as the respective reference times at which these simulated concentrations were recorded.

Zones	Patient 4 values	Simulation values	Reference times (years)
Entorhinal zone	2.61	2.613	25
Temporal zone	3	2.999	25
Hippocampal zone	3	2.965	31.5
Sensorial zone	3	2.999	28
Occipital zone	3	2.999	29
Language zone	3	2.999	25
Frontal zone	3	2.960	25.5
Zone of the wedge	2.9	2.89	26
Mid-frontal zone	2.92	2.915	16.5
Parietal zone	3	2.999	31.5
Central zone	3	2.999	28
Upper-frontal zone	3	2.999	27.5
Cingulate zone	2.44	2.419	16

Table 7.17: Average concentrations of tau and β-amyloid proteins measured via the patient's PET scan, alongside the corresponding concentrations obtained from the simulation conducted with parameters $\alpha_{tau} = 1.1 \left[\frac{1}{\text{year}}\right]$, $\alpha_{\beta} = 1.7 \left[\frac{1}{\text{year}}\right]$, and $\gamma_{int} = 1.5 \left[\frac{1}{\text{year}}\right]$, as well as the respective reference times at which these simulated concentrations were recorded.

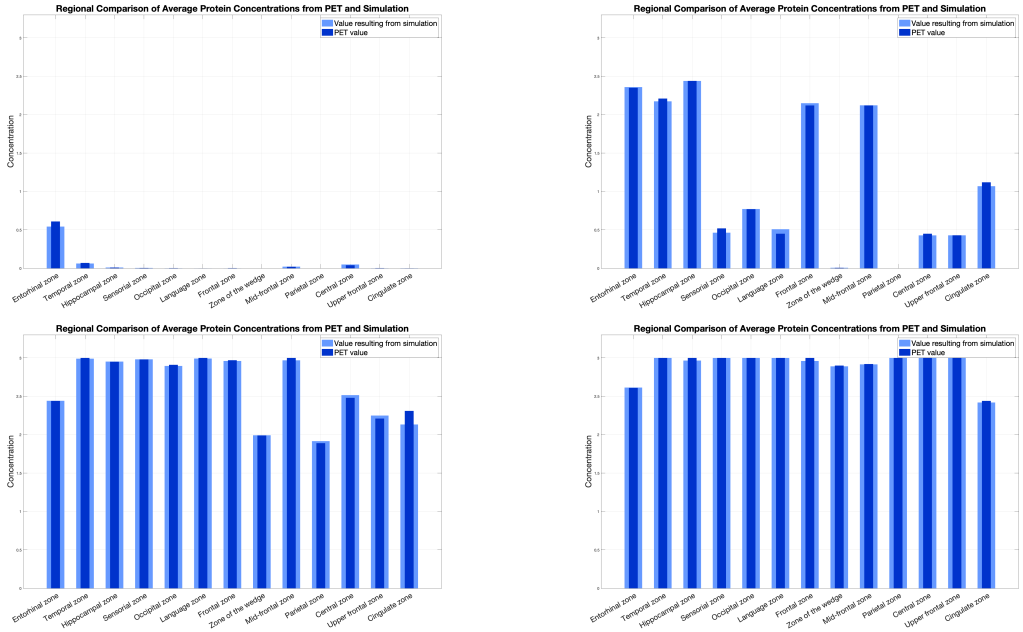

Figure 7.25: Comparison between the average concentrations obtained from the patient's PET scan (darker bars) and those computed by the simulation with parameters $\alpha_{tau} = 1.1\left[\frac{1}{year}\right]$, $\alpha_{\beta} = 1.7\left[\frac{1}{year}\right]$ and $\gamma_{int} = 1.5\left[\frac{1}{year}\right]$ (lighter bars) for patient 1, 2, 3 and 4, respectively.

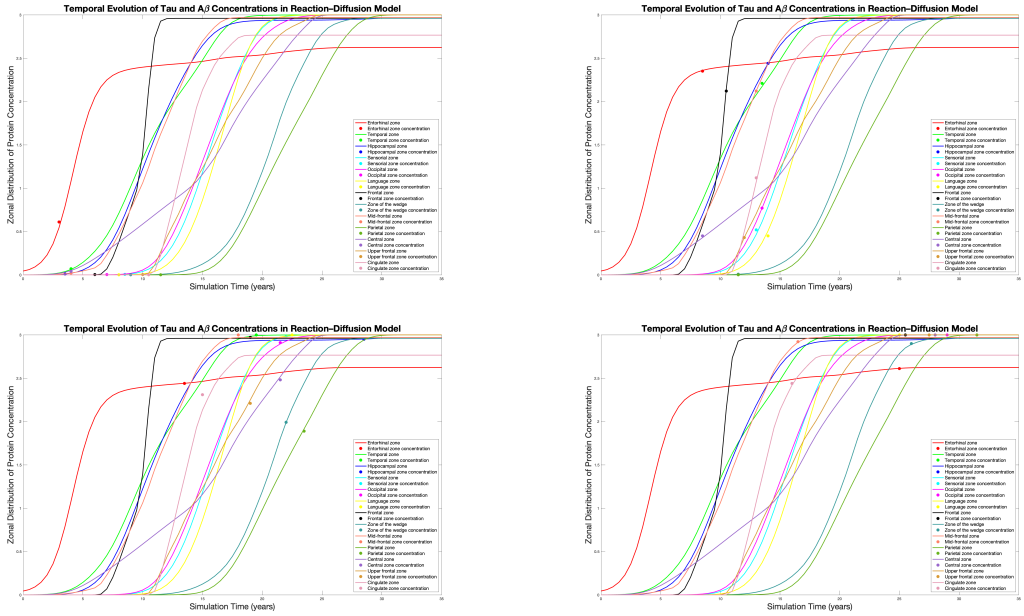

Figure 7.26: Trend of mean concentrations of tau and β-amyloid proteins in the simulation with parameters $\alpha_{tau} = 1.1\left[\frac{1}{year}\right]$, $\alpha_{\beta} = 1.7\left[\frac{1}{year}\right]$ and $\gamma_{int} = 1.5\left[\frac{1}{year}\right]$. The dots represent the average concentrations per zone calculated by PET for patient 1, 2, 3 and 4, respectively.

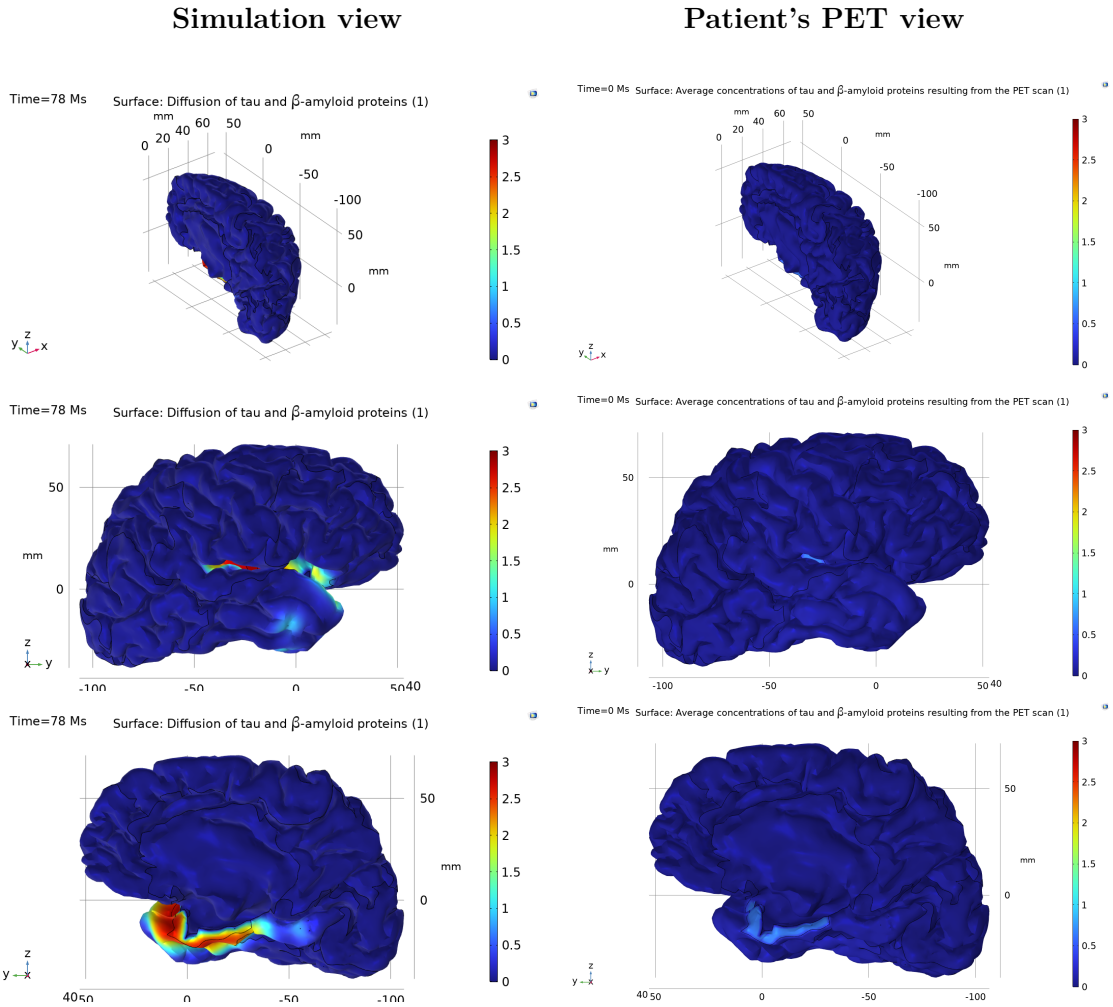

Figure 7.27: Comparison between the simulation with the parameters $\alpha_{tau} = 1.1 \left[\frac{1}{year}\right]$, $\alpha_{\beta} = 1.7 \left[\frac{1}{year}\right]$, $\gamma_{int} = 1.5 \left[\frac{1}{year}\right]$ and the real data for patient 1. Left: view of the cerebral cortex invasion trend at time 78 months. Right: view of the cerebral cortex with the values of the concentrations calculated by PET in the respective areas.

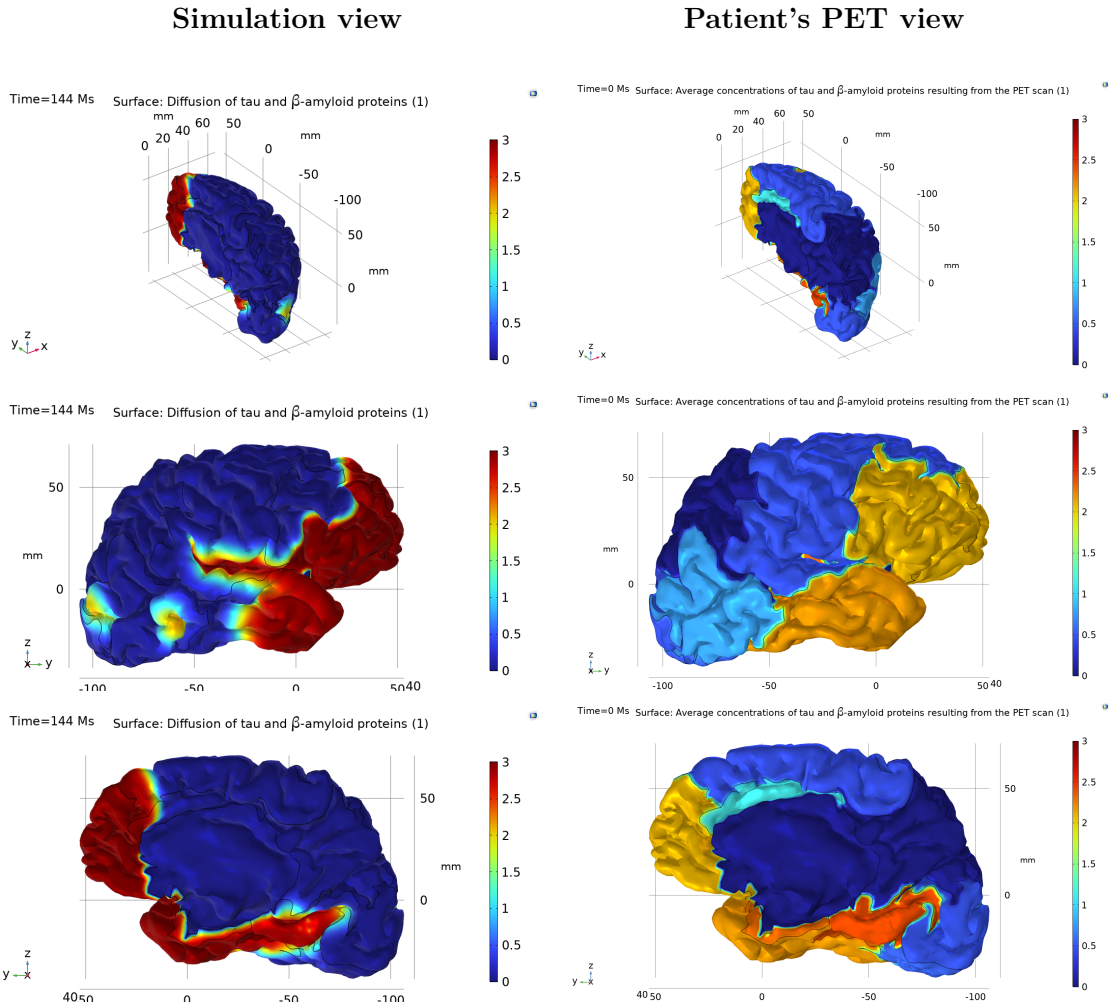

Figure 7.28: Comparison between the simulation with the parameters $\alpha_{tau} = 1.1\left[\frac{1}{year}\right]$, $\alpha_{\beta} = 1.7\left[\frac{1}{year}\right]$, $\gamma_{int} = 1.5\left[\frac{1}{year}\right]$ and the real data for patient 2. Left: view of the cerebral cortex invasion trend at time 144 months. Right: view of the cerebral cortex with the values of the concentrations calculated by PET in the respective areas.

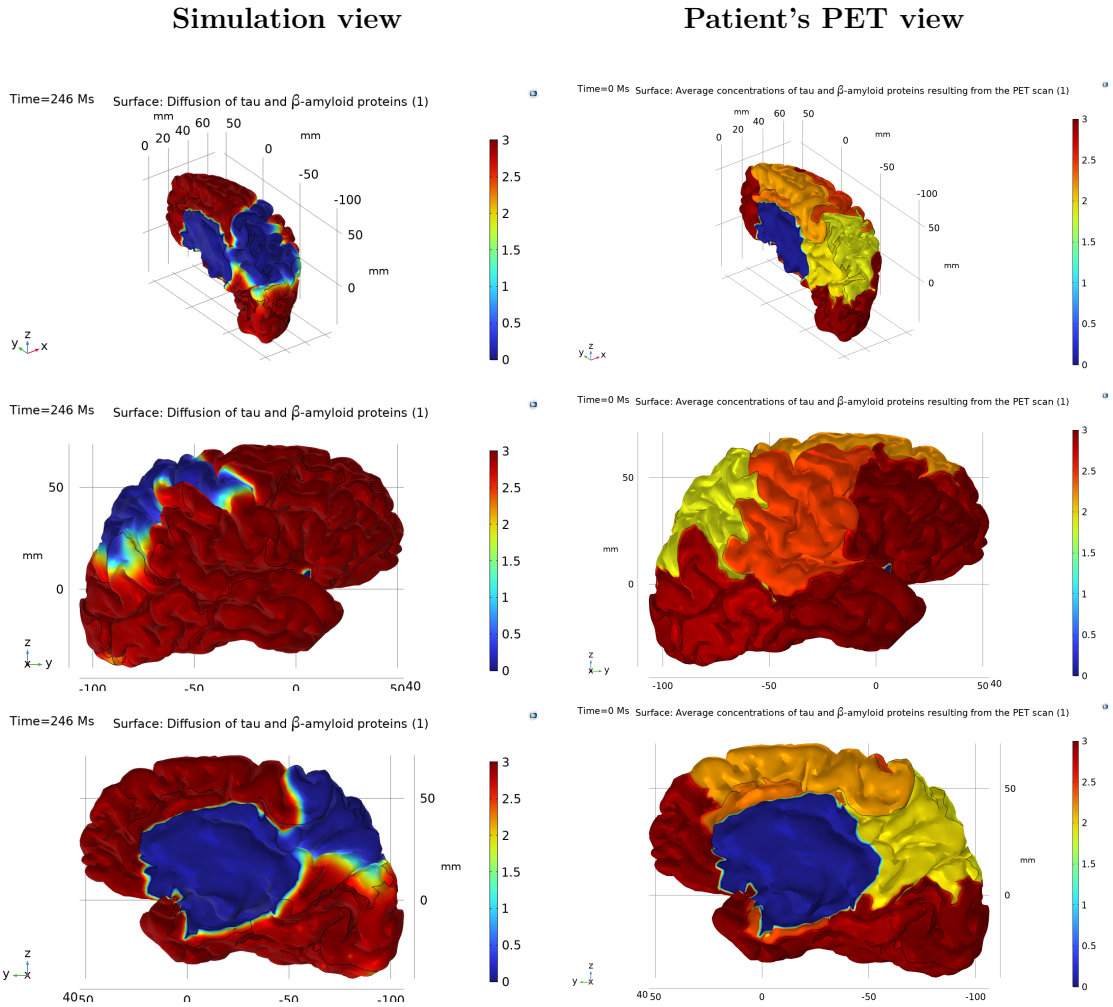

Figure 7.29: Comparison between the simulation with the parameters $\alpha_{tau} = 1.1\left[\frac{1}{year}\right]$, $\alpha_{\beta} = 1.7\left[\frac{1}{year}\right]$, $\gamma_{int} = 1.5\left[\frac{1}{year}\right]$ and the real data for patient 3. Left: view of the cerebral cortex invasion trend at time 246 months. Right: view of the cerebral cortex with the values of the concentrations calculated by PET in the respective areas.

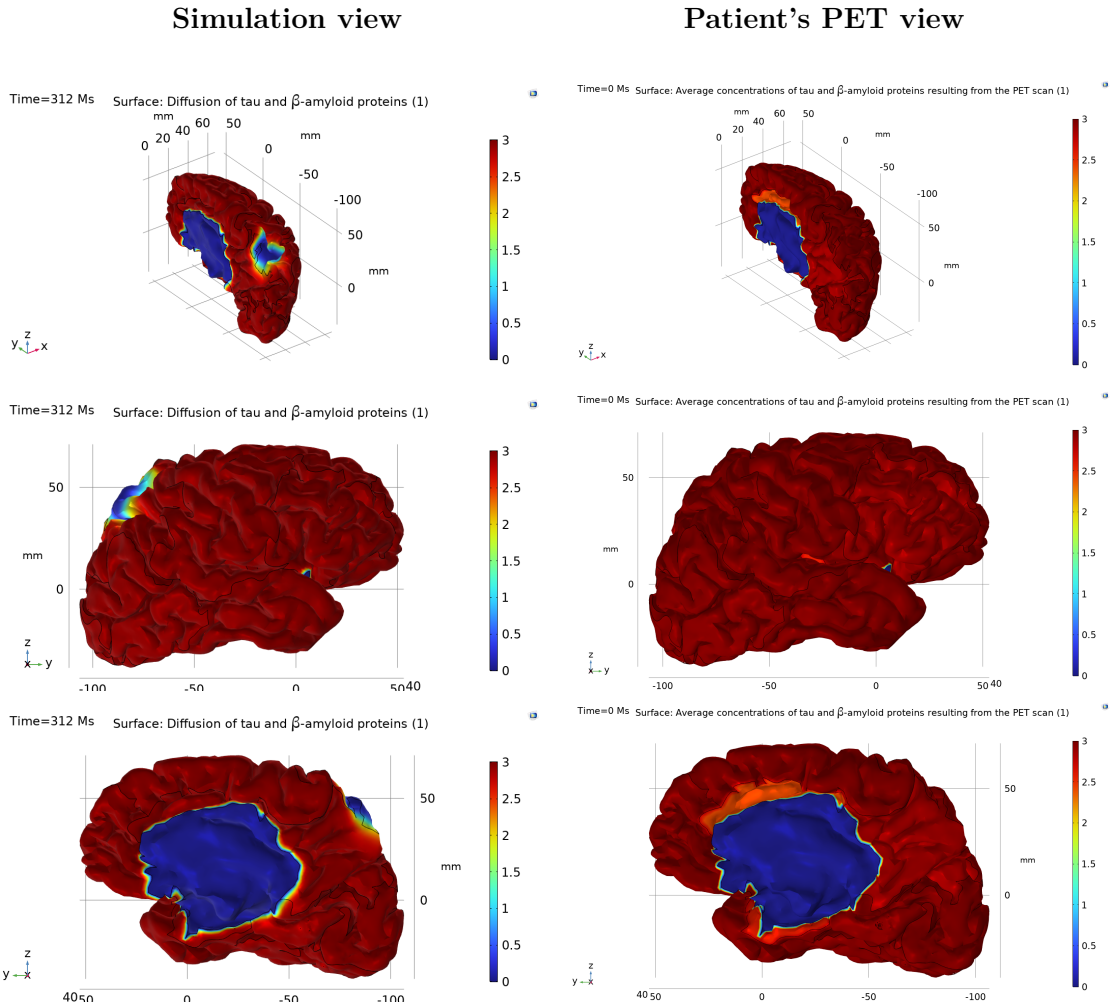

Figure 7.30: Comparison between the simulation with the parameters $\alpha_{tau} = 1.1\left[\frac{1}{year}\right]$, $\alpha_{\beta} = 1.7\left[\frac{1}{year}\right]$, $\gamma_{int} = 1.5\left[\frac{1}{year}\right]$ and the real data for patient 4. Left: view of the cerebral cortex invasion trend at time 312 months. Right: view of the cerebral cortex with the values of the concentrations calculated by PET in the respective areas.

7.4.4 Overall results

The average cerebral cortex invasion times calculated from the parametric study conducted with varying values of α_{tau} and α_{β} are reported in the corresponding table 7.18.

It is evident from the parametric study that, as the parameter α_{tau} increases, even in cases where α_{β} decreases, the time it takes for misfolded proteins to spread throughout brain regions progressively decreases. This trend is particularly clear in patients 3 and 4, suggesting that when the interaction between tau and β-amyloid proteins becomes more significant, the disease progression accelerates noticeably.

This relationship is also illustrated graphically in the figure 7.31, which shows the calculated invasion times across different parameter configurations. The parametric analysis thus reinforces the observation that increasing α_{tau} consistently shortens the average time required for complete cortical invasion. This supports the hypothesis that the tau protein plays a primary role in initiating and sustaining the propagation of neurodegenerative pathology. From a biological point of view, this result is in line with evidence in the literature suggesting that misfolded tau spreads trans-neuronally along the anatomical connectome pathways and acts as an early biomarker of Alzheimer's disease progression. The sensitivity of the model is thus further supported by the fact that α_{tau} is a strong time factor and cortical involvement.

Within this study, not only the role of the tau protein misfolding rate, α_{tau}, is considered relevant, but also that of the β-amyloid protein, represented by the parameter α_{β}. This becomes particularly evident when analysing the behaviour of simulations based on the modified patient model (7.1). Compared to those performed using the protein interaction model, it is observed that as the parameter α_{β} increases, the final invasion pattern shifts from the superior frontal region toward the zone of the wedge. However, according to the literature, the superior frontal cortex is typically among the last regions to be affected by protein accumulation. This discrepancy suggests that the parameter α_{β} must be constrained within a specific range to prevent this biologically inconsistent spatial shift.

This observation can be verified by comparing the simulation results for patient 4 with parameters $\alpha_{tau} = 1.1 \left[\frac{1}{year}\right]$, $\alpha_{\beta} = 1.7 \left[\frac{1}{year}\right]$, and $\gamma_{int} = 1.5 \left[\frac{1}{year}\right]$ (see figure 7.30) with any other simulation included in the parametric study presented in Chapter 6.

Overall, these results confirm the importance of carefully calibrating the parameters governing protein dynamics, in particular α_{tau} and α_{β}, in order to reproduce biologically realistic disease trajectories.

From a modelling point of view, this emphasises the need for physiologically grounded parameter ranges to ensure temporal and spatial consistency with clinical observations. From a clinical point of view, on the other hand, these results may help to improve the interpretation of PET imaging and simulation-based disease staging, offering a more refined tool to assess patient-specific progression and potentially guide therapeutic strategies.

ID	α_{tau} $\left[\frac{1}{year}\right]$	α_{β} $\left[\frac{1}{year}\right]$	γ_{int} $\left[\frac{1}{year}\right]$	Average Invasion Times
Patient 1	1.1	1.7	1.5	6.88
	1.5	1.5		5.69
	1.7	1.1		5.52
Patient 2	1.1	1.7	1.5	12.03
	1.5	1.5		10.15
	1.7	1.1		9.61
Patient 3	1.1	1.7	1.5	20.42
	1.5	1.5		16.76
	1.7	1.1		16.26
Patient 4	1.1	1.7	1.5	25.73
	1.5	1.5		25.19
	1.7	1.1		22.84

Table 7.18: Average cerebral cortex invasion times calculated for each patient under different parameter configurations. In all simulations, the interaction parameter was held constant at $\gamma_{int} = 1.5 \left[\frac{1}{\text{year}}\right]$, while the values of α_{tau} and α_{β} were varied as follows: $(\alpha_{tau}, \alpha_{\beta}) = (1.1, 1.7)$, $(1.5, 1.5)$, and $(1.7, 1.1)$ $\left[\frac{1}{\text{year}}\right]$, respectively.

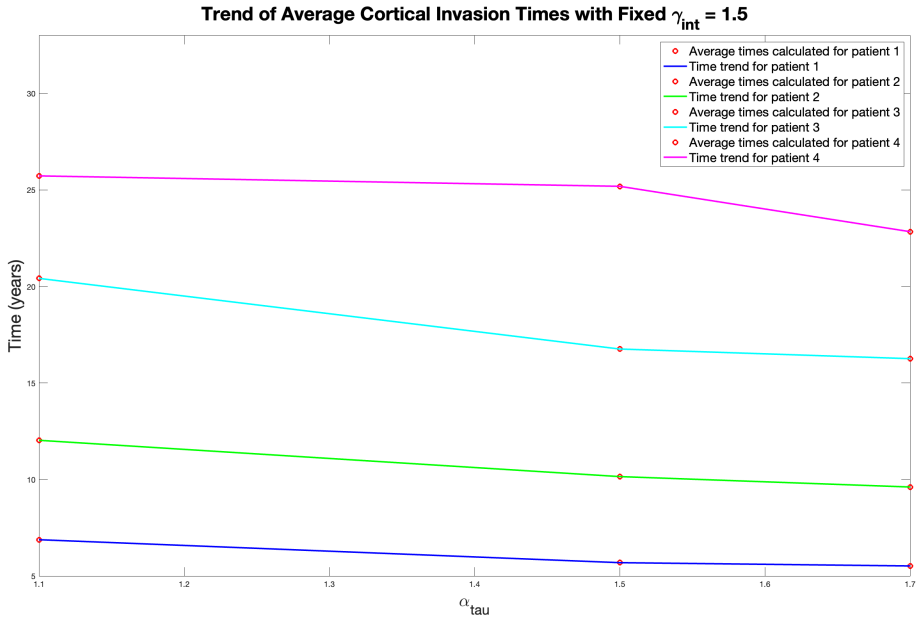

Figure 7.31: Trends of the average cortical invasion times obtained from simulations with varying α_{tau} and α_{β} values, and fixed $\gamma_{int} = 1.5 \left[\frac{1}{\text{year}}\right]$. From top to bottom, results are shown for patients 1, 2, 3, and 4, respectively.

Finally, the Euclidean norm error was computed for each patient across the four reported simulations. The purpose of this calculation was to quantify the deviation between the simulated concentrations of misfolded proteins in the cerebral cortex — obtained from the patient-specific model implementation — and the real concentrations measured via PET imaging.

The Euclidean norm error is defined by the following formula:

$$err = ||v - w||_2 \tag{7.2}$$

where v is the vector of PET-derived values for each patient, and w is the vector of simulated concentrations.

The calculated errors for each simulation are reported in table 7.19.

ID	$\alpha_{tau} = 1.1 \left[\frac{1}{\text{year}}\right]$ $\alpha_{\beta} = 1.7 \left[\frac{1}{\text{year}}\right]$ $\gamma_{int} = 1.5 \left[\frac{1}{\text{year}}\right]$	$\alpha_{tau} = 1.5 \left[\frac{1}{\text{year}}\right]$ $\alpha_{\beta} = 1.5 \left[\frac{1}{\text{year}}\right]$ $\gamma_{int} = 1.5 \left[\frac{1}{\text{year}}\right]$	$\alpha_{tau} = 1.7 \left[\frac{1}{\text{year}}\right]$ $\alpha_{\beta} = 1.1 \left[\frac{1}{\text{year}}\right]$ $\gamma_{int} = 1.5 \left[\frac{1}{\text{year}}\right]$	$\alpha_{tau} = 0.9 \left[\frac{1}{\text{year}}\right]$ $\alpha_{\beta} = 0.9 \left[\frac{1}{\text{year}}\right]$ $\gamma_{int} = 1.2 \left[\frac{1}{\text{year}}\right]$
Patient 1	0.0682	0.1157	0.0886	0.0076
Patient 2	0.1095	0.1336	0.1451	0.1859
Patient 3	0.1903	0.0604	0.1377	0.0789
Patient 4	0.0576	0.0949	0.0639	0.1182

Table 7.19: Euclidean norm errors between the PET-result concentrations and the simulated concentrations, calculated for each patient by varying the parameters α_{tau}, α_{β} and γ_{int}.

The analysis of the error values reveals that the accuracy of the simulations varies depending on the parameter set used. In general, lower Euclidean norm errors correspond to parameter configurations that better capture the disease stage inferred from PET scans, both in terms of spatial distribution and magnitude of accumulation.

In most cases, the lowest errors were obtained for simulations in which the average invasion time closely matched the apparent disease progression observed in PET data. This suggests that calibrating parameters such as α_{tau} and α_{β} is critical not only for temporal alignment but also for achieving spatial fidelity in concentration estimates.

For instance, patient 4 consistently showed lower errors across simulations, indicating good agreement between model predictions and PET results. Conversely, patient 2 exhibited relatively higher errors, likely due to the minimal spread of pathology at early stages, which makes numerical approximations more sensitive to noise or local variations in PET-signal.

These findings highlight the sensitivity of the model to parameter variations and underline the importance of personalized calibration for accurate prediction. In particular, the interaction between α_{tau} and α_{β}, dictated by the parameter γ_{int}, appears to play a key role not only in disease progression, but also in determining the fit of the model to real-world data.

8. Conclusions

This final chapter presents the concluding observations of the work carried out, highlighting both its current limitations and possible future developments aimed at improving the results obtained.

Starting from the analysis of the model used, the Fisher-Kolmogorov reaction-diffusion model (3.1), it can be stated that it effectively captures the diffusion dynamics underlying the propagation of neurodegenerative diseases in the brain. The invasion times derived from the simulations, both in the case of tau protein diffusion alone and in the study of its interaction with β-amyloid, appear to closely match the actual progression times observed in patients affected by Alzheimer's disease.

Regarding the connectome structure implemented in COMSOL Multiphysics, the simulations demonstrated that it provides a coherent continuous representation of the discrete connectivity model typically used in this field. This structure enabled the diffusion processes to be modelled in a realistic spatial framework aligned with known neuro-anatomical pathways.

Focusing on the applied study involving the diffusion of misfolded proteins in the cerebral cortices of the four selected patients, the average invasion times computed were found to reflect the clinical and pathological conditions of each case. The model shows promise in its ability to temporally place a patient within the disease progression curve. This becomes particularly evident when the symptomatology observed, and clinically attributed to a certain disease stage, is correctly identified by the model within a comparable timeframe. This correspondence supports the validity of the chosen parameters — including the diffusion coefficients of the two protein species, their respective propagation rates, and the interaction coefficient — all of which exhibit units of measurement and magnitudes consistent with physiological expectations and literature data.

An additional remark concerns the computational cost associated with the implementation of the three models and the simulation times observed. For the model simulating the spread of the tau protein alone (6.1), the average simulation time was approximately 35–45 seconds. In the model including the interaction with β-amyloid (6.2), this increased to 90–100 seconds. Finally, in the most complex patient-specific model (7.1), each simulation required approximately 3–5 minutes.

This progressive increase in computational demand reflects the added complexity of the system and the number of parameters involved.

The following sections discuss in detail the limitations encountered in the models and simulations developed, and propose potential directions for future research aimed at extending and improving the work presented here.

8.1 Limitations

This section outlines the main limitations currently affecting the models analyzed in this study.

First and foremost is the assumption regarding the propagation of misfolded proteins within the connectome structure. In the present work — as in several recent studies on the same topic — it was assumed that the spread of tau and β-amyloid proteins does not affect the architecture of the connectome itself [26]. This simplification is based on the biological rationale that, under normal physiological conditions, the brain is capable of regulating the accumulation of pathological proteins through efficient clearance mechanisms. In neurodegenerative diseases, however, this balance is disrupted, resulting in the progressive formation of toxic aggregates that propagate across neural regions, causing widespread cellular dysfunction [11].

Despite this, there is increasing evidence that the propagation of these aggregated proteins may not be entirely passive. In the long term, their accumulation may induce structural and functional alterations in the neuronal pathways themselves. Therefore, future modelling efforts should consider the introduction of a dynamic coefficient or function capable of capturing changes in the physical characteristics of the connectome over time — for example, representing synaptic weakening, atrophy, or axonal degradation. To date, few comprehensive models attempt to describe both cortical diffusion and dynamic alterations in white matter connectivity during the course of neurodegeneration.

A second limitation concerns the spatial discretization of the idealized brain structure used for the simulations. The division of the cortex into 14 macroscopic regions allowed a tractable and interpretable analysis of the spatial-temporal invasion pattern [21]. However, this simplification inevitably grouped together functionally heterogeneous areas, possibly introducing inaccuracies — particularly in the patient-specific model, where the simulated concentrations were compared with PET-derived measurements.

To enable this comparison, regional averages were computed over the micro-areas composing each macro-region. This averaging process, although necessary, likely introduced a loss of resolution and spatial specificity. A possible solution would involve implementing a more detailed partitioning of the cortex, segmenting it into a greater number of anatomically or functionally defined micro-regions. Mapping the simulations directly onto this higher-resolution cortical geometry could improve the match between model predictions and PET-derived concentration data. In this way, both the generated concentration histograms and the spatial progression graphs would reflect more accurately the real spatial heterogeneity of the pathological burden.

It can reasonably be assumed that as the number of regions considered and the complexity of the dynamic processes modelled - including the interaction between protein accumulation and connectome structure - increases, the computational cost and simulation time will also increase. However, these developments are essential to capture the full biological complexity of disease progression in neurodegenerative disorders such as Alzheimer's.

Based on the limitations discussed above, the following section presents possible directions for future work aimed at overcoming these constraints and enhancing the biological realism and predictive capacity of the models.

8.2 Future work

There are several promising directions for the future development of this research, a few of which are outlined below.

One of the most immediate extensions would be to incorporate the left hemisphere of the brain into the model, mapping its anatomical subdivisions and functional areas, and examining how they are affected by disease progression in parallel with the right hemisphere.

Another important step could involve increasing the complexity of both the brain and the connectome structures. Building on the foundation laid in this work, the connectome could be further refined to more closely resemble real anatomical data, increasing the density and distribution of inter-regional connections. Although such an improvement is likely to increase the computational cost and simulation time, it would provide a complete brain model capable of capturing the simultaneous propagation of misfolded proteins in both hemispheres. In this context, one could revise the original mesh imported into COMSOL Multiphysics or generate a new, more detailed one to improve the spatial accuracy of simulations and parameter estimation.

A third avenue for future work involves expanding the patient cohort used to validate the model. This would not only provide further testing ground for the model's robustness but also help identify limitations and improve its generalizability. In particular, selecting patients at different stages of disease progression would offer insights into how symptoms and protein diffusion patterns evolve over time. Gradually, this approach could lead to the creation of a comprehensive database of case studies and a predictive tool capable of accurately placing new patients within the appropriate disease phase.

Further development could focus on the possibility of customising model parameters, in particular α_{tau}, α_{β} and γ_{int}, by calibrating them directly to each patient's PET scan data. This would make it possible to construct a grid of parameters from which to select the most suitable values according to individual disease profiles, minimising errors and improving the adaptability of the model to patient-specific conditions.

Furthermore, the current model could be extended to incorporate biologically realistic mechanisms such as protein clearance, impaired glial function, or region-specific vulnerability. These additions would allow the model to simulate the imbalance between production and removal of misfolded proteins — a key aspect of neurodegenerative pathology — with greater fidelity. Expanding the framework to integrate molecular-level features, such as gene expression or synaptic connectivity, could also support a multi-scale modelling approach, linking microscopic processes to macroscopic anatomical changes.

Lastly, the integration of clinical data beyond PET imaging, including MRI, cerebrospinal fluid biomarkers, or electrophysiological recordings, would enhance model calibration and validation. Combined with machine learning algorithms, the simulation results could be used to develop hybrid predictive models that forecast disease progression or classify patient status with higher accuracy. Over time, this could support the development of clinical decision-support tools tailored to personalized medicine, capable of predicting the outcome of pharmacological interventions and simulating their effect on cortical involvement and disease course.

Bibliography

[1] ADNI. Adni neuroimaging pet data, 2025. Accessed: 2025-06-28.

[2] Heiko Braak and Eva Braak. Neuropathological stageing of alzheimer-related changes. *Acta neuropathologica*, 82(4):239–259, 1991.

[3] Heiko Braak, Kelly Del Tredici, Udo Rüb, Rob AI De Vos, Ernst NH Jansen Steur, and Eva Braak. Staging of brain pathology related to sporadic parkinson's disease. *Neurobiology of aging*, 24(2):197–211, 2003.

[4] Johannes Brettschneider, Kelly Del Tredici, Jon B Toledo, John L Robinson, David J Irwin, Murray Grossman, EunRan Suh, Vivianna M Van Deerlin, Elisabeth M Wood, Young Baek, et al. Stages of ptdp-43 pathology in amyotrophic lateral sclerosis. *Annals of neurology*, 74(1):20–38, 2013.

[5] Felix Carbonell, Yasser Iturria-Medina, and Alan C Evans. Mathematical modeling of protein misfolding mechanisms in neurological diseases: a historical overview. *Frontiers in Neurology*, 9:37, 2018.

[6] Henry Vandyke Carter. Gray715.png. Wikimedia Commons, 1918. Public domain.

[7] Louis Collins, Alex Zijdenbos, Wim Baaré, and Alan Evans. Animal+insect: improved cortical structure segmentation. *Inf Process Med Imaging*, 1613:210–223, 06 1999.

[8] Vladimir Fonov, Alan C Evans, Kelly Botteron, C Robert Almli, Robert C McKinstry, D Louis Collins, Brain Development Cooperative Group, et al. Unbiased average age-appropriate atlases for pediatric studies. *NeuroImage*, 54(1):313–327, 2011.

[9] Vladimir S Fonov, Alan C Evans, Robert C McKinstry, CR Almli, and DL Collins. Unbiased nonlinear average age-appropriate brain templates from birth to adulthood. *NeuroImage*, 47:S102, 2009.

[10] Sveva Fornari, Amelie Schäfer, Mathias Jucker, Alain Goriely, and Ellen Kuhl. Prion-like spreading of alzheimer's disease within the brain's connectome. *Journal of the Royal Society Interface*, 16(159):20190356, 2019.

[11] Sara Garbarino and Marco Lorenzi. Investigating hypotheses of neurodegeneration by learning dynamical systems of protein propagation in the brain. *NeuroImage*, 235:117980, 2021.

[12] Mathias Jucker and Lary C. Walker. Self-propagation of pathogenic protein aggregates in neurodegenerative diseases. *Nature*, 501(7465):45–51, Sep 2013.

[13] Kigsz. Human_brain.png. Wikimedia Commons, June 2012. Public domain mark 1.0.

[14] Joanna Masel, Vincent A.A. Jansen, and Martin A. Nowak. Quantifying the kinetic parameters of prion replication. *Biophysical chemistry*, 77(2):139–152, 1999.

[15] Jennifer A. McNab, Brian L. Edlow, Thomas Witzel, Susie Y. Huang, Himanshu Bhat, Keith Heberlein, Thorsten Feiweier, Kecheng Liu, Boris Keil, Julien Cohen-Adad, M. Dylan Tisdall, Rebecca D. Folkerth, Hannah C. Kinney, and Lawrence L. Wald. The human connectome project and beyond: Initial applications of 300mt/m gradients. *NeuroImage*, 80:234–245, 2013. Mapping the Connectome.

[16] Aliasghar Mortazi, Jayaram K Udupa, Dewey Odhner, Yubing Tong, and Drew A Torigian. Post-acquisition standardization of positron emission tomography images. *Front. Nucl. Med.*, 3, September 2023.

[17] G. Pocock and C.D. Richards. *Human Physiology-The Basis of Medicine third edition.* Oxford University Press, Oxford, 2006.

[18] Ashish Raj, Justin Torok, and Kamalini Ranasinghe. Understanding the complex interplay between tau, amyloid and the network in the spatiotemporal progression of alzheimer's disease. *bioRxiv*, 2024.

[19] Balázs Szalkai, Csaba Kerepesi, Bálint Varga, and Vince Grolmusz. Parameterizable consensus connectomes from the human connectome project: the budapest reference connectome server v3.0. *Cognitive Neurodynamics*, 11(1):113–116, February 2017.

[20] Dietmar R. Thal, Udo Rüb, Mario Orantes, and Heiko Braak. Phases of a-deposition in the human brain and its relevance for the development of ad. *Neurology*, 58(12):1791–1800, 2002.

[21] Lucina Q. Uddin, B. T. Thomas Yeo, and R. Nathan Spreng. Towards a universal taxonomy of macro-scale functional human brain networks. *Brain Topography*, 32(6):926–942, Nov 2019.

[22] Jacob W Vogel, Nick Corriveau-Lecavalier, Nicolai Franzmeier, Joana B Pereira, Jesse A Brown, Anne Maass, Hugo Botha, William W Seeley, Dani S Bassett, David T Jones, et al. Connectome-based modelling of neurodegenerative diseases: towards precision medicine and mechanistic insight. *Nature Reviews Neuroscience*, 24(10):620–639, 2023.

[23] Lary C. Walker and Mathias Jucker. Neurodegenerative diseases: Expanding the prion concept. *Annual Review of Neuroscience*, 38:87–103, 2015.

[24] J Weickenmeier, CAM Butler, PG Young, Alain Goriely, and E Kuhl. The mechanics of decompressive craniectomy: Personalized simulations. *Computer Methods in Applied Mechanics and Engineering*, 314:180–195, 2017.

[25] Johannes Weickenmeier, Mathias Jucker, Alain Goriely, and Ellen Kuhl. A physics-based model explains the prion-like features of neurodegeneration in alzheimer's disease, parkinson's disease, and amyotrophic lateral sclerosis. *Journal of the Mechanics and Physics of Solids*, 124:264–281, 2019.

[26] Johannes Weickenmeier, Ellen Kuhl, and Alain Goriely. Multiphysics of prionlike diseases: Progression and atrophy. *Phys. Rev. Lett.*, 121:158101, Oct 2018.

[27] Qing Zhao, Xinxin Du, Wenhong Chen, Ting Zhang, and Zhuo Xu. Advances in diagnosing mild cognitive impairment and alzheimer's disease using 11c-pib-pet/ct and common neuropsychological tests. *Frontiers in Neuroscience*, Volume 17 - 2023, 2023.